University of Warsaw - Faculty of Physics

University of Bremen - Department 1 of Physics and Electrical Engineering

Tomasz Jakubczyk

Effects of photonic confinement on the emission from CdTe quantum dots

PhD thesis supervised by

professor Piotr Kossacki and professor Detlef Hommel

30.IV.2014

At the begining of my study I was priviledged to be supervised by late Professor Jan Gaj. I am convinced that he would read the work with great attention and bring valuable support. I hope that my thesis reflects at least partially scientific values which I learned during my work under his supervision. I dedicate this work to Professor Gaj.

Acknowledgments

It's my pleasure to thank people who either contributed to this work or made its realization a memorable and, most of all, positive experience.

First of all I would like to thank both of my supervisors for guidance during my studies. Also, I thank Piotr Kossacki for showing me day by day that physics is fun, and that understanding it is the greatest fun. I enjoyed that "doing research" was primarily about satisfying one's curiosity where the bonus is in realization of a formal scientific project, and not the other way round. I thank Detlef Hommel for a great hospitality. Without your constantly repeated assurance that I am welcomed in Bremen, which was beyond standard politeness and requirements of the realized projects, I wouldn't myself dare coming to Bremen more often than the contracted periods. This set for me great possibilities for exchange and mobility, far more comfortable than frames of the realized projects and, what is more important, far more efficient. But most of all I am thankful for your warmth welcoming in Bremen at private level and creation of a good team spirit in the work group.

This work wouldn't be possible without Wojciech Pacuski and his great samples. I thank you for growing the one microcavity sample which is the basis of my thesis, for discussions and many helpful ideas. Special thanks to Andrzej Golnik for his help, patience and serenity. I enjoyed work and discussions with Mateusz Goryca, Tomasz Smoleński, Johannes Binder and Jaś Suffczyński. I especially appreciate help of Tomasz Kazimierczuk and his guidance in the lab during my early years in the group in Warsaw. I highly value your attitude to share knowledge, impressive lab skills and valuable discussions about my work. I think you went to far in in politeness and modesty giving me brilliant ideas and trying to convince me that they were mine!

At this point I thank the whole AG Hommel team for friendly and professional approach to guests, which made my stays in Bremen both an enjoyable and fruitful time. I always had a feeling, even being already officially a Ph. D. candidate in

Bremen, to have as little responsibilities as a guest having all the privileges of a member of the group! In this regard my special thanks go to people who helped me the most in the work: Carsten Kruse, Thorsten Klein, Sebastian Klembt, Stephan Figge, Heiko Dartsch, Malte Fandrich, Timo Aschenbrenner, Torben Rohbeck - I learned a lot from you, I appreciate your disinterested help and good time I had working with you. I thank Matthias Florian, from the "'Theoretikern"' in Bremen for helpful discussions and valuable numerical simulations.

A large part of this work wouldn't be possible without my collaborators from the University of Leipzig. My special thanks go to Helena Franke. I appreciate our common work without the frames of projects, agreements, kick-start meetings, milestones... *etc.* Such project was therefore a delicate matter but your attitude made it a reliable cooperation. In this regard I am also thankful to Dr Rüdiger Schmidt-Grund and Prof. Marius Grundmann for their support.

For our collaboration, often related to the presented work I thank students Krzysztof Sawicki, Michał Papaj, Maciej Ściesiek, Paweł Duch and Gosia Pilat who were involved in the presented work at various stages. I am also very thankful to Olga Babicka for assistance during all the administrative tasks and organization of numerous travels.

It's my pleasure to thank Prof. Frank Jahnke and Prof. Andrzej Wysmołek for agreement to be the referees of my thesis.

I thank my parents for running a wonderful *Hotel Mama* during periods where I was an active researcher and during preparation of the manuscript. And finally my girlfriend Liv, thank you for the great care I got during preparations of manuscript and for tolerating me spending evenings and nights with the lab equipment.

Abstract

The thesis describes phenomena related to the control of the spontaneous emission from excitons in CdTe/ZnTe quantum dots (QDs). It describes development of ZnTe-based planar and micropillar cavities followed by the demonstration of modification of various aspects of QDs spontaneous emission.

In the first step basic optical properties of the microcavities were investigated. The experiments were conducted on structures with a large spectral density of quantum dot emission lines in the range of energies close to the energies of photonic modes. Thus, QDs acted as probes for the photonic characteristics of the structures. We determined energy of microcavity modes together with their Q-factors. We performed mode mapping of micropillar cavities and measured angular distribution of the emission originating from planar microcavity.

In further experiments micropillars with single QDs emission lines in the vicinity of the fundamental modes were investigated. The method of tuning the energy difference between an excitonic state and a cavity mode by a variation of the temperature of the sample was used. In the step we measured the intensity of emission related to quantum dot and cavity mode. This experiment shoed, that the emission from the mode is funneled from the emission of spectraly closest QD transition. In the next experiment we investigated time-resolved photoluminescence of the system. We measured the decay time of QDs placed inside micropillars for varied cavity mode - QD detuning. Additionally, we measeured decay time for QDs embedded in standard semiconductor matrix. This demonstrated enhancement of the decay rate of spontaneous emission from the micropillars if the emission is resonant. an Purcell-factor above 5 was demonstrated, in agreement with the model simulations

Next topic covered by the thesis is related to the development of the micropillars with an enhanced radial confinement. This project was realized in collaboration with the University of Leipzig, where an additional radial Bragg reflector was deposited on the micropillars. In the obtained structures we observed decrease of spontaneous

emission rate of QDs detunde from the cavity mode by factor more than 3. This demonstrates, that the coupling of QD emission into the undesired continuum of radial decay channels has been successfully decreased.

Finally, the last part of the thesis describes the development of epitaxial growth of ZnTe-based nanostructures on GaSb substrates. A series of samples with both quantum wells and distributed Bragg reflectors were grown by the molecular beam epitaxy. The photoluminescence and reflectivity of samples was characterized. The crystal quality and lattice constant was measured using High Resolution X-ray diffraction.

0.1 Streszczenie

Praca poświęcona jest poprawie sterowania spontaniczną emisją fotonów z kropek kwantowych wytworzonych z materiałów typu II-VI: z tellurku kadmu (CdTe) osadzonych w tellurku cynku (ZnTe). W tym celu zastosowano mikrownęki optyczne wykorzystujące opracowane niedawno rozproszone zwierciadła Braggowskie o stałej sieci ZnTe. Badania mikrownęk optycznych dla materiałów typu II-VI uzasadniony są istnieniem dojrzałej technologii półprzewodników półmagnetycznych tego typu, świetnymi własnościami optycznymi heterostruktur zawierających (Cd,Mn)Te (takich jak np. kropki kwantowe), oraz dobrą znajomością oddziaływań i stałych materiałowych. Te własności w połączeniu z wlasnosciami mikrownek optycznych pozwalają uzyskać systemy o unikatowych własnościach magneto-optycznych.

Bazując na planarnych mikrownękach wytworzono mikrownęki filarowe charakteryzujące się związaniem fotonicznym we wszystkich kierunkach przestrzeni. Własności optyczne mikrownęk filarowych zawierających kropki kwantowe zostały zbadane przy użyciu fotoluminescencji niskotemperaturowej. W pierwszym kroku wyznaczono energie fotonowych modów własnych mikrownęk filarowych oraz dobroć tych rezonatorów. Wykazano również modyfikacje widma emisji omawianych kropek kwantowych. Następnie zbadano szczegółowe własności modów własnych takich mikrownęk. Dokonano mapowania rozkładu przestrzennego emisji mikrownęk filarowych oraz zmierzono rozkład kątowy emisji mikrownęk planarnych w zależności od energii fotonu. Zbadano również aspekty polaryzacyjne emisji obu rodzajów mikrownęk. Stwierdzono, iż mod podstawowy składa się z dwóch niezdegenerowanych energetycznie modów własnych o wzajemnie prostopadłych polaryzacjach.

Wyniki pomiarów energii modów własnych dla różnych średnic mikrownęk filarowych porównano z symulacjami wykonanymi przy użyciu rozszerzonej metody

macierzy transferu. Uzyskano dobrą zgodność wyników symulacji z wynikami eksperymentalnymi. Czynnik Purcella opisuje przyśpieszenie spontanicznej emisji dla emitera we wnęce optycznej względem emitera w przestrzeni. Metodą macierzy transferu obliczono również efektywne objętości modów, co w połączeniu ze znajomością dobroci rezonatorów pozwoliło wyznaczyć spodziewaną zależność czynnika Purcella od średnicy mikrwonęki filarowej. Eksperymentalnie ustalono, iż największe przyśpieszenie emisji związane z efektem Purcella uzyskuje się dla mikrownęk o średnicy poniżej 2 mikrometrów. W eksperymentach z rozdzielczością czasową wykazano skrócenie czasu życia ekscytonu uwięzionego w kropce kwantowej będącego w rezonansie z modem fotonicznym mikrownęki filarowej o średnicy 1,5 mikrometra. Uzyskany współczynnik Purcella o wartości 5,7 jest zgodny z wartością wyznaczoną dzięki symulacjom i pomiarom dobroci rezonatora.

W następnej kolejności zbadane zostały mechanizmy relaksacji wzbudzenia ekscytonowego do fotonicznych modów własnych mikrownęki poprzez oddziaływanie z siecią krystaliczną materiału półprzewodnikowego, z którego zrobiona jest kropka kwantowa. Pomiary te są wykonywane dla zmieniającej się w sposób kontrolowany temperatury próbki. Daje to możliwość sprzęgania wybranych stanów ekscytonowych z modami fotonicznymi, gdyż energie obu tych zmieniają się w różnym tempie w zależności od temperatury. Zbadno intensywności emisji kropki kwantowej i modu własnego mikrownęki przy zmianie ich dostrojenia energetycznego. Pozwoliło to wykazać, iż emisja modu zasilana jest z najbliższej spektralnie linii kropki kwantowej. Eksperyment ten wykazał również ukierunkowanie emisji kropki kwantowej poprzez sprzężenie jej z modem własnym mikrownęki, który to mod jest emitowany kierunkowo.

Dysponując dobrze poznanym systemem mikrownęk filarowych z kropkami kwantowymi CdTe/ZnTe opracowano nowatorskie mikrownęki filaorwe z dodatkowymi radialnymi rozproszonymi zwierciadłami Bragga. Dla takich mikrownęk wykazano, iż tempo rekombinacji promienistej w przypadku emiterów odstrojonych od modów własnych mikrownęki może zostać wydłużone o czynik co najmniej 3.

W zakresie badań technologicznych przeprowadzono również optymalizację wzrostu kropek kwantowych CdTe/ZnTe oraz zwierciadeł Bragga o stałej sieci ZnTe w komorze do epitaksji z wiązki molekularnej poprzez użycie nowego rodzaju podłoży z antymonku galu (GaSb). Dzięki lepszemu dopasowaniu stałej sieci krystalicznej w takim podłożu zmniejszła się gęstość defektów w wyhodowanych na nich strukturach.

Dzięki wytworzeniu wydajnych mikrownęk fotonicznych opartych na ZnTe ba-

dania kropek kwantowych CdTe w ZnTe zyskują nowe narzędzie do badania fizyki procesów w nich zachodzących. Własności materiałów II-VI, takie jak wysoka stabilność temperaturowa emisji i świecenie w widzialnym zakresie widma fal elektromagnetycznych, stawiają je jako dobre źródła pojedynczych fotonów na żądanie. Te ostatnie są kluczowym elementem informatyki i kryptografii kwantowej.

0.2 Zusammenfasung

Die vorliegende Arbeit beschäftigt sich mit der Verbesserung der Kontrolle der spontanen Emission von Photonen aus Quantenpunkten, die aus Materialien des Typs II-IV hergestellt wurden. Diese Materialien sind Cadmium-Tellurid (CdTe), das in Zink-Tellurid eingesetzt (ZnTe) wurde. Zu diesem Zweck wurden optische Mikrokavitäten verwendet, die auf kürzlich neu-entwickelte Bragg-Spiegeln mit die Gitterkonstante von ZnTe basieren. Die Entwicklung der Technologie der optischen Mikrokavitäten für Materialien des Typs II-IV wird begründet mit: der Existenz einer ausgereiften Technologie der aus diesen Materialien bestehende halbmagnetischen Halbleiter ; mit den ausgezeichneten optischen Eigenschaften ihrer Hetereostrukturen, die (Cd,Mn)Te (solche wie z.B. im Form von Quantenpunkte) enthalten ; sowie mit den soliden Kenntnissen über Wirkungen und Materialkonstanten. Diese Eigenschaften in Verbindung mit den Eigenschaften der optischen Mikrokavitäten ermöglichen es, Systeme mit einzigartigen magneto-optischen Eigenschaften zu generieren.

Die optischen Eigenschaften der Mikrosäulekavitäten, die Quantenpunkte enthalten, wurden mit Hilfe der Tieftemperatur-Mikrophotolumineszenz untersucht. In einem ersten Schritt wurden die Eigenenergien der Eigenmoden der Mikrosäulekavitäten und der Q-Faktoren bestimmt. Danach wurden die besonderen Eigenschaften der Eigenmoden dieser Mikrokavitäten untersucht. Es wurde ein Mapping der Verteilung der räumlichen Emission von Mikrokavitäten durchgeführt und es wurde der Winkel des Emissionsprofils von planaren Mikrokavitäten als Funktion der Photonenenergie gemessen. Gleichermaßen wurden Polarisationsaspekte der Emission von Kavitäten untersucht. Es wurde bestimmt, dass die erste Eigenmode aus zwei energie entatrtete Eigenmoden die gegenseitig senkrecht polariesiert sind.

Die Ergebnisse der Messungen der Energien der Eigenmoden für verschiedene Durchmesser der Mikrosäulenkavitäten wurden mit Simulationen verglichen, die mit Hilfe von Transfer-Matrix-Simulationen durchgeführt wurden. Es konnte hier eine klare Übereinstimmung der Ergebnisse der Simulationen mit den Ergebnissen aus

Experimenten festgestellt werden. Mit derselben Methode wurden zudem die effektiven Modalvolumina berechnet, was in Verbindung mit den vorhandenen Kenntnissen über die Q-Faktoren der Resonatoren dazu führte, die Abhängigkeit des Purcell-Faktors von dem Durchmesser der Mikrosäulenkavitäten bestimmen zu können. Der Purcell-Faktor beschreibt die Beschleunigung der spontanen Emission für Emitter in einer Kavität gegenüber Emittern im freien Raum. Es wurde bestimmt, dass die größte Beschleunigung der Emission, verbunden mit dem Purcell-Effekt, für Mikrokavitäten mit einem Durchmesser von weniger als 2 Mikrometer erreicht wird. In zeitaufgelösten Messungen wurde die Verkürzung der Lebensdauer des Exzitons nachgewiesen, das im Quantenpunkt fixiert ist und das sich in Resonanz mit der Eigenmode der Mikrosäulenkavität mit einem Durchmesser von 1,5 Mikron befindet. Der erzielte Purcell-Faktor mit einem Wert von 5,7 stimmt mit dem bestimmten dank der Simulationen Wert überein.

Anschließend wurden die Relaxationmechanismen des Exzitons zu den Eigenmoden der Mikrokavitäten durch Wechselwirkung Interaktion mit dem Halbleiter-Kristallgitter, aus dem der Quantenpunkt konstruiert ist, untersucht. Bei diesen Messungen wurde die Temperatur der Proben variiert. Dies bietet die Möglichkeit einer steubar Kopplung der ausgewählten Exzitonen mit ausgewählten Eigenmoden, weil sich die Energien dieser beiden Objekte in Abhängigkeit von der Temperatur nicht im gleichen Tempo verändern. Es wurde die Intensität der Emission der Quantenpunkte und der Eigenmoden der Mikrokavitäten bei Veränderung ihrer energetischen Verstimmung untersucht. Dies ermöglichte es, nachzuweisen, dass die Emission von Moden durch die nächstgelegene spektrale Quantenpunkte-Emissionslinie gespeist wird.

Da wir über ein gut entwickelt System von Mikrosäulenkavitäten mit auf CdTe/ZnTe -basierten Quantenpunkten verfügen, konnten wir neuartige Mikrosäulenkavitäten mit radialen Bragg-Spiegeln entwickeln. Für solche Mikrokavitäten wurde gezeigt, dass das Geschwindigkeit der radiativen Rekombination im Fall der Emitter, die von den Eigenmoden verstimmt sind, mindestens um den Faktor 3 verlangsamt werden kann. Dieses Ergebnis illustriert die Reduktion der photonischen Zustande die eine Ursache für die ungewünschte radiale Leckemission sind.

Die Arbeit beschreibt darüber hinaus die Optimierung der Molekularstrahlepitaxie zum Wachstum von Mikrokavitäten mit CdTe/ZnTe-Quantenpunkten durch die Verwendung einer neuen Art von Substraten aus Gallium Antimoniden (GaSb). Es ist zu erwarten, dass sich dank einer besseren Anpassung der Gitterkonstanten die Zahl der Defekte in gewachsenen Strukturen reduziert.

0. ABSTRACT

Dank der Herstellung von effektiven ZnTe-basierten Mikrokavitäten schaffen die Untersuchungen von CdTe-basierten Quantenpunkten neue Instrumentarien zur Untersuchung der Physik der in ihnen vorkommenden Prozesse. Die Eigenschaften der Materialien II-VI, wie zum Beispiel die hohe Temperaturstabilität der Emission im sichtbaren Spektralbereich, macht diese Strukturen zu guten Quantum-Lichtquellen.

Contents

Chapter 1

Introduction

If shortened to one sentence, the main goal of this work is to provide an efficient interface for encoding to photon the quantum state of a confined electron-hole pair in CdTe semiconductor quantum dots. This can be achieved by optimizing the temporal and spatial aspects of spontaneous recombination of such pair resulting in photon emission. The basic idea behind this is that the spontaneous emission (SE) does not only depend on the emitter itself but also on its environment. This fact was first formulated in a pioneering, now classical work of Purcell in 1946 [Purcell, 1946]. He proposed the possibility of controlling SE in the microwave range by coupling a spin system (nuclear magnetic moments) to a resonant electrical circuit, which later led to the birth of a whole new area of research called the cavity quantum electro-dynamics (cavity QED) [1], first explored in atomic physics experiments.

The interest in using photons lies in the fact that they can carry data more efficiently than is possible using pulses of electrons in wires. However, integrating photon sources and detectors into current electronics requires efficient coupling of light with electronic system. The limits of diffraction enable to focus light at most to a spot of the size equal to about half its wavelength, while current integrated circuits feature elements with the size of the order of $40 - 50\,\mathrm{nm}$. Therefore it is of vital importance to increase the duration of light-matter interaction to increase coupling efficiency. Optical cavities feature important advantages on this field.

[1] We can speak of cavity QED effect in the study of light-matter interaction if the quantum nature of light photons is significant.

1.1 History and presentation of the area of research

Achievements in research on the light matter coupling in optical cavities has been recently awarded with a Nobel Prize for Serge Haroche and David Weinland for controlling the properties of an atom by placing it in a microwave cavity made up of superconducting mirrors. However, experiments on single atoms require complicated preparations and atoms can interact with the cavity only transitory. Since Yablonovitch proposition of using a photonic crystal to inhibit the spontaneous emission of an emitter in a solid state system [Yablonovitch, 1987] much attention has been attracted to solid state photonic bandgap microcavities. Nowadays, advanced semiconductor epitaxial and nano-lithography techniques enabled realization of high quality, low volume optical cavities embedding semiconductor emitters, so similar experiments can be realized in solid state systems - better scalable and having potentially broader range of applications. Indeed, semiconductor cavities constitute nowadays the major playfield for cQED [1]. One of the possible ways of extending the area of research is to integrate new semiconducting materials and combine their unique features with the properties of photonic structures. It is the case of the work presented here, where investigations of a novel semiconductor-cavity system containing CdTe/ZnTe low dimensional emitters are described.

1.2 Introduction to the physics of emitter in cavity

1.2.1 Fermi's golden rule

We model the emitter by a two-level system with a transition frequency ω_0 and an isotropic dipole. The spontaneous emission appears as a jump of the electron from an initial level e to a final level f accompanied by the emission of a photon. This process can be understood as resulting from the coupling of the emitter's electron to the electromagnetic field in its "vacuum" state[2]. An essential feature of spontaneous emission in free space is that the emitter can radiate into any mode that satisfies the conservation of energy and momentum. The time of emission and the particular mode in which the photon is observed are random variables.

[1] Other material solid state resonators and artificial atoms which are since recently intensively explored include: molecules, nitrogen-vacancy centers in diamond coupled to photonic crystal cavities [Faraon *et al.*, 2011] or Fiber-Based microcavities and colloidal quantum dots (QDs) coupled to dielectric cavities or plasmonic antennas

[2] ground state or state of lowest energy for the field in the vicinity of the emitter

The probability Γ_0 of photon emission per unit time, often called the Einstein A-coefficient is governed by the Fermi's golden rule

$$\Gamma_0 = \frac{2\pi}{\hbar}|M_{ef}|^2\rho_0(\omega_0), \tag{1.1}$$

where $|M_{ef}|$ is the matrix element for the emitter between two levels and $\rho_0(\omega_0)$ is the mode density which is the number of modes available per unit frequency interval.

The probability $P_e(t)$ of finding an emitter still excited at time t after its preparation in state e is $exp(-\Gamma_0 t)$. Such an exponential decay law describes an irreversible process that leads the emitter to its ground state. At the origin of irreversibility is the continuum of field resonantly coupled to the emitter which acts as a gigantic reservoir, a thermodynamical equivalent of the *heat bath.* According to the thermodynamics laws the excitation of the emitter is absorbed by the field which contains many more possible states, and thus it decays away.

1.2.2 Purcell effect

In a cavity, the density of modes is modified - a single mode is dispersed over frequency $\Delta\nu$ in a volume V. This volume is defined as the spatial integral of the vacuum field intensity for the cavity mode, divided by its maximum value

$$V = \int\int\int_{space} \frac{|E|^2}{|E_{max}|^2}. \tag{1.2}$$

In his original work Purcell [Purcell, 1946] considered a localized dipole, at resonance with a single cavity mode of angular frequency ω_c and of linewidth $\Delta\omega_c = \omega/Q$, where Q is the quality factor of the cavity resonator. He quantified the increase of the emission rate by factor (later named the Purcell factor) F_p according to equation [Purcell, 1946]

$$F_p = \frac{\Gamma_c}{\Gamma_f} = \frac{\tau_f}{\tau_c} = \frac{3}{4\pi^2}\left(\frac{\lambda_c}{n}\right)^3\frac{Q}{V}, \tag{1.3}$$

where τ_f is the mean radiative time in free space and τ_c is the mean radiative time in cavity and $\frac{\lambda_c}{n}$ is the wavelength within the material. The Purcell factor describes the ability of coupling an ideal emitter with the vacuum field via a local amplification of field's intensity.

The cavity-induced modification of spontaneous emission rate can be derived from Fermi's golden rule by normalizing the cavity-enhanced mode density ρ_c per

unit volume to the mode density of free space ρ_f [Kleppner *et al.*, 1981].

$$\rho_f(\omega) = \frac{n^3\omega^2}{\pi^2 c^3}, \tag{1.4}$$

$$\rho_c(\omega) = \frac{1}{\Delta\omega V}, \tag{1.5}$$

$$\frac{\rho_c}{\rho_f} = \frac{\pi^2 c^3}{n^3\omega^2}\frac{Q}{\omega V} = \frac{1}{8\pi}\left(\frac{\lambda_c}{n}\right)^3\frac{Q}{V}. \tag{1.6}$$

This, up to a constant, yields the Purcell factor. It is clear that the ability of a cavity to alter the spontaneous emission rate depends on its properties expressed by the factor $\frac{Q}{V}$.

In real cavities we must additionally consider how the emitter is coupled to the vacuum field by correcting for the following factors:
- the position r of the emitter relative to the maximum of the cavity field ($\vec{\epsilon}_{max}$),
- relative orientation of the cavity electric field vector ($\vec{\epsilon}$) with respect to the emitter dipole $\vec{d}$,
- energy detuning of the emitter with respect to cavity,
- the emission rate through other recombination channels τ_{leaky}.

The corrected enhancement factor F can thus be written [Gérard *et al.*, 1998]:

$$F = F_p\frac{|\vec{\epsilon}(r)|^2}{|\vec{\epsilon}_{max}|^2}\left(\frac{\vec{d}\vec{\epsilon}}{|\vec{d}||\vec{\epsilon}|}\right)^2\frac{\lambda_c^2}{\lambda_c^2 + 4Q^2(\lambda_e - \lambda_c)^2} + 1/\tau_{leaky}. \tag{1.7}$$

1.2.3 Inhibition of spontaneous emission

Equation 1.7 indicates that for an emitter which is either detuned spectrally, spatially or its dipole moment is perpendicular to the cavity mode field there will be no enhancement of spontaneous emission rate. In such case, the spontaneous emission rate is governed by the coupling to the leaky modes with a rate of $\frac{1}{\tau_{leaky}}$. In a cavity with reduced coupling to leaky modes the τ_{leaky} may be increased, leading to an overall decrease of the spontaneous emission rate compared to free-space emission.

1.3 Quantum dots

Quantum dots (QDs) are nanometer-size semiconductor structures in which carriers are confined in all three spatial directions. As a result of the small confinement

volume energy spectrum of the carriers is quantized in shells of discrete levels. For this reason quantum dots are often called "artificial atoms". However, unlike single atoms which are difficult to isolate and manipulate, quantum dots excitons, that is electron - hole pairs, can be relatively easy accessed and manipulated both optically and electrically. This feature makes them interesting objects from the point of view of fundamental research and applications. If the barrier potential is high enough QDs enable also investigations of other localized quantum particles: charged excitons (two electrons and one hole or two holes and one electron), biexcitons (two electrons and two holes) and other many-body complexes. The quantum state of these particles can be "encoded" in photons in a straightforward manner by spontaneous emission recombination and thus one can transmit information about this state over long distances with little decoherence. For this reason QDs are advertised for their possible application in the emerging field of quantum information, where, among others, QDs can be used as sources of single photons on-demand and entangled photon pairs (for more details about these applications see section 1.4.4). Finally, semiconductor QDs are light sources offering important advantages, such as low power consumption and possibilities of integration with the existing electronics.

Methods of production of QDs include nanocrystals produced by chemical methods or by ion implantation, nanodevices made by state-of-the-art lithographic techniques and finally, self assembled QDs which I discuss in the present work.

Due to the advantages mentioned above extensive studies of QDs have been carried out for more than 15 years now, especially in self-assembled QDs systems grown by molecular beam epitaxy. However, despite all the advantages of QDs their applications and studies in regular, bulk semiconductor matrices are limited by a low probability of extracting the emitted photons from the sample, caused by internal reflection in the embedding barrier layer. Usually only less than 5% of light passes outside the matrix structure due to the total internal reflection at the semiconductor-air interface. Use of optical microcavities is an efficient way to overcome this limit.

1.4 Optical microcavities - state of the research

Advanced semiconductor epitaxial and lithographic techniques give recipes for enhancement and guiding of QDs photoluminescence by using optical microcavities. For instance, it was proven that micropillar cavities (for details see below) can achieve photon extraction efficiency of about 80% [Gazzano *et al.*, 2013a] as effect

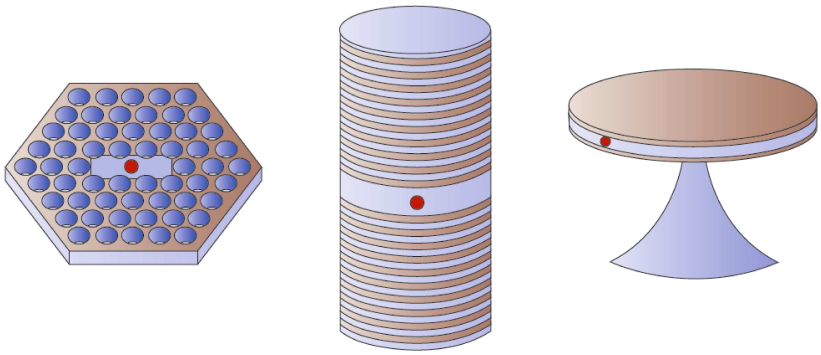

Figure 1.1: From left to right: photonic crystal, micropillar cavity, microdisc. The optimal position of QD, corresponding also to the place with maximal amplitude of the electric field oscillation is marked with red dot. From [Khitrova *et al.*, 2006].

of their highly directional emission profile and the Purcell effect [Purcell, 1946] [1]. Because of the enhanced efficiency in generation of photons optical microcavities are considered as key-elements in a number of quantum information schemes based on photons. They are also interesting from the point of view of the fundamental research. This is because confining photons in small volumes around quantum emitters leads to a variety of cavity QED effects resulting from an amplified light-matter interaction. Below, I summarize major achievements in the domain of semiconductor optical microcavities, starting with a brief overview of their available forms.

1.4.1 Types of semiconductor microcavities

Planar microcavities are constructed from cavity spacer layer embedded usually between two distributed Bragg reflectors (DBRs). DBR is a structure formed from multiple layers of materials with alternating refractive index. Their thickness is adjusted to equal quarter of the wavelenght of photons of a selected energy. Each layer interface causes a partial reflection of the optical wave. The consecutive reflections interfere constructively for photons of the selected energy. Planar cavities were originally developed for applications as Vertical-cavity surface-emitting lasers. The first VCSEL was presented in 1979 by Iga [Soda *et al.*, 1979] as an alternative for an edge-emitting laser. First VCSEL utilizing a DBR, made of alternating layers of GaInAsP/InP is dated on 1985 [Chailertvanitkul *et al.*, 1985]. Another milestone

[1] in this thesis I discuss schemes of further enhancing this efficiency by blocking the unwanted "leaky" emission channels, for details see chapter Micropillars with radial distributed Bragg reflectors.

achievement was the demonstration of the first full-monolithic VCSEL with epitaxial DBRs and those quantum wells by Jewell in 1989 [Jewell *et al.*, 1989].

Among cavities ensuring three-dimensional confinement the most intensively studied are micropillar cavities (discussed in detail in this thesis), photonic crystal cavities [Srinivasan *et al.*, 2003] and microdiscs, all three presented in Fig. 1.1. A micropillar cavity is etched from a planar microcavity using various techniques of microstructurization (for details see section 1.4.7). In such structure the confinement in the planar direction is assured by the reflection at the semiconductor-air interface. A 2D photonic crystal is formed of arrays of air holes etched in a planar semiconductor structure. Its stopband is formed at a wavelength which corresponds to half the optical path-length between the holes. A cavity (so-called defect-cavity) is formed by leaving out or shrinking the diameter of one or a few of the holes. Also 3D microcavities can be manufactured, using a half-wavelength-thick slab which ensures vertical confinement through total internal refection. Microdiscs are fabricated in a two-step wet-etching procedure [Michler *et al.*, 2000] and show whispering gallery modes [Gayral *et al.*, 1999].

We may arbitrary divide the current research with the use of semiconductor optical microcavities into three fields which focus on: enhancement and suppression of spontaneous emission, strong-coupling cavity quantum electrodynamics (cQED) and finally on development of sources of photons for applications in optical quantum communication schemes. Below I discuss these three fields in more detail.

1.4.2 Enhancement, guiding and inhibition of spontaneous emission

In the present generation of advanced optoelectronic devices, such as single and entangled photon sources or low-threshold microlasers it is desired to feed all the spontaneous emission into a controlled optical mode. This can be achieved by enhancing the spontaneous emission into the desired mode or inhibiting all the other emission channels. The most efficient method results from combining these two approaches. Below, I discuss achievements of both enhancing and inhibiting the spontaneous emission of semicoductor-based emitters.

Increase of the spontaneous emission rate

In a pioneering in the research of the increase of spontaneous emission Gérard and coworkers showed a five-fold Purcell enhancement. This was achieved in micropillar cavities with InAs quantum dots [Gérard *et al.*, 1996]. Recently, taking advan-

tage of such enhancement and efficient collection of emitted photons [Pelton *et al.*, 2002], InAs QDs in micropillar cavities were used as an ultra-bright source of entangled photon pairs featuring an entangled photon pair rate of 0.12 per excitation pulse [Dousse *et al.*, 2010].

Inhibition of the spontaneous emission

Stepping out from the field of semiconductors, the inhibition of spontaneous emission has been first demonstrated for Rydberg atoms [Hulet *et al.*, 1985] in a microwave cavity. In semiconductors, demonstration of pronounced inhibition was first achieved after major technological advancements. In planar semiconductor cavities lack of photonic bandgap in the horizontal direction results in enhancement and suppression of emission rates of emitters only on the order of 10% [Abram *et al.*, 1998; Tanaka *et al.*, 1995]. To inhibit the emission of QDs by a larger factor three-dimensional dielectric periodic structures were used [Lodahl *et al.*, 2004]. A recent record for inhibiting the spontaneous emission of QDs was reported for Tamm plasmon modes, where an inhibition of spontaneous emission by a factor of 40 was reported [Gazzano *et al.*, 2011].

In the case of standard micropillar cavities the inhibition of spontaneous emission is not observed [Gérard *et al.*, 1998; Lohmeyer *et al.*, 2006a], which is due to the so-called "leaky" emission through the sidewalls of the micropillars. The horizontal confinement is assured only by the reflection at the single semiconductor-air interface. However, it has been shown that the photonic bandgap for the light propagating in the transverse directions can be strongly enhanced by means of a silver coating of the micropillars [Poborchii *et al.*, 2003]. For such structures suppression of coupling to leaky modes and resulting inhibition of spontaneous emissio was demonstrated. Also large increase in acceleration of the spontaneous emission of QDs resonant with the cavity modes has been reported such metal-coated micropillars [Bayer *et al.*, 2001]. However, due to losses induced by the metallic coating this technique is not considered as optimal. In this thesis, in chapter Micropillars with radial distributed Bragg reflectors I describe our approach to inhibit the spontaneous emission in micropillar cavities. It is based on using radial Bragg reflectors to enhance the photonic bandgap in the radial direction.

Photonic nanowires featuring high extraction efficiency In all the examples mentioned above the focus is on enhancing a single-mode emission. In photonic

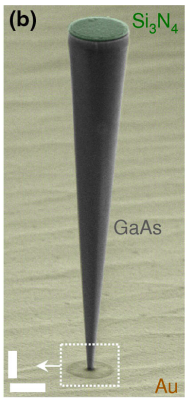

Figure 1.2: Scanning electron micrograph of a "photonic trumpet" (in false colors). Vertical and horizontal scale bars: 1 µm. From [Claudon *et al.*, 2010]

nanowires also broadband efficient spontaneous emission control is feasible and extraction efficiency (the probability for a photon to be emitted upwards) of 0.72 has been demonstrated in a nanowire with a tapered end [Claudon *et al.*, 2010] for InAs/GaAs QDs. In a similar system produced of CdSe/ZnSe efficient room-temperature single-photon source was demonstrated [Bounouar *et al.*, 2012]. More recently yet another approach has been proposed. The so-called "photonic trumpets" nanowires [Munsch *et al.*, 2013] (see Fig. 1.2) guide and expand a mode within a conical taper providing a nearly perfect coupling between an embedded quantum light source and a Gaussian free-space beam. Such Gaussian profile is favorable for all applications. Such design with a broad upper end of the wire offers important advantage in the possibility for defining a top electrode, which is not possible in standard nanowires. "Photonic trumpets" achieve extraction efficiency of up to 0.75.

1.4.3 Light-matter strong coupling

Photons interact with matter relatively little. This enables to coherently send information over long distances using photons. However, this advantage becomes disadvantage when it comes to conversion of photons to electronic excitation, necessary in many applications. The light-matter interaction can be effectively enhanced by confining photons in a small volume and for prolonged period of time to enhance the dipole light-matter coupling and photon absorption probability. This idea is realized in optical microcavities. In analogy to classical coupled oscillators, if the coupling rate between a cavity mode electromagnetic field and exciton exceeds the mean of their decay rates then the coupled system has two eigenenergies. For solid state microcavity this was first demonstrated in a planar microcavity containing

multiple quantum wells. The strong coupling between excitons confined in quantum wells (QWs) and electromagnetic field was observed in reflectivity spectra of such structures [Weisbuch *et al.*, 1992].

For a typical planar microcavity containing quantum wells around 90 photons per square micrometer has to be absorbed to saturate the normal mode coupling [Lee *et al.*, 2001]. The strong coupling regime is in its quantum limit if absorption of a single photon induces significant changes. This limit was first demonstrated in a micropillar cavity containing QDs with relatively large oscillator strength resulting from their enlarged size [Reithmaier *et al.*, 2004]. It was shown that the emission from such system is antibunched, which proofs that exciton transition in a single QD is responsible for the splitting [Hennessy *et al.*, 2007]. Another confirmation came from an experiment utilizing the four-wave mixing technique. Kasprzak *et al.* confirmed that coupled QD-microcavity systems can be considered as being in the quantum strong coupling regime and that it can be well described by the Jaynes - Cummings model [Kasprzak *et al.*, 2010]. A recent achievement on this field was the demonstration of a controlled coherent coupling of spatially separated quantum dots via the photon mode of a solid state microresonator [Albert *et al.*, 2013]. To achieve this all three coupled dots were in the strong exciton-photon coupling regime with the mode.

Since the first report on the Bose-Einstein like condensation of excitons-polaritons a few years ago [Kasprzak *et al.*, 2006] the main research interest in the domain of semiconductor cavities has been focused on the search for effects related to many-body coherence. During the recent years there have been reports on polaritons superfluidity [Amo *et al.*, 2009], quantized vortexes [Lagoudakis *et al.*, 2008] and finally, electrically driven polaritonic lasing [Bhattacharya *et al.*, 2013; Schneider *et al.*, 2013].

1.4.4 Generation and applications of single photons

Development of optical microcavities is to a large extend driven by their potential application in optical quantum information schemes basing on single photons. Quantum information science involves encoding, manipulation, transfer and finally read-out of information using quantum-mechanical objects. An example of application are photonic qubits, where information is encoded in the quantum state of the light quanta using its polarization (also momentum, energy and other degrees of freedom can be considered). Emission from quantum dots exhibits non-classical pho-

ton anti-bunching behavior required for single photon emission. By combining this feature with the ability to enhance and guide such emission by using cavity-related effects one obtains an efficient source of single photons [Pelton *et al.*, 2002].

For the past years the main drive for the development of single photon sources were also quantum cryptography protocols basing on key distribution by the use of single photons, such as the famous BB84 protocol [Bennett & Brassard, 1984]. Additionally, some quantum computation schemes also require single (and in most of the schemes entangled) photons, imposing the additional requirement of photon indistinguishability (*i. e.* identical wave packets).

1.4.5 Application as Vertical-cavity surface-emitting laser

The most successful commercial application of semiconductor optical cavities are vertical-cavity surface-emitting lasers (VCSELs). Their success stems from preferable lasing characteristics and relatively easy production. They can be densely packed as a large-scale two-dimensional arrays which can be tested without the necessity of further wafer processing. The lasing characteristics include single mode operation, narrow circular beam profile and ultra-low threshold. Due to all these advantages they found application in a large variety of fields including fiber optic communication, laser printers, pumping of solid state lasers, laser cutting, drilling and engraving (using high-power arrays) and so on. This variety of applications is best reflected in the fact that after Fabry-Pérot type edge emitting lasers (used in optical disk drives for data storage) VCSELs have the second largest production volume among all types of semiconductor lasers. The dynamic development of VCSELs is also strongly related to their applications in fiber-optic communications. The use of VCSELs as transmitters is highly favorable for their high coupling efficiency (approx. 50 %) into single-mode fiber, narrow spectral width which allows for high bit rates since it reduces the effect of chromatic dispersion, or finally achievable high frequencies of modulation, which result from short carrier generation and recombination time.

Major challenges in the construction of VCSELs include development of Bragg reflectors featuring the possibility of both n and p doping. Furthermore the materials should feature high refractive index contrast for reaching high Q-factor, without the necessity for growing many DBR pairs which results in a higher absorption rate. Of special importance is also the susceptibility of a material to electric current induced damage. These stringent requirements are particularly challenging to fulfill in the

II-VI material system, as described in more detail in section 1.5.2.

1.4.6 Low-threshold lasing

Lasers utilizing quantum dots as the active material are expected to bring improvements in semiconductor laser performance in terms of high gain and low lasing thresholds [Alferov, 2001; Strauf & Jahnke, 2011]. These advantages result, among others, from the discrete nature of energy states and localization of carriers. Additionally, in high Purcell factor cavities the emission is preferentially directed in one mode resulting in lowering of the number of degrees of freedom for the decay of an emitter. The fraction of photons emitted into such cavity mode is given by the expression $\beta = F_P/(F_P + 1)$, where F_P is the Purcell factor associated to this mode. Progress in the growth and design of photonic crystals and micropillar microcavities led to β factors close to unity [Strauf *et al.*, 2006; Ulrich *et al.*, 2007]. The lasing threshold is no longer well defined in such case, as there is no abrupt transition from thermal to coherent radiation with the increased pumping power. The device shows lasing-like characteristics for all pumping power values, however small they are. Particularly interesting is the limit of a single QD-cavity system, as only very few photons are involved in the lasing process. Presently low threshold lasers constitute an active field of research.

1.4.7 Micropillar cavities - details

Micropillar cavities are typically based on planar microcavities grown by molecular beam epitaxy (MBE) or metal-organic vapor phase deposition (MOVPE). In order to provide confinement in the planar directions structures are further processed into micropillars. Their planar cross-section is usually circular, although elliptical cross sections are also produced, depending on the desired properties related to polarization of the emitted light (for more details see chapter Purcell effect in quantum dot). The etching technique has to fulfill stringent requirements: yield structures of high aspect ratio and yield low damage leading to smooth and vertical pillar sidewalls. More about micropillar etching can be found in section 2.3 in chapter Technology and samples.

Micropillar cavities combine small microcavity volume with relatively high Q. They have an emission pattern that is well suited for manipulation and coupling of emitted photons with, for example, optical fibers. Additionally they offer the possibility to incorporate quantum wells and quantum dots as emitters. The latter

may be also positioned in a deterministic way on the micropillar axis [Dousse *et al.*, 2008]. In application of micropillars as vertical-cavity surface emitting lasers the reduced active area and reduced mode volume, compared to planar microcavity, result in decrease in threshold excitation power density for lasing. Finally, micropillar cavities might incorporate a p-n junction and can be electrically contacted [Böckler *et al.*, 2008].

All the mentioned features make micropillar cavities one of the best candidates for both applications and fundamental research of light-matter coupling and for these reasons they became one of the most investigated optical cavities in the recent years. Semiconductor quantum dot in a micropillar cavity proved to be a source of bright single photons [Santori *et al.*, 2002]. Also state-of-the-art entangled photon pairs have been generated in a system of two coupled micropillar cavities (so called *photonic molecule*)[Dousse *et al.*, 2010], where InAs QDs in micropillar cavities were used as an ultra bright source of entangled photon pairs reaching a record polarization entangled photon pair rate of 0.12 per excitation pulse (more details on this experiment can be found in section 1.4.7). Entangled photons are required in most of quantum computation schemes [Bouwmeester *et al.*, 2000] and are key components of quantum teleportation schemes [Bouwmeester *et al.*, 1997]. A canonical entangling gate - the controlled-not (C-NOT) gate flips the state of a target qubit depending on the state of the control qubit. Recently such gate basing on micropillar cavity was demonstrated [Gazzano *et al.*, 2013b]. Indistinguishable photons were used as target and control qubits.

Up to now, the major research efforts were focused on micropillars (and planar cavities) based on the III-V materials, mainly III-arsenides and -phosphides. The combination of materials include primarily AlAs/GaAs and AlP/GaP due to their low lattice mismatch what enables to grow thick samples without defects. Additionally, the technology of doping in this materials is well developed so that DBRs can be both n or p-doted.

Over the last decade major achievements in the development of micropillar cavities were record Q-factors of up to 165.000 [Reitzenstein *et al.*, 2007] achieved in the AlAs/GaAs material system, highly efficient lasing [Reitzenstein *et al.*, 2006] and electrical pumping of high-Q QD micropillars [Böckler *et al.*, 2008]. An exhaustive review on micropillar cavities can be found in [Reitzenstein & Forchel, 2010], however it doesn't cover the most recent advancements in this field, some mentioned below.

InAs QD in micropillar cavities was used as an ultra bright source of entangled

photon pairs [Dousse *et al.*, 2010]. In this experiment, biexciton and exciton energy states of a preselected quantum dot were coupled to two different photonic modes of a photonic molecule made of two micropillar cavities. The Purcell effect improved the indistinguishability of the two optical recombination paths compensating the anisotropic exchange splitting of the exciton. Additionally the entangled photon pairs were emitted into photon modes providing outstanding efficiency in collection of the emission. Micropillar cavities were reported to show brightness (see 1.4.7 for) reaching 80% [Gazzano *et al.*, 2013a] for a carefully designed QD-micropillar device. This two achievements clearly illustrate the potential of micropillars for applications and scientific research.

Important parameters of micropillar cavities

Quality factor Quality factor Q is a crucial parameter determining the strength of interaction of the microcavity electromagnetic field of an mode with the emitter.

The Q-factor of planar microcavity depends on the number of Bragg reflector pairs, their refractive index step and absorption of the microcavity and reflectors. Neglecting absorption to a first approximation, Q can be expressed by the reflectivity of the lower (r_l) and upper (r_u) DBRs [Schubert, 2006] as

$$Q \propto \frac{1}{1 - r_l r_u}. \tag{1.8}$$

This equation indicates that Q increases with increasing reflectivity of the Bragg reflectors. However, in real microcavities an increase in reflectivity obtained by use of an increased number of Bragg pairs results in higher absorption rate. This is because prolonged decay time of the photon from microcavity and huge thickness of the DBRs results in a higher absorption probability of the photon before leaving the structure. Thus, designing the optimal number of Bragg pairs requires balancing those opposite effects. Numerical simulations based either on the extended transfer matrix method or finite-difference time-domain (see chapter Basic optical properties of planar and micropillar cavities for more details on those methods) are often used to find the optimal design.

Q-factor of a micropillar cavity depends on the reflectivity of the DBRs, absorption and edge scattering. For large Q values the total quality factor can be conveniently written as a sum of various scattering factors [Rivera *et al.*, 1999], such as :

$$1/Q = 1/Q_{\text{intrinsic}} + 1/Q_{\text{edge scattering}} + 1/Q_{\text{absorption}}. \tag{1.9}$$

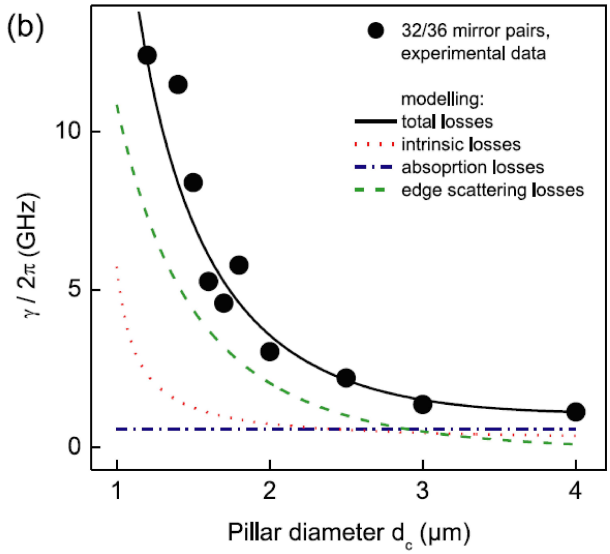

Figure 1.3: Loss rates versus the micropillar diameter for micropillars with 32/36 mirror pairs in the AlAs/GaAs system. The total loss rate is composed of intrinsic, absorption and edge scattering losses. Figure from [Reitzenstein *et al.*, 2007].

Here, $Q_{intrinsic}$ denotes a quality factor of an perfect microcavity without absorption ans sidewalls scattering. The edge scattering denotes losses due to imperfections of the sidewalls related to the etching process. Absorption is dependent on the absorption of the microcavity and DBR materials. An example of how these components contribute to the Q-factor of a micropillar cavity is presented in Fig. 1.3 [Reitzenstein & Forchel, 2010], where the factors were divided into those three categories. The edge scattering becomes more pronounced in the small diameter range due to the increase of the relative area of the sidewalls of the microcavity with respect to the area of its interface with the DBRs. The reduction of the $Q_{intrinsic}$ is due to radiative losses related to a reduction of the bandgap and a blue shift of the microcavity mode away from the center of the photonic bandgap [Vučković *et al.*, 2002].

For small diameters the micropillar Q-factor exhibits an oscillatory variation as a function of the micropillar diameter [Lalanne *et al.*, 2004; Lecamp *et al.*, 2007]. As showed by simulations [Lalanne *et al.*, 2004] this results mainly from the hybrid character of the cavity mode in the small diameter limit. The guided modes of the microcavity layer couple to modes with different numbers or radial and azimuthal nodes in the Bragg mirrors. This issue, which deteriorated the quality factor of the modes was overcomed in micropillar with tapered refractive index profile across the microcavity, where the fundamental Bloch mode[1] is subject to an adiabatic

[1]The analysis of electromagnetic fields in periodic media shares the same concepts as analysis of electrons in periodic potentials - such as Bloch modes in analogy to Bloch waves

transition to match the Bragg mirror Bloch mode [Lermer *et al.*, 2012].

Brightness The brightness of a source is defined as the number of collected photons in the first lens per excitation pulse. It is given by the product

$$\beta\,\eta\,Q_{QD}, \tag{1.10}$$

where η is the fraction of photons emitted in the mode that are not scattered or absorbed (and thus leave the structure within that mode) and q_{QD} is the quantum efficiency of the QD emission line. β is defined earlier, in section 1.4.6). η is given by the ratio of the intrinsic losses to the total losses of a micropillar. Using equation 1.9 we may write

$$\eta = \frac{1/Q_{\text{int.}}}{1/Q} = \frac{Q_{\text{abs.}}Q_{\text{edge scat.}}}{Q_{\text{abs.}}Q_{\text{edge scat.}} + Q_{\text{abs.}}Q_{\text{int.}} + Q_{\text{int.}}Q_{\text{edge scat.}}}. \tag{1.11}$$

1.5 Vertical cavities and emitters based on wide-bandgap materials

Wide-bandgap compounds offer optical transitions in the visible spectrum in contrary to the III-V GaAs and InAs based heterostructures, which give infrared photoluminescence. In particular, green spectral region is hardly accessible for the III-V's, but it can be easily achieved for the II-VI's (e.g. ZnSe). In wide-bandgap materials exciton and biexciton have feature also greater binding energies which makes the excitons and their coherent states more robust. It allows the emitters to function at higher temperatures compared to the classical III-V ones [Sebald *et al.*, 2002]. Wide-bandgap materials are also characterized by shorter radiative lifetimes.

Optical microcavities have been developed mainly basing on semiconducting compounds from the III-V groups, in particular arsenides. This section gives an overview on the wide-bandgap materials-based vertical cavities designed for emitters covering the visible and UV part of the electromagnetic waves spectrum.

The term wide-bandgap refers to materials of bandgap larger than the commonly used silicon (1.1 eV) and Gallium Arsenide (1.4 eV), that is mainly II-VI materials and III-nitrides. Besides advantageous spectral characteristics as light emitters the wide bandgap materials feature also more stable high-temperature operation due to a large carrier confinement, as compared to the III-V materials.

From the point of view of potential applications, emitting in the spectral range

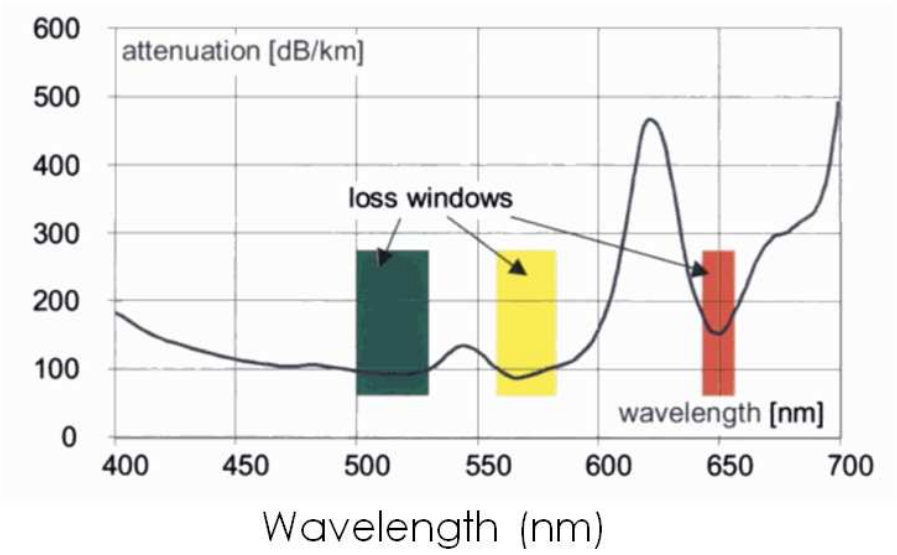

Figure 1.4: Spectral loss in a Poly(methyl methacrylate) (PMMA) step index profile fiber. From [Daum, 2002]

from green to orange this material is of particular interest for data communication using plastic optical fibers since they exhibit a minimum of the light absorption in that region [Daum *et al.*, 2002] (see Fig. 1.4). Plastic optical fibers have comparatively high attenuation and distortion characteristics. However this is not an issue in low-speed and short-distance (up to 100 meters) applications and therefore, as being the cheapest option, plastic fibers are commonly used in these applications. The Te-based II-VI semiconducting compounds, in particular emitters based on CdTe/ZnTe low-dimensional heterostructures, bridge the so called "yellow efficiency gap" [Mueller-Mach *et al.*, 2009a] showing a high efficiency in the green to orange spectral region [Karczewski *et al.*, 1999; Kobak *et al.*, 2013; Nomura *et al.*, 2006b; Pimpinella *et al.*, 2011; Tinjod *et al.*, 2004; Wojnar *et al.*, 2011]. The peak sensitivity of human eye is in this region. For this reasons potential VCSELs could find application as compact high-efficiency lasers in projection TV, pointing and alignment devices, laser location etc.

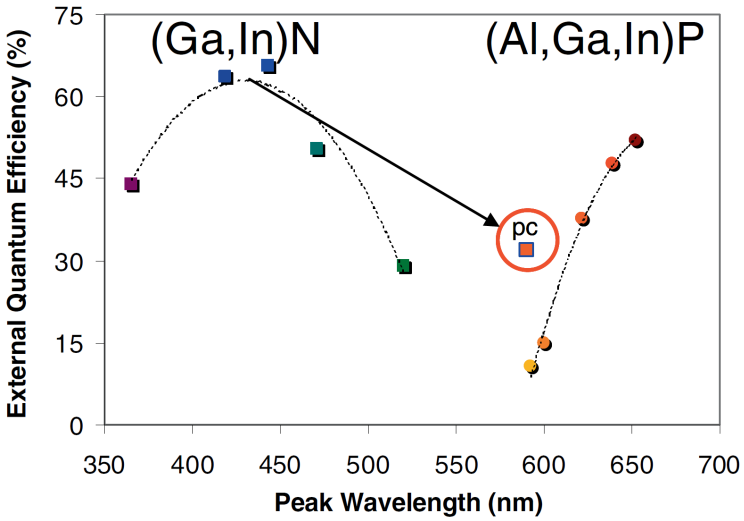

Figure 1.5: Decrease of external quantum efficiency versus emission wavelength termed the "'yellow gap"' [Krames *et al.*, 2007]. The extra point "pc" refers to emission based on photon conversion. From [Mueller-Mach *et al.*, 2009b]

1.5.1 State of the art

Nitride-based

This material system covers emitters in the blue - violet spectral range. A canonical system for the construction of vertical resonators is based on the combination of GaN/AlN pairs used in DBR construction. The index contrast for this pair is about 0.4 what ensures above 99% reflectivity for 16 Bragg pairs, although a lattice mismatch over 2.5% reduces significantly the crystalline quality of the structures. For this reason $Al_xGa_{1-x}N$ layers are used to lower the lattice mismatch. High quality vertical resonators were also achieved with the use of $Al_xIn_{1-x}N$ layers, that can be grown lattice-matched to GaN if the content of In is close to 17% [Carlin & Ilegems, 2003]. This combination was used in the construction of nitride-based monolithic micropillar cavities [Sebald *et al.*, 2010]. Finally, room temperature strong exciton-photon coupling was demonstrated for (AlIn)N/(AlGa)N-based cavities with GaN/(AlGa)N quantum wells [Christmann *et al.*, 2006].

II-VI based

In the 1995 strong coupling was reported for microcavities with (Zn,Cd)Se/(Zn,Mg)(S,Se) quantum wells and dielectric Bragg mirrors made of SiO_2/TiO_2. A Rabi-splitting

of 17.5 meV at 70 K [Kelkar *et al.*, 1995] was observed in this system. Later a Rabi-splitting of 23.6 meV and 44 meV at 300 K were demonstrated for a (Zn,Cd)Se/ZnSe quantum well sample sandwiched between SiO_2/Ta_2O_5 DBRs [Curran *et al.*, 2007] or ZnS and YF_3 DBRs [Pawlis *et al.*, 2003], respectively. A more detailed overview of the research is given by [Sebald *et al.*, 2009]. However, in the case of II-VI based vertical resonators probably the most widely recognized are works on CdTe-based monolithic structures. The main motivation was to utilize II-VI larger oscillator strength and larger exciton binding energy as comparing to GaAs-based compounds. Such features increase the exciton-polariton stability and Rabi-splitting. CdTe multiple Quantum wells enclosed in a (Cd,Mg)Te/(Cd,Mn)Te microcavity developed and investigated by André et coworkers [André *et al.*, 2000] showed Rabi splitting up to 30 meV at room temperature. This lead to a first demonstration of a Bose-Einstein like condensation in a solid state system by Kasprzak et coworkers [Kasprzak *et al.*, 2006].

For the CdSe/ZnSe emitters a DBR based on ZnSe for the high-refractive index and a short-period MgS/ZnCdSe superlattices for the low-refractive index material was developed [Kruse *et al.*, 2002]. MBE growth of such planar, monolithic microcavities, followed by FIB processing resulted in first II-VI based micropillar cavities yielding three-dimensionally confined optical modes possessing high quality factors [Lohmeyer *et al.*, 2006b]. Finally, an Purcell enhancement by a factor of up to 3.8 of the spontaneous emission rate of quantum dots coupled to the micropillars discrete optical modes was demonstrated [Lohmeyer *et al.*, 2008]. In further steps a green-light emitting monolithic VCSEL was created with the incorporation of CdSe/ZnSe quantum wells into micropillar resonator. On this structure, under pulsed optical pumping, single-mode stimulated emission near room temperature has been achieved [Kruse *et al.*, 2008]. For this system a systematic decrease in threshold excitation power for decreasing micropillar diameter was found. This effect results from the reduction of the active area combined with a decrease of the mode volume [Kruse *et al.*, 2008].

ZnTe-based distributed Bragg reflectors

In the literature, apart from the superlattice approach presented in this thesis, there exists only few reports on realization of ZnTe-based Bragg reflectors, all based on the use of a quaternary (Zn,Mg)(Te,Se) alloy [Nomura *et al.*, 2004; Ueta & Hommel, 2002]. The composition of materials is adjusted to keep the same lattice parame-

ter as ZnTe. Ternary and quaternary compounds require precise calibration of the growth parameters. Much easier in fabrication is the recently developed superlattice-based distributed Bragg reflector (DBR) [Pacuski *et al.*, 2009] lattice-matched to ZnTe [Kruse *et al.*, 2011]. We used it in construction for the all the cavities investigated in this thesis. This DBR contains ZnTe layers as the high refractive index material and a short-period superlattice consisting of MgSe, MgTe and ZnTe layers as the low index material. These layers have a relatively large refractive index step of $\Delta n = 0.48$ ($n_{ZnTe} = 3.08$ [Marple, 1964], $n_{SL} = 2.6$ [Pacuski *et al.*, 2009] at the photon energy of 2050 meV), which allows for the use of an efficient top DBR with a small total thickness resulting in a relatively low level of absorption of the excitation laser beam.

MgSe has a lattice parameter smaller than ZnTe, MgTe larger than ZnTe (see Fig. 1.6). Therefore, in the considered DBR the lattice mismatch of ZnTe and SL is compensated by using a defined thickness ratio of MgSe and MgTe layers. This is much easier than balancing the strain by controlling the content of a ternary or quaternary compound, as it was done in previously reported approaches. MgSe and MgTe layers are separated by very thin ZnTe layers, which are neutral with regard to strain and lattice parameter.

The development of such DBR by Wojciech Pacuski opened a whole new area of research on ZnTe-based photonic structures, which became an interesting topic for my Ph. D. thesis.

1.5.2 Toward applications - major challenges and obstacles

Vertical cavities are closely related to applications, as VCSELs constitute an important part of solid state lasers market. Other applications seem to have a relatively long way to commercialization. I briefly summarize here the major issues related to applications of II-VI based optical microcavities.

The first II-VI based edge emitting laser diode operating in the blue-green spectral range was demonstrated in the early 90's [Haase *et al.*, 1991]. Significant efforts in the development of II-VI heterostructures led to demonstration of green laser diodes with lifetimes as long as 400 hours [Kato *et al.*, 1998]. However, current induced degradation of the structures came out to be the major obstacle on the way to commercialization. Furthermore the breakthrough in III-nitrides based laser diodes which achieved many thousand hours under continuous-wave room temperature operation [Nakamura *et al.*, 1998] led to a significant decrease in the interest

in the development of II-VI based light emitters.

After Itoh *et al.* [2000], responsible for the degradation are mainly stacking fault defects originating at the the interface between the substrate (usually GaAs) and the deposited II-VI material. Another origin of defects which is mentioned in the literature is related to carrier recombination-enhanced defect reactions in the active region [Hovinen *et al.*, 1995; Kimerling, 1978]. Further problem of the II-VI materials which hinders their commercial application is the difficulty of controlling the conductive type. This is because of commonly occurring native defects. These defects can have either a donor or acceptor character, or even be amphoteric, and they act as compensating centers.

One of the most important usage of II-VI semiconductors is as infrared radiation detectors. HgCdTe has a unique property among common materials which is the ability to detect infrared radiation in both atmospheric windows. These are wavelengths from 3 to 5 µm and from 8 to 12 µm.

In regard of potential and existing large-scale application of the II-VI materials the availability of the key elements is good, with the exception of tellurium which is present in the earth's crust at a level comparable to platinum. However, a potential barrier for applications is toxicity of cadmium and its compounds. For this reason in many regions of the world there is now a restriction or ban on the use of heavy metals in many household goods which means that most cadmium based quantum dots are unusable for consumer-goods applications. The European Union banned the use of cadmium in electronics, with only several exceptions.

Summarizing, although II-VI materials certainly have a potential for applications, their way to the market still seems to be quite long. This view is best reflected in the fact that currently marketed green-orange diodes are made of such compounds as (Ga,As)P, (Al,Ga)P, (Al,Ga)InP and GaP, despite their relatively low efficiency at these wavelengths. Concerning green lasers, the III-nitrides based quantum well laser diodes operating at 533 nm [Adachi *et al.*, 2010] have parametrers that are still not matching the requirements of projector devices. As stated by Nichia by the end of 2012 high-power pure green laser diode was achieved by the optimization of epi-structures based on c-plane GaN substrates. They might be the first ones to be used in display application, such as long foreseen Laser TVs. Despite this, alternative approaches, such as optical or electron beam pumping are taken to overcome the degradation problems in II-VI materials.

Electron beam pumped lasers The difficulties obstructing commercialization of II-VI laser diodes have fundamental character and therefore approaches alternative to electrical pumping are necessary. Electron beam pumped (EBP) laser is one of them. It requires neither doping nor ohmic contacts and the active region can be significantly enlarged, what makes it favorable for high-power applications. Available compact electron beam sources allow for scanning of the electron beam across an macroscopic area of the sample. This helps in avoiding creation of defects resulting from prolonged exposition of a single spot to the beam. ZnSe-based electron beam pumped laser has been showed as early as in 1967 [Bogdankevich *et al.*, 1967]. Major progress in the optimization of laser parameters was obtained using edge-emitting lasers with ZnSe-based heterorstructures such as (Zn,Cd)Se quantum wells [Herve *et al.*, 1995] or (Zn,Mg)(S,Se) QDs [Zverev *et al.*, 2002]. Interesting results were obtained recently at the University of Bremen where Klein *et al.* showed continuous-wave operation of an electron-beam pumped vertical-cavity surface emitting laser based on (Zn,Cd)(S,Se) quantum well in Zn(S,Se) matrix with the output of 5,9 W at 530 nm. More recently, a similar laser operating at 460 nm with an output power of 3,3 W was developed [Klein *et al.*, 2014]. It was based on ZnSe quantum well in (Zn,Mg)(S,Se) matrix

What hinders laser-based display technology is lack of green laser diodes providing the required power (several Watts) at room temperature with an adequate lifetime. Therefore, the structures developed by Klein *et al.* gain interest from potential investors. The low-cost of production of such tubes would compensate their limited lifetime.

Optically pumped lasers Another possibility for the development of II-VI lasers, which helps in avoiding the current-induced degeneration, is the optical pumping. However, the commercialization of devices utilizing such pumping is hindered by the need for compact and efficient pumping sources. Nevertheless, there have been interesting achievements on this field. First, (Zn,Cd)Se/(Zn,Cd,Mg)Se graded-index separate confinement heterostructure with a single quantum well showed lasing at 512 nm [Guo *et al.*, 1997], although with a relatively high pump power threshold required for the lasing. This threshold was significantly lower for structures with (Be,Zn)(Se,Te) as active material and MgSe/(Be,Zn)Te superlattice cladding layers. These structures were fabricated on InP substrates, featuring green lasing emissions at 548 nm at room temperature [Nomura *et al.*, 2009]. Also (Be,Zn)(Se,Te) active layer grown on InP showed lasing in the wavelengths range from 538 to 570 nm at

room temperature [Nomura *et al.*, 2011]. High efficiency lasing was reported for VCSELs based on ZnSe described in one of the previous sections [Kruse *et al.*, 2008] (see section 1.5.1). Finally, the microcavities investigated in the presented work, combined with quantum wells, are expected to show favorable lasing characteristics (especially emission in the yellow-orange spectral range) .

1.6 Aim of this work

The presented work aims at developing the microcavity technology for CdTe/ZnTe QDs and other ZnTe-based emitters providing new tools for the research on carriers confined in these QDs and opening the way for exploring cavity quantum electrodynamics effects in this material system. Of special interests are QDs containing solitary dopants, like single-atom magnetic impurities. Finally, our aim is to develop cavities for vertical cavity surface emitting lasers pumped either optically or with electron beam. In the first step we want to provide a detailed characterization of the new ZnTe-based photonic system featuring planar and micropillar cavities [Kruse *et al.*, 2011; Pacuski *et al.*, 2009]. In parallel we want to optimize the structures, using characterization measurements as feedback about the properties of obtained structures.

1.6.1 Background and motivation

Having available high reflectivity distributed Bragg reflectors (DBRs) [Pacuski *et al.*, 2009] a realization of highly efficient light sources, like monolithic vertical-cavity surface-emitting lasers (VCSELs) and resonant-cavity light emitting diodes radiating in this range can be realized based on the CdTe/ZnTe system. Moreover, QDs containing single Mn (or other solitary dopants) ions incorporated into a high-quality microcavity allows to introduce a spin of localized magnetic atom as additional degree of freedom. The need of the preparation of the defined quantum state of QD for applications based on quantum manipulations makes the studies of the QD excitation very important. Last but not least, the most common single photon detectors based on avalanche diodes made of silicone have best efficiency (up to over 70%) at the visible wavelengths around 600 nm [Thomas *et al.*, 2010], and this decreases dramatically for longer wavelengths.

The development of the microcavity technology for the II-VI materials is also motivated by the existence of a mature technology of diluted magnetic semiconduc-

tors (DMS) in this material system, which is a traditional field of research of the commonly named "semimagnetic". Interesting properties of such heterostructures, as those made of (Cd,Mn)Te, combined with a good knowledge of the interactions and material constants in this materials sets interesting perspectives if the research possibilities were extended with the tools provided by optical cavities.

For a long time, cavity effects were not used in exploration of II-VI QDs due to a lack of suitable microcavities. A significant progress on fabrication and optical study of II-VI microcavities has been achieved few years ago in two leading laboratories: in Grenoble, and in Bremen, in group of Prof. D. Hommel. Enhanced spontaneous emission rates have been observed for CdSe QDs embedded in hybrid micropillar [Robin *et al.*, 2005] and monolithic micropillar microcavities [Lohmeyer *et al.*, 2006a]. This is related to the Purcell effect, resulting from strong coupling between QDs transitions and micropillar modes. The strength of the coupling depends on quality of microcavity-mirror interfaces and precision of the etching. In Bremen, growth of II-VI Bragg mirrors was motivated by the development of VCSELs [Kruse *et al.*, 2004].

Although developed only recently [Jakubczyk *et al.*, 2009; Kruse *et al.*, 2011], ZnTe based micropillar cavities have proven to have very good photonic properties. The Bragg reflector, on which the micropillars are based, shows over 99% of reflectivity only for 15 Bragg mirror pairs [Pacuski *et al.*, 2009]. Both single QD lines and cavity modes were successfully identified in this structures [Jakubczyk *et al.*, 2009] and modes with quality factors of up to 3700 were observed [Kruse *et al.*, 2011].

1.6.2 Basic physical properties of the material system

The II-VI compounds, in semiconductor research limited almost entirely to such materials as MgO, MgS, MgSe, MgTe; ZnO, ZnS, ZnSe, ZnTe; CdS, CdSe, CdTe, HgS, HgSe, HgTe and mixed compounds. The majority of these materials crystallize in either the cubic zinc-blende (beta) phase or the hexagonal wurzite (alpha) phase, where one or other of those phases is thermodynamically more stable at 300 K. MgO, MgS, MgS have rock salt structure, however can be epitaxially grown in zincblende structure for limited thickness. MgTe has wurtzite structure if no high pressure is applied.

The group VI elements are considerably more electronegative than group V elements. Therefore the II-VI materials have more ionic (*i. e.* less covalent) bonds than the III-Vs. Larger bandgap of II-VI compounds as compared to those of the cova-

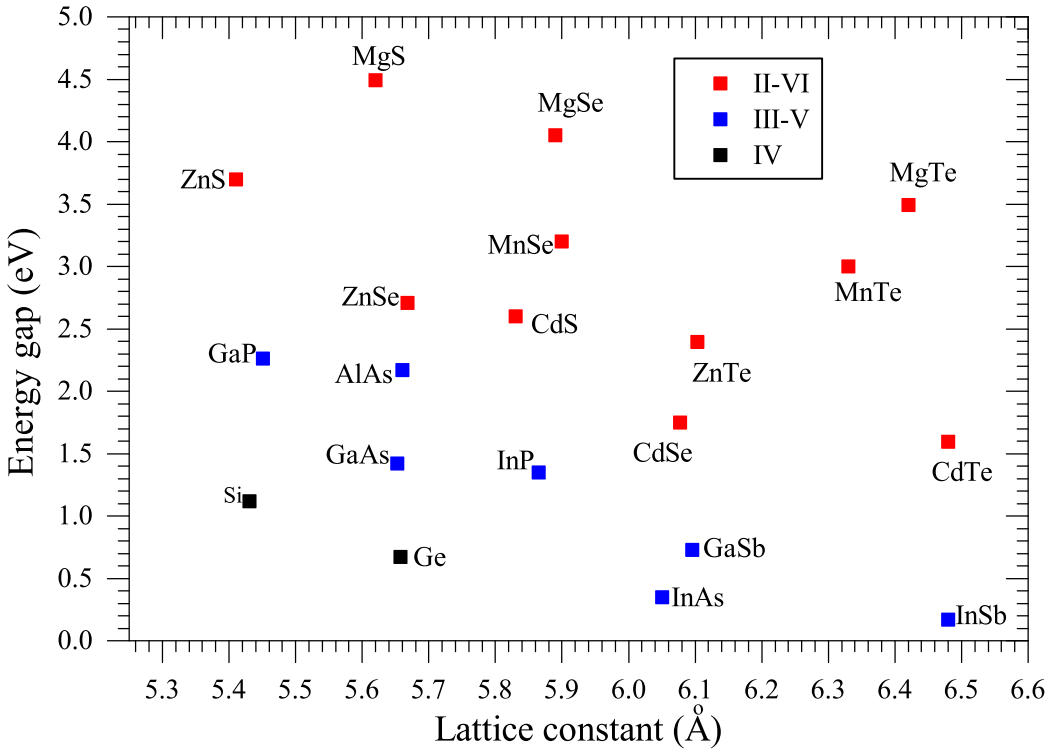

Figure 1.6: Energy gap vs lattice constant of various semiconductors. Various sources, [Marple, 1964].

lent semiconductors of comparable lattice constants is related to this ionic character. The bandgaps cover energies from almost zero (HgTe) through infrared (CdTe) to ultraviolet (MgS, ZnS, MgSe) spectral range , while the combination of ZnSe, CdSe, CdS and ZnTe covers the visible. All the materials have a direct bandgap, except mercury compounds (some of these are classified rather as semi-metals).

II-VI based heterostructures, compared to those made of III-V materials have favorable optical characteristics: comparably large carrier confinement advantageous for high temperature operation, large oscillator strength and large exciton-biexciton separation. II-VI materials typically have also stronger exciton-phonon interactions than III-V materials.

Epitaxial growth of wide-bandgap II-VI compounds can be carried out using such methods as liquid-phase epitaxy (LPE), Vapor-phase epitaxy (VPE), hot-wall epitaxy (HWE), metalorganic chemical vapor deposition (MOCVD) or metalorganic phase epitaxy (MOVPE), atomic-layer epitaxy (ALE) or metalorganic molecular-beam epitaxy (MOMBE). However, in the construction of high-quality heteroepitaxial structures with atomic layer deposition precision and the possibility of constructing materials far from their thermodynamically stable phase the molecular-beam epitaxy is a technique of choice (for more details see the description of the technique in chapter Technology and samples). For completeness I mention the techniques of the growth of bulk II-VI materials: chemical vapor transport (CVT), physical vapor transport (PVT), hydrothermal technique, Bridgmann and Gradient Freezing (GF) Method and The Traveling Heater Method (THM). The Warsaw semiconductor-researchers community is familiar with the Bridgmann method utilized by prof. Andrzej Mycielski in the construction of outstanding quality CdMnTe crystals used in the construction of X-rays and gamma detectors.

Structures investigated in the presented thesis are prepared at temperatures of the orders of several hundreds of $\circ$C and then are cooled down to few K for optical investigations. The technique of covering samples with oxide layers described in chapter Micropillars with radial distributed Bragg reflectors requires a closer analysis of temperature induced strains and for those reasons I enclose below a table of thermal expansion coefficients of those materials.

Table 1.1: *Selected thermal expansion coefficients of materials constituting samples investigated in this work. Values at 300 K*

Material	$[10^{-6}K^{-1}]$
GaSb	6.35 [Adachi, 2009]
ZnTe	8.33 [Adachi, 2009]
GaAs	5.75 [Adachi, 2009]
Alumina	5.4 [Hayashi *et al.*, 2005]
YSZ	5-10 [Hayashi *et al.*, 2005]

Chapter 2

Technology and samples

Majority of the effects investigated in this work rely on interference of light in thin dielectric layers. For this reason the required precision for the production of structures is preferentially greater than quarter-wavelength of the wave in matter, which is below 50 nm in the considered ZnTe-based system. Even more stringent requirement occurs in the production of quantum dots, as quantization effects related to confinement of electrons and holes become apparent when the motion of carriers is restricted to a region comparable to their de-Broglie wavelength. This corresponds to 23 nm in the CdTe system [Marple, 1963]. However, planar epitaxy is not designed to construct three dimensional traps for carriers (i. e. quantum dots) as this requires deposition of CdTe material selectively on surfaces with precision comparable, again, to several nm (approx. lateral size of a CdTe/ZnTe QD). This is also below limits of conventional lithography techniques. At this point, we have to use "tricks" to force atoms into forming islands of one semiconductor on an other semiconductor, like i. e. self-assembled CdTe QDs in ZnTe matrix. As described in more details in section 2.4.1, they form in self-organization processes resulting from strain related to layers lattice-mismatch and triggered by deposition of amorphous tellurium [Tinjod *et al.*, 2003].

The only practically relevant crystal growth methods fulfilling the above mentioned requirements are molecular beam epitaxy (MBE) and metal organic vapor phase epitaxy (MOVPE). They offer high-precision growth capabilities and possibility to grow materials which are far from thermodynamic stability. This allows to produce monolithic structures combining high quality Distributed Bragg Reflector and layer with quantum dots.

2.1 Molecular beam epitaxy

MBE has been developed since the late 60's as a versatile technique for growing thin heteroepitaxial structures made of semiconductors, insulators and metals. In a MBE process elements used for growing the crystal are evaporated from individual cells containing typically one of the elements each. As ultra-high-vacuum (UHV - below 10^{-9} mbar) is kept in the chamber the mean free path of the evaporated atoms largely exceeds the dimensions of the chamber, so the materials reach wafer usually without scattering . The necessity for such UHV is caused by the desired purity of the produced crystals.

The gaseous elements arrive to the wafer, where they may react with each other. The typical growth rate is around 1 monolayer/s (approx. 1μm/h) which ensures sufficient surface migration of the deposited atoms, leading to a smooth surface of the grown film. The kinetics of the reaction is controlled by the the beam fluxes of the deposited elements and additionally by the temperature of the samples surface. As in typical MBE growth the materials are deposited simultaneously the ratio of the fluxes plays a crucial role in the control of the growth of the crystal. For example, for the binary II-VI elements the highest crystalline quality can be obtained in a stoichiometric growth. The elements from the group VI have a higher vapor pressure and lower adhesion coefficient and therefore it is convenient to perform the growth supplying more atoms of group VI.

MBE is carried far from the thermodynamical equilibrium which implies that the produced materials are thermodynamically unstable (i. e. they are not in their lowest energy state). A particle, after hitting the substrate might be incorporated, desorbed or may move across the surface with a mean free path dependent on the substrate temperature. By setting the temperature sufficiently low one can incorporate elements beyond their solubility limit. This is used in the production of diluted magnetic semiconductors (DMSs). This feature is also of special importance for doping of II-VI materials, where compensation mechanisms by native defects prevents from n-type or p-type doping in equilibrium conditions.

2.1.1 Molecular beam epitaxy reactor

One of the most important components in an MBE system are effusion cells, each equipped with a shutter which allows to completely blend the flux. Different materials in ultra pure form, each in different crucible, are heated until they begin to sublime (typically in temperatures between $200-400\,^{\circ}\mathrm{C}$ for the materials in the pre-

sented work). The cells are fitted with thermocouples to allow closed-loop feedback control of the crucibles. In Knudsen-type cells the atom flux is controlled solely by temperature. With high vapor pressure materials, like Te or Se, a small fluctuation in temperature may create a large fluctuation in deposition rate. Therefore long stabilization of the cell temperature is required to obtain stable flux of atoms, which is not always favorable in applications, especially if the flux has to be varied during growth of a structure. For this reason some cells are equipped with a valve located near their end to reproducibly control and rapidly change the beam flux. The valve is heated to prevent deposition of the evaporated material.

The majority of the elements used in MBE provide a beam of atoms when heated, although some evaporate as molecules instead, like for instance tellurium and selenium. Therefore in the so-called cracker cells an additional heating system is attached to the top to obtain temperatures much higher than the evaporation temperature. Under these conditions the molecules break and an atomic (or composed of smaller molecules) flux is obtained. Commonly used in MBE, although not in the presented work are also radio frequency plasma sources used to produce beams of atomic nitrogen, oxygen or hydrogen.

To determine the beam flux hot-filament ionization gauge is used after stabilization of the cells temperatures. During the measurement the gauge is inserted in front of the substrate holder to measure beam flux corresponding to this arriving to the sample. Atoms of each of the species arrive on the gauge and are ionized and then collected in form of electronic current, which can be expressed as a beam equivalent pressure of the examined species.

The reactor used in the presented work was produced by *Veeco*, model *EPI 930* and it is installed at the Institute of Solid State Physics in Bremen. The system consists of two growth chambers, one for the II-VI materials and one for the III-V, so that the elements of these two groups are not mixed in one chamber. This helps to reduce cross contamination. The chambers are connected by vacuum transfer modules. The II-VI chamber, which was mainly used in the presented work, is equipped with Knudsen evaporation cells containing the following elements: Cd, Mg, Zn, Se, Te and $ZnCl_2$, cracker cells for S and Se and a plasma sources for N_2 and H_2.

To ensure the necessary UHV the system consists of a cryopump and an ion-getter pump. On the inner chamber walls there are shields cooled by liquid nitrogen which provide cryopumping of the system.

2.1.2 *In situ* growth monitoring techniques

To control such parameters as ratio of beam fluxes and the quality of the epitaxial layers the process was controlled by Reflection high-energy electron diffraction. During growth of DBRs and microcavities in-situ reflectivity may be used to control the optical thicknesses of the deposited layers. Both techniques were used in the presented work, hence below I describe both of them.

Reflection high-energy electron diffraction

Reflection high-energy electron diffraction (RHEED) is a powerful tool to monitor such information as crystallization quality, growth mode, surface reconstruction or growth rate. The measurement is possible during crystal growth.

In a RHEED system an electron gun, driven by voltage reaching 30 kV, generates a high-energy beam of electrons, which strikes the sample at a very small angle relative to the sample surface. Incident electrons diffract from atoms at the surface of the sample. The electrons penetrate at a depth of at most few atomic layers and a fraction of the diffracted electrons interfere constructively at specific angles and form regular patterns on the detector. Such diffraction pattern provides information about the surface of the sample.

Ewald construction Ewald's sphere show the allowed diffraction conditions for kinematically scattered electrons in a given RHEED setup. Construction of Ewald's spheres helps to find the crystallographic properties of the sample surface.

The electron diffraction results from its wavefunction being scattered on a regular array of atoms in a crystal. Following the well-know Bragg's law the constructive interference occurs at angle of incidence θ that satisfies the condition

$$2d \sin\theta = n\lambda, \text{ with } n = 1, 2, 3, ..., \tag{2.1}$$

where λ is the wavelength of the incident beam and d is the spacing between two lattice points. It is more convenient to consider the conditions for constructive interference in the reciprocal space. The Bragg condition in the reciprocal space transforms into the Laue-condition (proof of the equivalence of these two conditions can easily be found in textbooks):

$$\vec{K} = \vec{k} - \vec{k}' = \vec{G}, \tag{2.2}$$

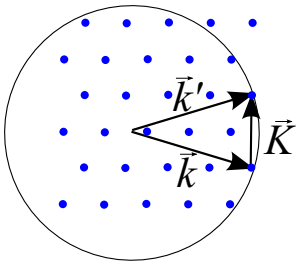

Figure 2.1: The Ewald construction.

where $\vec{G}$ is the reciprocal lattice vector, $\vec{k}$ and $\vec{k}'$ are the wavevectors of the incident and scattered beam, respectively. One can conveniently find the crystal directions satisfying the Laue condition using the Ewald construction, as depicted in Fig. 2.1.

Since the electrons penetrate at a depth of at most few atomic layers, in a RHEED experiment there is no interference in the dimension perpendicular to the sample surface. The reciprocal lattice of a flat surface is a series of infinite rods extending perpendicular to this surface (see Fig. 2.2). Diffraction conditions are satisfied where the rods of reciprocal lattice intersect the Ewald's sphere.

During samples growth RHEED was used to monitor quality of obtained crystals. Atomically rough surfaces, which result from undesired growth of amorphous material, are evidenced by spotty diffraction patterns (instead of streaks, see Fig. 2.2).

Also the optimal ratio of beam fluxes, crucial for obtaining high quality crystals, can be controlled by RHEED. This is because reconstruction of the surface of the crystal, which can be monitored by RHEED, depends on this parameter. For instance in the case of II-VI compounds crystals feature best quality if slightly more atoms of group VI are supplied during the growth process, as they have a higher vapor pressure and lower adhesion coefficient. Element-VI rich growth results in a 2x1 surface reconstruction reflected in specific diffraction pattern. The desired stoichiometric growth can be unambiguously identified by a transformation of the streak patterns from this corresponding to 2x2 surface reconstruction (reflecting group-II-rich or stoichiometric growth) to the 2x1 one.

In-situ reflectivity monitoring

Particularly useful in the growth of DBRs and cavities structures is the in-situ reflectivity of the sample during its growth. This is a powerful, yet relatively uncomplicated method which enables to monitor the optical thickness of the grown material, even if its refractive index is unknown. This is of particular interest in the growth of DBR structures where one (or both) of the used material is a com-

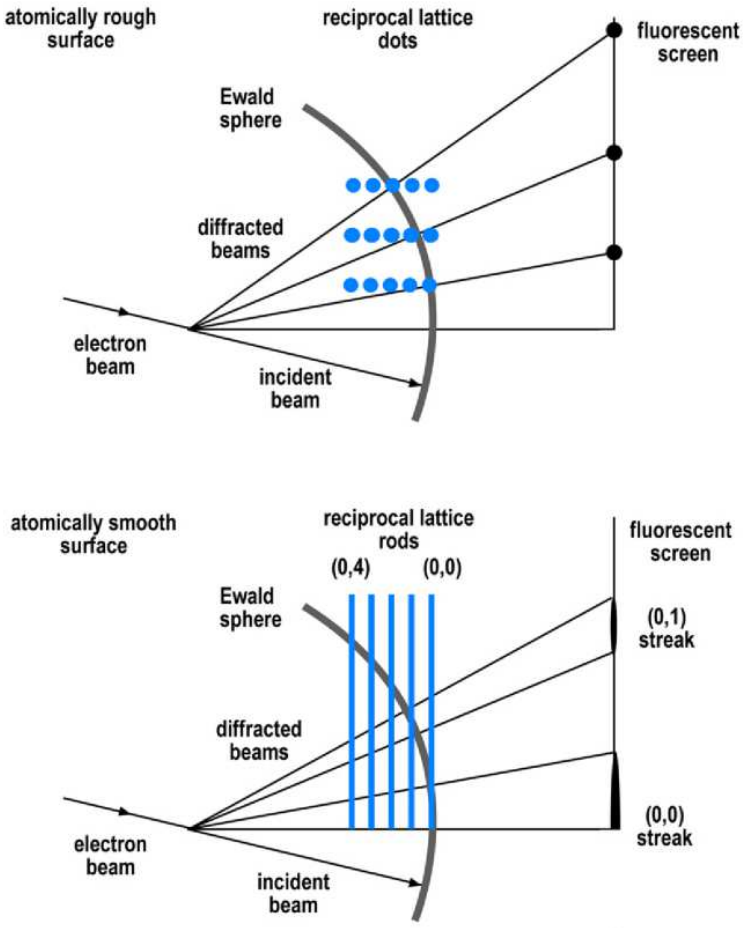

Figure 2.2: Schematic construction of Ewald sphere for atomically rough (upper panel) and smooth (lower panel) surfaces. From [Henini, 2012].

plex multi-compound material (*e. g.* superlattice, ternary compound etc.), where the exact refractive index depends on various parameters like beam fluxes ratio or relative thicknesses etc., which are difficult to control with high precision.

The MBE reactor in Bremen has a window port which ensures optical access to the sample along an axis perpendicular to the sample. A reflectivity system produced by *Filmetrics*, model *F30*, was installed. It consists of a halogen lamp and a Czerny-Turner spectrometer with a 512-element photodiode array for the acquisition of the reflected signal. Sample illumination and reflected light are guided by a multimode fiber attached to the window port of the MBE system. The setup is primarily used to monitor relative reflectivity signal of the sample at a selected wavelength, like i. e. the desired center of the stopband of a DBR. The optimal optical thickness of the grown layers are reflected by a local maximum or minimum in the reflectivity signal, for the high and low refractive index material respectively.

The same setup, unmounted from the MBE reactor, is used for measurements of absolute reflectivity in a configuration where the fiber is attached to a holder ensuring a predefined distance to the investigated sample. Good accuracy can be achieved after calibration of the spectral response of the system with a reference sample with known reflectivity characteristics.

2.2 Post-growth crystal structure analysis techniques

The growth of high-quality complex multi-compound materials (*e. g.* superlattices, ternary compounds *etc.*) requires precise lattice match across the whole epitaxial structure for minimization of dislocation density and strain. Therefore post-growth examination of the epitaxial structures with high-resolution X-ray diffractometry is required. Another examination technique - scanning electron microscopy was used to visualize results of lithographic processing and obtain information about morphology of large pieces of samples and their cross-sections, especially important in the case of hybrid structures described in chapter Micropillars with radial distributed Bragg reflectors. Below, the two techniques are described .

2.2.1 High resolution X-ray diffractometry

This technique was used to determine the lattice parameters of the materials in the grown samples. Its is based on the fact that X-ray wavelengths (approx. 1 to 100 Å) have the same order of magnitude as the spacing between atomic planes in the

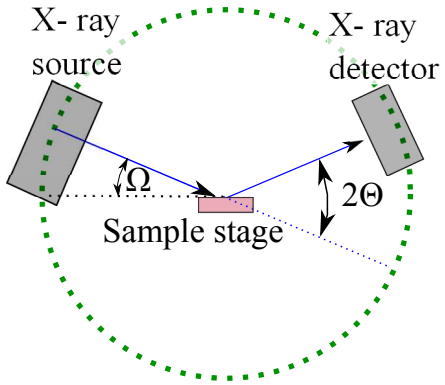

Figure 2.3: Rotation angles of X-ray diffractometer

crystal. Therefore X-rays can be used to produce a diffraction pattern enabling to determine this distance, thus also crystal lattice parameters and strain in the structure.

In the x-ray diffraction (XRD) setup, a sample of investigated crystal is mounted on a goniometer and gradually rotated while being illuminated with X-rays. Obtained diffraction pattern of regularly spaced spots (reflections) is collected by detector. The outcome of a measurement is the diffracted signal intensity as a function of a specific angle. Typically, both sample and detector can be rotated. In Fig. 2.3 the scheme represents typical rotation axes used for scanning the samples.

In a typical experiment, a coupled $\Omega/2\Theta$ scan, the sample is rotated by varying the Ω angle while the detector is varied by 2Θ around one of the reflexes of the sample. A related Ewald construction is presented in Fig. 2.4. Typically, the radiation penetrates the sample several μm deep and therefore all of the epitaxial layers influence the collected interference signal. The intensity of the scattered light depends on the scattering volume, i. e. layers thicknesses, so a rough estimation of those thicknesses can be done from the observed signal. More precise information can be drawn from the high-frequency modulation of the signal (fringes) resulting from the interference on single layers. However, in a multi-layer structure the appropriate assignment of the fringes to a layer is often ambiguous.

The main information that can be drawn from a $\Omega/2\Theta$ scan is the lattice match of the layers, which is of vital importance in the growth of ternary and more complex layers, as the lattice parameter depends on the relative content of the constituting elements. However, one dimensional measurement in the reciprocal space does not provide information on possible strain of the epitaxial layers. Such information can be obtained from a mapping of the reciprocal space around an asymmetric reflex

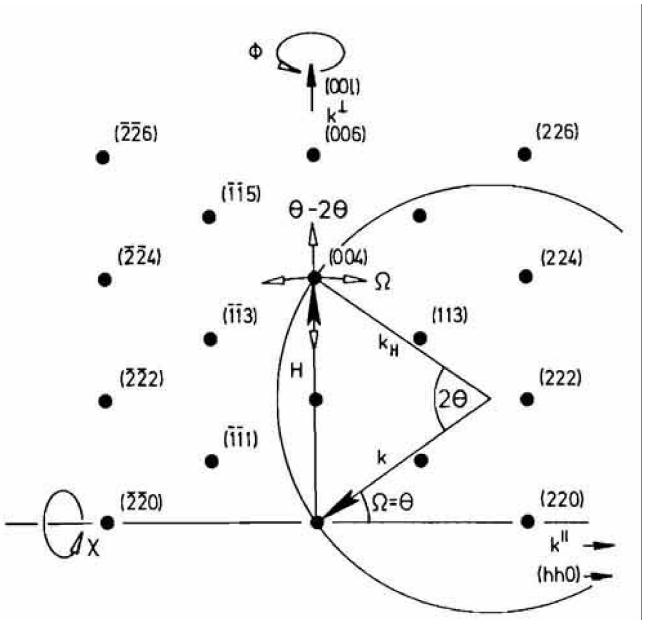

Figure 2.4: Ewald construction of the symmetric GaAs(004) reflection. The Bragg-condition is fulfilled for all the reciprocal lattice points which lie on the Ewald sphere. $k = 2\pi/\lambda$ is the radius of the Ewald sphere; $\mathbf{k}$: incident wavevector, $\mathbf{k}_H$: scattered wavevector, $\mathbf{H}$: reciprocal lattice vector; Ω: incident angle; $\Omega' = 2\Theta$ is the scattering angle. From [Schuster & Herres, 1993]

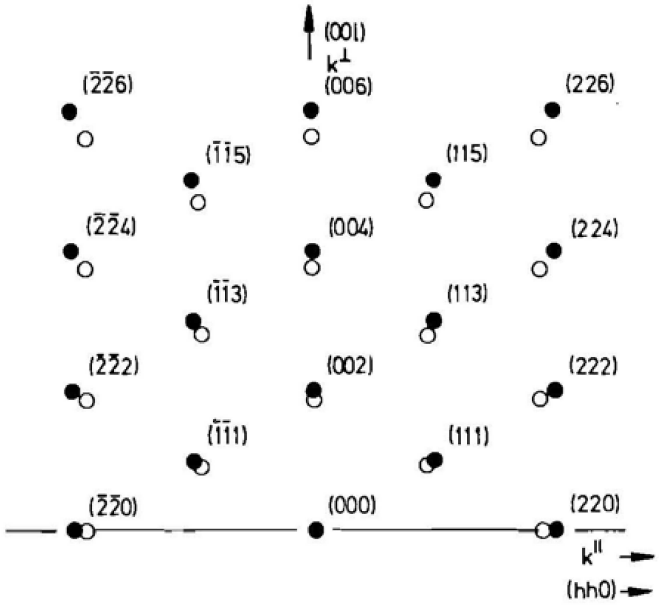

Figure 2.5: Reciprocal space of substrate (filled dots) and fully relaxed layer (empty dots). Substrate orientation (001). From [Schuster & Herres, 1993]

[1] It is obtained by measuring multiple $\Omega/2\Theta$ scans at various Ω directions around one of the asymmetric reciprocal lattice points. This measurement, yielding a two dimensional image of the reciprocal space of the crystal lattice, enables to determine if the deposited layers are relaxed.

2.2.2 Scanning electron microscope

This technique produce image of a sample by scanning its surface with a focused beam of electrons with a nominal resolution down to few nm. In the domain of semiconductor growth it is commonly used for quick and rough examination of the quality of the sample surface and its cross-sections. Comparing with other electron microscopy techniques it has the ability to image a large bulk material. The same type of device was used in both laboratories in Warsaw and Bremen. Both instruments were produced by *FEI*, model *Helios NanoLab DualBeam 600* (Warsaw) and *Nova Nanolab 200* (Bremen).

During investigation the sample is mounted on a piezo-adjusted and motorized holder with 5 axis and a travel range of 150 mm in the X-Y plane. To produce an

[1] Reflex (hkl) is asymmetric if h or k are not equal 0.

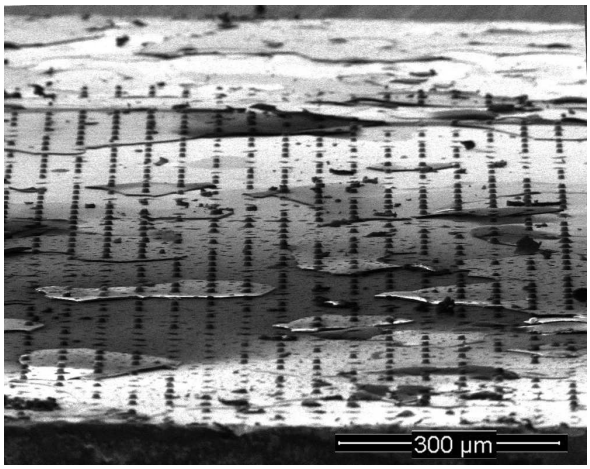

Figure 2.6: SEM image of surface of a planar sample after lithographic etching and deposition of additional layers (sample F). The large deepth of focus enables to investigate large pieces of samples. On the presented image we observe that the deposited additional layers peeled off at most of the sample surface.

image the device delivers an electron beam from a Schottky thermal field emitter. The electron beam is accelerated with a voltage ranging from 350 V to 30 kV and is focused by condenser lens to a spot which size depends on the voltage. For example, the size of the spot is nominally 0.9 nm @ 15 kV and 1.4 nm @ 1 kV (*Helios 600*).

The interaction of the electron beam and the examined material results in the reflection of high-energy electrons by elastic scattering, emission of secondary electrons by inelastic scattering and the emission of electromagnetic radiation. The most commonly used imagining method is based on the detection of secondary electrons.

The electron beam is focused on the sample and moved by deflections coils which deflect the beam in the x and y axes so that it scans in a raster fashion over a rectangular area of the sample surface. Each pixel of the obtained image corresponds to a certain deflection of the scanning beam. The resulting image is a distribution map of the intensity of the signal being emitted from the scanned area of the sample. SEM images have a large depth of field which is due to a low aperture of the beam. This helps in understanding the surface structure of a sample, as can be observed in Fig. 2.6.

The investigated semiconductor samples don't require special preparation for SEM characterization. Non-conductive specimens, like photoresists, tend to become electrically charged when scanned by the electron beam, and especially in secondary electron imaging mode this results in distortions in the observed image, although basic imagining is possible. For such samples, to enhance the image quality it is advised to use low voltage of the SEM operation and to decrease the integration

time lowering thus the charged acquired by the observed area. Such accumulated charge deflects the impinging beam, resulting in artifacts in the obtained images. [1]

2.3 Samples processing techniques

Planar semiconductor microcavities obtained by molecular beam epitaxy ensure photonic confinement only in the vertical direction. To ensure three-dimensional confinement micropillar cavities are processed out of the planar sample. The lateral light confinement is thus assured by the refractive index step, which approximately equals 2 for the ZnTe-air interface, at the investigated wavelengths around 600 nm. To produce such micropillars high aspect ratio etching procedure is required. This procedure has to yield smooth sidewalls of the structures to maintain good optical properties of the structures. High quality micropillars can be obtained by photo or e-beam lithographic processes, where a resist is deposited on the sample and in a subsequent step micropillars are etched by plasma etching. This technique requires relatively long preparations and optimizations of the procedures, but once calibrated one can fabricate tens or even hundreds of micropillars during one process. Micropillar produced by plasma etching techniques include inductively coupled plasma etching [Loffler *et al.*, 2005] and electron cyclotron resonance plasma etching [Reitzenstein *et al.*, 2007]. In a small-scale production a focused ion beam can be used for etching. This technique enables to produce a series of micropillars of any desired diameter without complicated preparation steps. However, the price for this versatility is a comparatively low quality of the sidewalls [Kato *et al.*, 1999] and time needed for the production of a single micropillar. Good availability of the focused ion beam devices both in Warsaw and Bremen determined the choice of technique used in the presented work.

2.3.1 Focused ion beam

Focused ion beam is a technique which enables nanoprocessing of custom shapes in semiconductor samples. In both laboratories (Warsaw and Bremen) FIB is combined with SEM in dual beam devices produced by FEI, model Helios NanoLab DualBeam 600 (Warsaw) and Nova Nanolab 200 (Bremen) (SEM is described in section 2.2.2). The combination of FIB with SEM makes these devices powerful, versatile and easy

[1] To enhance the quality of the micrographs nonconductive samples can be coated with an ultrathin layer of a conductor (*e. g.* platinum, gold) deposited on the sample by low-vacuum sputter coating or by high-vacuum evaporation.

to use as nanoprocessing machines. The systems use a focused beam of gallium ions that are operated at low beam currents for imaging or high beam currents for sputtering or milling. The principles of FIB imaging are similar to SEM, where the major difference is in the source and charge of ions. In FIB it is a liquid-metal ion source of positively charged gallium ions. The beam is focused onto the sample by electrostatic lens and scanned in the X-Y plane. The interaction of impinging gallium atoms with the specimen produces secondary electrons which can serve for imagining, just like in SEM. FIB can deliver ion beam up to tens of nanoamperes on a spot of several tens of nm (the bigger the current the larger is beam divergence and lower resolution). Therefore, in principle, the processed samples should preferentially be conductive to avoid charge accumulation. Nevertheless, in practice even a few micrometers thick photoresists layers can be successfully etched, although with lower resolution as the accumulated charges may deflect the beam. For a conductive sample and at low currents the etching resolution achieve down to 5 nm at acceleration voltage of 30 kV (according to the producer).

FIB milling results in a "dead area"' in the milled specimen which may degrade optical properties of the structured sample. Such a "'dead layer " is a trap for carriers and therefore may induce variable charge environment, i.e. for QDs embedded in micropillars. There were several studies examining such dead layer [Kato *et al.*, 1999; Rubanov & Munroe, 2005]. In III-V systems, if the beam is parallel to the milled material a "dead area" of amorphous layers associated with direct amorphization from the gallium beam is formed [Rubanov & Munroe, 2005]. Redeposition of the milled material, which might be intuitively expected, was not observed [Rubanov & Munroe, 2005]. If the beam is perpendicular to the surface of the milled material gallium atoms are implanted by the beam. Poly-crystalline phases of the etched material may be formed, as the material recrystallizes due to heating from the incident beam. For an acceleration voltage of 30 keV the experimentally measured thickness of the damage layers in III-V semiconductors are around 50 nm in the perpendicular configuration and around 25 nm for the material oriented parallel to the beam [Rubanov & Munroe, 2005]. At 10 keV the damaged layer thickness was roughly half of these values [Rubanov & Munroe, 2005]. The induced variable charge environment from the "dead area", as shown later in this work, had detrimental effect on the stability of emission of QDs embedded in micropillars with small diameter.

2.4 Samples

In this section I describe structural details of the investigated samples. All samples investigated in this work were grown by molecular beam epitaxy (for details on this method please refer to chapter Technology and samples). The core of the study, like the investigation of the Purcell effect (chapter Purcell effect in quantum dot), cavity mode feeding (chapter Purcell effect in quantum dot) and micropillars with radial DBRs Micropillars with radial distributed Bragg reflectors was performed on structures stemming from one planar microcavity sample denoted S1801, which is a particularly successful combination of good quality quantum dots and DBRs, the latter resulting in high quality factor of the microcavity.

All samples presented in this work were grown at the University of Bremen and focused ion beam processing was performed both in Warsaw and in Bremen. A number of complementary samples was grown at the University of Warsaw. The investigations of these samples provided valuable auxiliary information to the study.

The samples were deposited on GaAs substrates and thick (usually 1 μm)ZnTe buffers were grown to reduce misfit dislocations formed at the interface between the substrate and epitaxial layers. Nevertheless, some of these defects propagate for few micrometers through the crystal. One possible solution is to grow buffer layers thicker than 1 μm, however, it significantly extends time required for sample preparation and results in an undesired short-period modulation of the reflectivity of the sample. Another possibility is to use GaSb substrates as they have nearly perfect lattice match to ZnTe. The growth, structural details and investigation of samples based on GaSb substrates (as alternative for GaAs substrates), which are lattice matched to ZnTe is described entirely in chapter Growth of quantum dots and distributed Bragg reflectors on GaSb substrates.

2.4.1 Formation of quantum dots

There are significant similarities in the formation of self-assembled quantum dots in CdSe/ZnSe and CdTe/ZnTe material systems. Despite the fact that the lattice mismatch in these systems is similar as in the III-V systems (i.e. 5.8% for CdTe/ZnTe) QDs do not spontaneously grow in the Stranski-Krastanow mode, as it is the case in III-V systems. This is because the formation energy of misfit dislocations is lower for II-VI materials which is at the origin of plastic strain relaxation before QDs formation transition occurs [Cibert *et al.*, 1990].

Tinjod *et al.* obtained abrupt QDs transition for a strained CdTe layer grown

just below its plastic relaxation critical thickness. They induced QD-formation transition by covering the layer with amorphous tellurium [Tinjod *et al.*, 2003]. This triggers the transition leading to a decrease in the surface energy. This method is now a standard technique for growing CdTe/ZnTe QDs. In both CdTe and CdSe systems the QD-formation transition can also be triggered by a ramp up of substrate temperature [Rabe *et al.*, 1998]. Alternatively, it can also be obtained in a process significantly different from the Stranski-Krastanov growth mode. As described in more detail below, QDs form due to a Zinc-induced reorganization of atoms [Kruse *et al.*, 2007, 2011; Passow *et al.*, 2002].

The microcavities investigated in this work contain two types of QDs, created by the Zn and the Te-induced formation methods. The growth of both kinds of dots begins with deposition of an initial CdTe layer on ZnTe by the migration enhanced epitaxy (i.e. the alternating supply of Cd and Te interrupted by a pause). The thickness of the grown CdTe layer is kept below the critical thickness for plastic island formation. This is monitored by RHEED showing streaky pattern which is characteristic for smooth layers. In the following step during the growth of the Te-induced QDs the sample is cooled down to room temperature and amorphous Te is deposited until the RHEED pattern is completely absent. Next, the sample is heated until complete desorption of the amorphous Te. After this step a spotty pattern is observed which indicates the formation of QDs. In the Zn-induced reorganization the CdTe smooth layer is first surface stabilized under irradiation of Te atoms. In the next step Zn is supplied which results in a site exchange of Zn and Cd atoms leading to a formation of nanoscale Cd-rich areas embedded in Cd-poor material. The exchange process is energy-favorable since this lowers the strain induced by the CdTe layer on ZnTe [Kruse *et al.*, 2011]. In a final step, for both kinds of QDs, the CdTe QDs are capped by ZnTe grown by migration enhanced epitaxy to achieve good crystalline quality of the ZnTe material around QDs.

The quantum dots obtained in the Te-induced process are lens-shaped, have a lateral size of about 10-20 nm and about 2 nm along the growth axis. The density of the quantum dots is of the order of $10^9\,\mathrm{cm}^{-2}$ [Wojnar *et al.*, 2008].

The structural properties of Zn-induced QDs were investigated with transmission electron microscopy. Exemplary results are presented in Fig. 2.7. Strain state analysis (SSA) , i.e. the evaluation of lattice distortion in the (Zn,Cd)Te area of the specimen taking the ZnTe lattice constant as a reference, revealed that elliptically shaped localizations reaching a Cd concentration of up to 65 % were obtained. The height of these QDs is about 2-3 nm and the lateral size in the range of 4-9 nm,

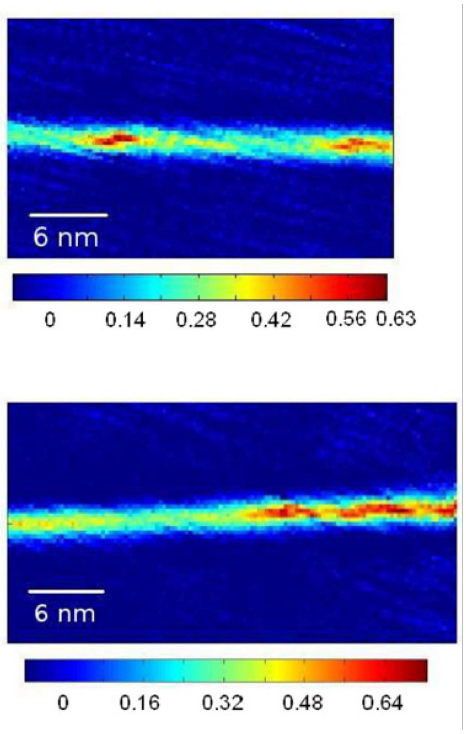

Figure 2.7: Cd concentration maps for Zn-induced QDs. Maps are derived from strain state analysis (SSA - see text). The graphs show two different areas of the QD sheet. From [Kruse *et al.*, 2011]

while the density of the quantum dots is of the order of $10^{11}\,\mathrm{cm}^{-2}$ [Kruse *et al.*, 2011].

2.4.2 Structural details of the distributed Bragg reflectors

A distributed Bragg reflector is formed from multiple layers of alternating materials with varying refractive index, where each layer boundary causes a partial reflection resulting in constructive interference of a selected range of wavelengths constituting the stopband of a reflector. The width of the stopband depends on the contrast of the refractive indices, while the absolute value of reflectivity depends on both the contrast and number of pairs.

In principle a DBR can be made of any transparent materials. However, in microcavities containing QDs the efficiency of those QDs depends on the crystal quality of the embedding layers. This requirement is well fulfilled in homoepitaxial structures combining DBRs, cavity and active material in one bulk crystal. This approach results in the highest quality of optoelectronic devices. One of the greatest challenges in designing and growth of semiconductor vertical optical resonators is to produce materials with the same lattice parameter and possibly largest refractive index contrast.

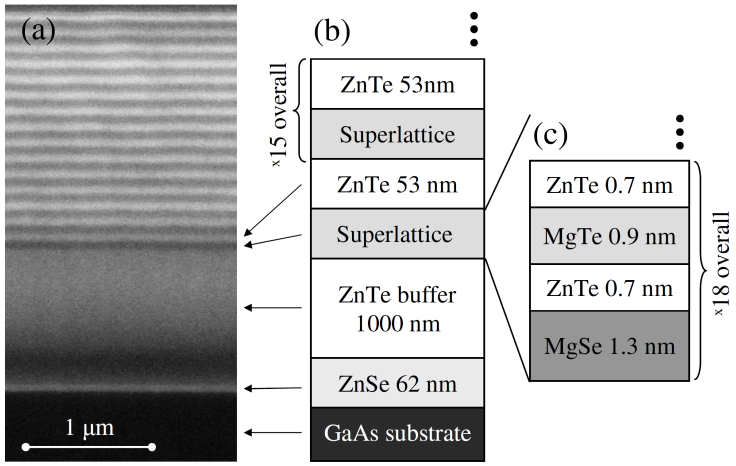

Figure 2.8: Structure of distributed Bragg reflector lattice matched to ZnTe buffer. (a)Cross-section image obtained with scanning electron microscope. (b) Scheme of layers. Material with high refractive index is ZnTe. Material with low refractive index is a short period triple SL MgSe/ZnTe/MgTe/ZnTe shown in (c). Layer thicknesses in (b) were determined from interference effects observed using *in situ* and post-growth reflectivity. Layer thicknesses in (c) were estimated using growth rates and period of SL 3.6 nm known from x-ray diffraction. From [Pacuski *et al.*, 2009]

In this thesis I investigated samples based on, recently developed, superlattice-based distributed Bragg reflector (DBR) [Pacuski *et al.*, 2009] lattice-matched to ZnTe [Kruse *et al.*, 2011]. This DBR contains ZnTe layers as the high-refractive index material and a short-period superlattice consisting of MgSe, MgTe and ZnTe layers as the low-index material. The lattice parameter of MgSe is smaller than ZnTe and MgTe has lattice parameter larger than ZnTe (see Fig. 1.6). Therefore the lattice mismatch of ZnTe and superlattice is compensated by using a defined thickness ratio of MgSe and MgTe layers. This is much easier than balancing the strain by controlling the content of a ternary or quaternary compound, as it was done in previously reported approaches [Nomura *et al.*, 2004; Ueta & Hommel, 2002]. MgSe and MgTe layers are separated by very thin ZnTe layers, which are neutral with regard to strain and lattice parameter, but they stabilize the growth in Zinc-blende structure. Details of the structure are presented in Fig. 2.8.

The superlattice can be treated as a homogeneous layer with a single dispersion. The DBR layers have a relatively large refractive index step of $\Delta n = 0.48$ ($n_{ZnTe} = 3.08$ [Marple, 1964], $n_{SL} = 2.6$ [Pacuski *et al.*, 2009] at the photon energy

of 2050 meV) which allows for the use of an efficient top DBR with a small total thickness resulting in a relatively low level of absorption of the excitation laser beam.

2.4.3 Growth of microvavity containing quantum dots

The details of the description presented below refer to sample S1801 grown by W. Pacuski and C. Kruse at the University of Bremen, however to a large extent the presented procedure is universal and I used it during the growth of DBRs and microcavities on GaSb substrates (see chapter Growth of quantum dots and distributed Bragg reflectors on GaSb substrates). As was already mentioned before, S1801 and microstuctures etched on this sample were the principle structures investigated in this work.

In microcavity S1801, the maximum of the QDs emission intensity was designed at around 2110 meV, while the cavity thickness, which defines the planar cavity mode energy, was targeted at 2050 meV. This corresponds to the low energy tail of the QDs ensemble emission. This choice enabled later observation of coupling of a single QD line with a single cavity mode without background of other emission lines in spectra.

The growth of microcavity structure was performed by molecular beam epitaxy (MBE) on a GaAs(100) substrate kept at a temperature of 360 °C. In the first step the GaAs substrate was covered by a thin ZnSe layer. This is an experimentally established procedure which results in facilitating the epitaxial growth of ZnTe on GaAs. The ZnSe was followed by a thick ZnTe buffer (1 µm) to relax the strain induced by the substrate and obtain good crystal quality for the growth of the DBR. According to high resolution x-ray diffraction (HRXRD-not shown) top epitaxial layers of ZnTe of such buffer are fully relaxed and therefore can be used as a quasi-substrate for the structure that follows.

For the resonator structure a 20-pair lower DBR and a 18-pair upper DBR are employed providing a high level of photon confinement within the microcavity. The slight asymmetry favors emission in the upper direction where the detectors are located in standard experimental configuration. The two DBRs consist of 53 nm thick ZnTe layers as the high refractive index material and 20-period MgSe(1.3 nm)/ZnTe(0.7 nm)/MgTe(0.9 nm)/ZnTe(0.7 nm) superlattices for the low-index layers. The quarterwave thickness values of the DBR layers have been chosen carefully in order to match the targeted 2050 meV energy of the center of the DBR stopband and cavity mode. The optimal layer thickness was additionally controlled by *in situ*

Table 2.1: *Parameters for etching micropillar cavities using FIB. The final current is optimized for balancing low damage to the micropillars sidewalls and keep this phase short enough so that sample holder drift does not play a role. The parameters diameters are optimized for balancing affordable total etching time and high quality factor of the resonators.*

	Ion beam current	**Inner/outer diameter (μ)**			
step 1	**3 nA**	5/15.0	8/15.0	8.0/15	8.0/15
step 2	**0.5 nA**	1.5/6.5	3/9.0	3/9.0	6/9.0
step 3	**30 pA**	1.2/2.0	1.6/2.1	2.0/3.2	5/6.5
step 4	**9 pA**	1.0/1.6	1.4/1.7		
	Final diameter (μ):	1	1.4	2	5

reflectivity.

The cavity region sandwiched between the two DBRs is made of ZnTe and the central part of the sample has an optical thickness of λ . For additional degree of freedom in terms of tuning of QDs emission to cavity mode the microcavity layer features a gradient of thickness. This was obtained by pausing the rotation of substrate during the growth of this layer. Since the flux of atoms is not uniform this result in a gradient of sample thickness.

2.4.4 Etching of micropillars

A series of cylindrically shaped micropillars with various diameters between 0.7 and 5 μm were prepared from the planar microcavity structure by focused ion beam (FIB) etching. The Gallium ions beam was accelerated with a voltage of 30 kV . Currents between 50 pA and 5 nA have been applied to remove the II-VI material around the micropillars entirely, i.e. in a radius of 10 μm around each micropillar only the GaAs substrate is remaining.

The exact beam currents as well as the inner and outer diameter of the etched ring, which were used during the etching are summarized in table 2.1. The yield of this procedure is roughly one micropillar per hour. It can be automatized to some extent, although user control is required for most of the time of the procedure.

2.4.5 List of samples

Table 2.2 presents full list of samples investigated in the presented work. In further chapters I refer to samples A,B,C *etc.*, where the details on each of these samples can be found in the table.

Table 2.2: List of samples

Designation	Sample number	Description	Piece label	Grower	Processing	substrate	Active material	details I	details II
A	S1695	DBR		Pacuski, Kruse		GaAs		15 DBR pairs	
B	S1723	empty microcavity						13 DBR upper pairs, 15 DBR lower pairs	
C	S1761	microcavity, micropillars		Pacuski, Kruse	T. Rohbeck	GaAs	CdTE QDs (Zn induced?)	20 DBR upper pairs, 18 DBR lower pairs	
D	S1763					IFPAN CdTe QDs		5 DBR upper pairs, 15 DBR lower pairs	
E	S1801	microcavity, micropillars	AIIcLE	Pacuski, Kruse	Jakubczyk, Franke		CdTe QDs	20 DBR upper pairs, 18 DBR lower pairs	radial DBR
F	S1801	microcavity, micropillars	DIIILE	Pacuski, Kruse	Jakubczyk, Franke		CdTe QDs	20 DBR upper pairs, 18 DBR lower pairs	radial DBR
G	S1801	microcavity, micropillars	AI	Pacuski, Kruse	Jakubczyk		CdTe QDs	20 DBR upper pairs, 18 DBR lower pairs	
H	S1804	QDs		Pacuski, Kruse		CdTe quantum dots			Single Mn
I	S1806	reference, same QDs as in S1801							
L	S1911	QDs		Jakubczyk, Kruse		GaAs	CdTe QDs	30 MEE loops CdTe	
M	S1912	QDs		Jakubczyk, Kruse		GaAs	CdTe QDs	20 MEE loops CdTe	
N	S1915	QDs		Jakubczyk, Kruse		GaSb 1 min HCl etch	CdTe QDs	20 MEE loops CdTe	
O	S1916	QDs		Jakubczyk, Kruse		GaSb 0 min HCl etch	CdTe QDs	20 MEE loops CdTe	
P	S1917	QDs		Jakubczyk, Kruse		GaSb 2 min HCl etch		20 MEE loops CdTe	
X	S1983	QDs		Jakubczyk, Kruse		GaSb 1 min HCl etch			
Y	S1984	QW		Jakubczyk, Kruse		GaSb 1 min HCl etch			
Z	S1995	QDs		Jakubczyk, Kruse		GaSb 1 min HCl etch			
A1	S1996	QWs		Jakubczyk, Kruse		GaSb 1 min HCl etch			
B1	UW0156	QDs Microcavity		Rousset, Pacuski	Jakubczyk, Rousset				Single Mn
C1	S2066	QDs		Jakubczyk, Kruse		GaSb 1 min HCl etch	CdTe QDs	30 MEE loops CdTe	MEE cap
D1	S2067	QW		Jakubczyk, Kruse		GaSb 1 min HCl etch		15 MEE loops CdTe	MBE cap
E1	S2069	QW		Jakubczyk, Kruse		GaSb 1 min HCl etch			
F1	S2077	QW		Jakubczyk, Kruse		GaSb 1 min HCl etch			
G1	S2078	DBR		Jakubczyk, Kruse		GaSb 1 min HCl etch		DBR 15 pairs	
H1	S2081	DBR		Jakubczyk, Kruse		GaSb 1 min HCl etch		DBR 12 pairs	
I1	S2082	VCSEL		Jakubczyk, Kruse		GaSb 1 min HCl etch		20 DBR upper pairs, 7 DBR lower pairs	
J1	S2083	VCSEL		Jakubczyk, Kruse		GaSb 1 min HCl etch		20 DBR upper pairs, 7 DBR lower pairs	

Chapter 3

Spectroscopic setups

Spectroscopy measurements constitute the main experimental approach used in this work. The specific arrangements were designed for measurements of reflectivity, photoluminescence and microphotoluminescence, also time and angle-resolved. All these experiments were performed at temperature range from 1.4 to 300 K. The used cryostats allow direct optical access to the sample through optically non-active windows made of fused silica. Therefore setups can be based on free beam optics. The laser and other optional sample illumination (i. e. white light for reflectivity measurements) are directed onto a beam splitter (usually dichroic mirror or glass plate) located at the main optical axis defined by the cryostat geometry. The light emitted from or reflected by the sample follows the same axis. A generic setup is presented in Fig. 3.1.

For reflectivity measurements a halogen lamp is used as a source of light providing a broad continuous spectrum.

The majority of experiments described in this work focus on optical investigations of micropillars. The microphotoluminescence experimental technique is best suited for those experiments as it assures both high collection efficiency and the possibility to select the desired microstructure. In a microphotoluminescence experimental setup the light is focused on the sample by a microscope lens. The resulting luminescence is collected by the same lens and follows the same path as the exciation beam until a selective beam splitter, like, for example, interference filter.

In experiments requiring low temperatures (< 100 K) two types of optical cryostats were used in this work. Measurements below 4.2 K were performed uniquely in an immersion cryostat. At temperatures above 4.2 K also a gas flow cryostat was used (see Fig. 3.2).

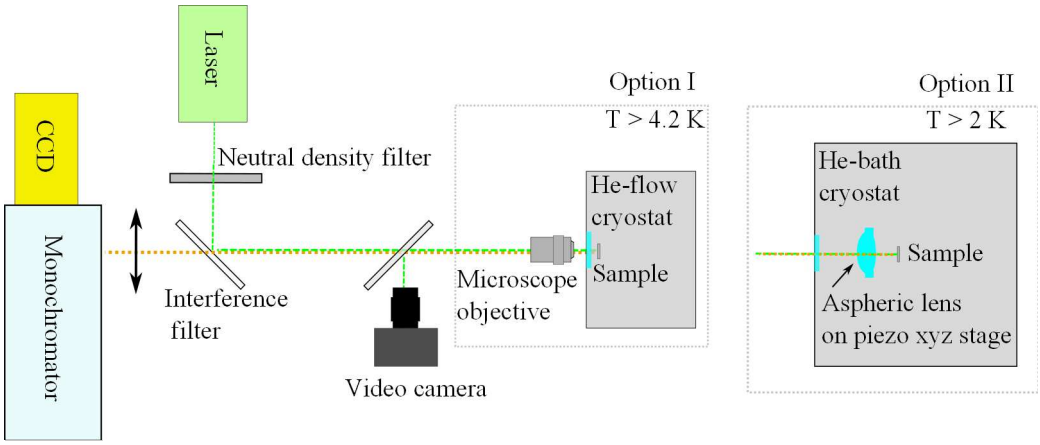

Figure 3.1: Experimental setup for PL measurements.

In all the setups the temperature was measured using calibrated *Cernox* sensors placed in the vicinity of the sample.

The excitation beam was delivered from a frequency-doubled YAG laser (532 nm), laser diode emitting at 405 nm or Argon laser operating at 488 nm. Such wavelengths are spectrally outside stopbands of the investigated DBRs.

Flow cryostat In a flow cryostat the sample is kept in vacuum, fixed to the sample holder usually with silver paste which assures good thermal contact. This holder is cooled by helium flow, the flow rate determining its temperature. For microphotoluminescence experiments a microscope lens is used. It is located outside the cryostat and therefore long working distance (at least 2 mm) is required for reaching the sample in the cryostat. In the presented work one lens was particularly often used as it features excellent parameters. It was produced by Nikon, model MUE30900. This lens has 100x magnification and long working distance, equaling 6.50 mm. It also features high resolution and high angular collection efficiency - both provided by a high numerical aperture 0.7. Due to a large numerical aperture the physical depth of focus is only 0.56 µm which requires precise adjustment of the objective lens over the sample along the z axis, that is the focal length. The resolution achieved with the lens was close to the diffraction limit and enabled achieving spot sizes down to 0.5 µm which is a crucial characteristic of the setup for observing single QDs in planar microcavities or in precise micropillars excitation.

For precise positioning of the light spot on the sample the cryostat is placed on a precise X-Y positioning table with micrometric screws. Additionally, the microscope

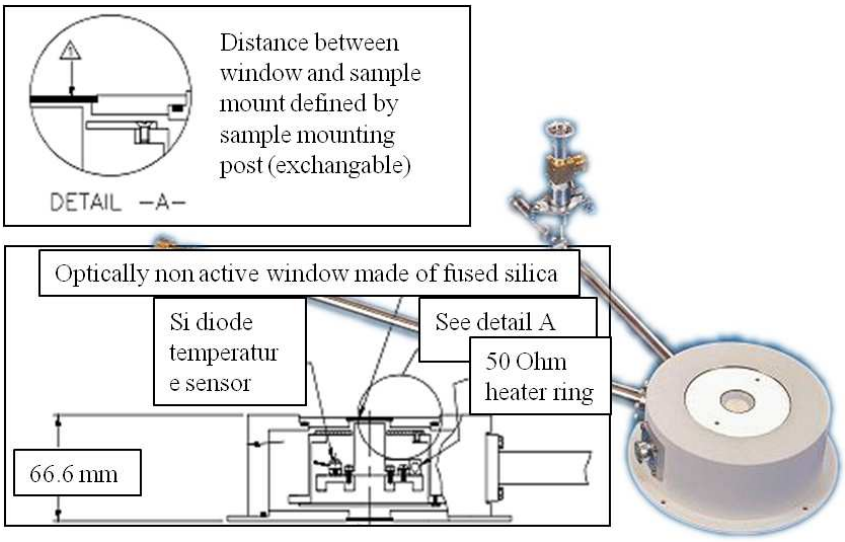

Figure 3.2: Type of the gas flow cryostat used in the experiments. Picture and scheme adapted on materials from *www.janis.com/products* .

objective is attached to a piezoelectric positioner allowing for final adjustment of the position of the spot with resolution down to single nanometers.

Immersion cryostat In an immersion cryostat the sample is immersed in liquid, gas or superfluid Helium (the latter has temperature below 2.17 K) with temperature controlled by control of Helium pressure (liquid and superfluid) or by controlling gas helium temperature with a heater.

In microphotoluminescence experiments performed in the immersion cryostat light was focused by an an aspheric lens on a piezoelectric stage which was immersed together with the sample in liquid or gaseous helium. The high numerical aperture of the lens (0.68) enables collection of photons emitted at an angle of up to 43 degrees with respect to the direction perpendicular to the sample. The achievable resolution of the aspheric lens was significantly lower than the diffraction limit. It was around 1 μm, which might be due to stress induced by its holder (temperature expandability of the titanium holder and glass are different). Such aspheric lens is highly chromatic so the distance between the lens and sample has to be compromised between the focal length of the excitation beam and the higher focal length for the emitted light (of wavelength longer than the excitation beam). The light emitted by the investigated samples is collected by the lens and a parallel beam is formed. The beam is then focused on a monochromator slit, dispersed on a grating in monochromator and

finally detected with a charge coupled device (CCD) camera. The CCD camera allows for collection of time-integrated spectra of the investigated samples.

For precise positioning of the light spot on the sample piezo-electric actuators provided by *attocube systems* are used. It allows x-y-z movement of an aspheric lens and focusing on a chosen spot of the sample.

3.1 Setup for time resolved measurements

For time resolved photoluminescence collection the excitation laser pulses were delivered from a femtosecond laser (*Coherent Mira Seed*), which emits laser pulses about 60 fs long. The frequency of pulses was doubled (the resulting wavelength was around 400 nm) which resulted in pulses around 100 fs long (measured in an laser autocorellation experiment [Kazimierczuk, 2013]). The repetition time of the laser was equal around 13.2 ns.

In a time-resolved photoluminescence experiment the intensity of the signal is collected together with the information about the delay of photon arrival with respect to the laser excitation pulse. The expected short lifetime of QD exciton in cavity, which is of the order of several tens of ps, combined with relatively low intensity of the usually investigated signal from samples, pose stringent requirements on the detectors efficiency and time resolution. In the experiments where micropillar cavities were investigated a Hamamatsu streak camera working in the synchro-scan mode was used. Previous to these experiments were experiments on QDs in bulk semiconductor, where avalanche photodiodes supplied by *idQuantique* were used (streak camera was not available at this time). The time-resolution of the diodes is around 50 ps, while the streak camera has variable resolution depending on the length of the investigated time window. Best, nominally achievable streak camera resolution is 2 ps, although a value of 5.8 ps was found for the used experimental setup in an experiment where the second harmonic of the femto-second laser impulse length was investigated [Kazimierczuk, 2013].

In experiments with avalanche photodiode this diode was connected to a time-resolved photon counter. It enabled recording of temporal profiles of the photoluminescence at specific energy. The correlation module provided by *PicoQuant* (model *Hydra Harp*) was connected with an avalanche photodiode and pulsed laser synchronization (see Fig. 3.3). A histogram of photoluminescence photon counts versus time difference between the laser pulse and photon emission of a desired energy was measured yielding the decay time of light emission from QDs.

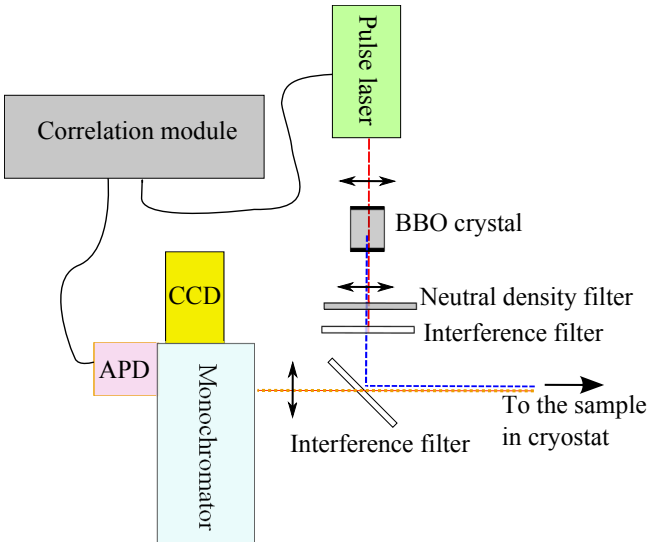

Figure 3.3: Scheme of the experimental setup for measurements of PL decay time.

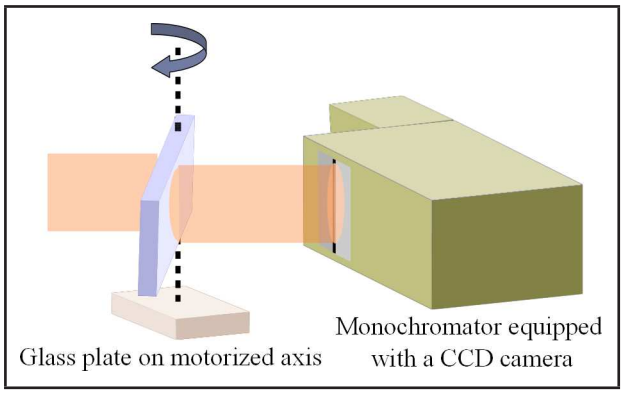

Figure 3.4: Scheme of the setup used to deflect the beam.

3.2 Setup for mode-mapping and angle-resolved measurements

The spectroscopic setup with aspheric lens (see Fig. 3.1) was used to investigate the distribution of the electromagnetic field inside the pillars. The lens in front of the monochromator was removed, and pillar top surface was imaged on the slit with the single aspheric lens left in the setup. The slit cut a vertical cross-section out of the image, which was dispersed horizontally by the spectrometer (see Fig. 4.11). By deflection of the beam with a thick glass plate (see Fig. 3.4) and consecutive collection of one-dimensional, energy-resolved cross-sections of the emission, a set of two-dimensional emission patterns is obtained for various emission energies.

The angular distribution of emission from planar cavity was investigated in the standard microphotoluminescence setup adapted to perform Fourier plane imagin-

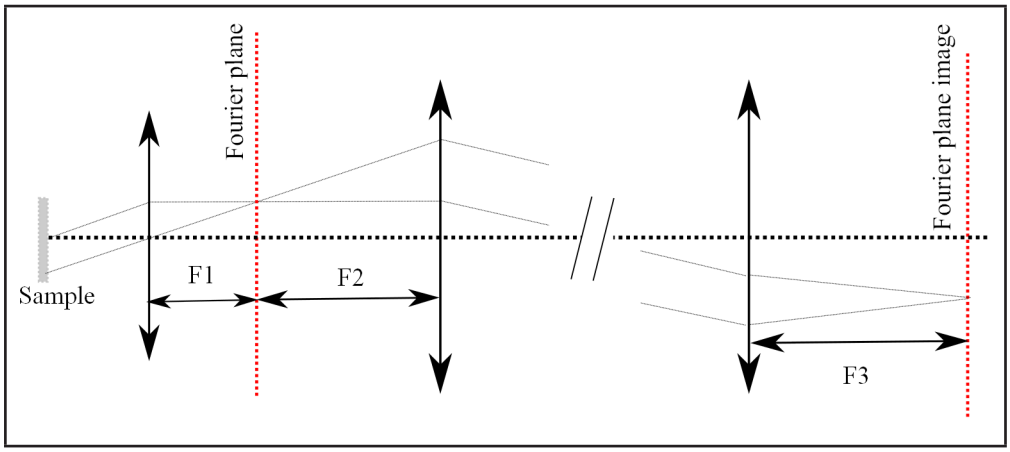

Figure 3.5: Scheme of Fourier plane imaging setup.

ing, as presented in Fig. 3.5.

Chapter 4

Basic optical properties of planar and micropillar cavities

In this chapter I discuss the basic optical characterization of the microcavities. First, I focus on the energies of the cavity modes and compare the results to simulations. I analyze quality factor of the microcavities. In the next section I describe light emission from these microcavities. The angular distribution of emission from planar microcavity is presented as well as spatial profile of distribution of the electromagnetic field in micropillars. A pronounced modification of the isotropic radiation of the QDs is shown experimentally for such structures and compared to simulations. The diffraction observed is found to be inherent for experiments with large numerical aperture of the lens and small diameters of the investigated micropillars.

4.1 Photoluminescence and reflectivity of a planar microcavity

I start by analyzing the photoluminescence of a planar microcavity containing QDs (sample D). A basic, but yet conclusive experiment consist of measurement of the microluminescence and reflectivity spectra. Results are shown in Fig. 4.1. We observe a dip in the reflectivity related to the resonant wavelength of light that is being transmitted through or absorbed in the microcavity region of the sample [1]. This feature of such Fabry-Perot resonator has a great effect also on the shape of the luminescence of QDs located in the center of the cavity. The observed luminescence

[1] the transmitted light is later absorbed in the substrate

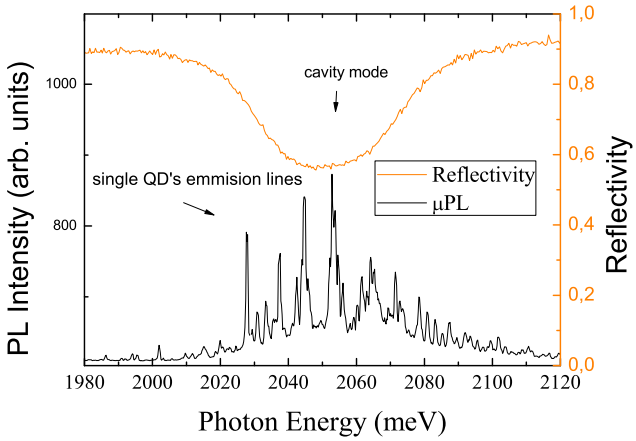

Figure 4.1: Reflectivity and microphotoluminescence of a planar microcavity containing QDs (sample D) spectra revealing enhancement of the emission of QDs in the cavity mode.

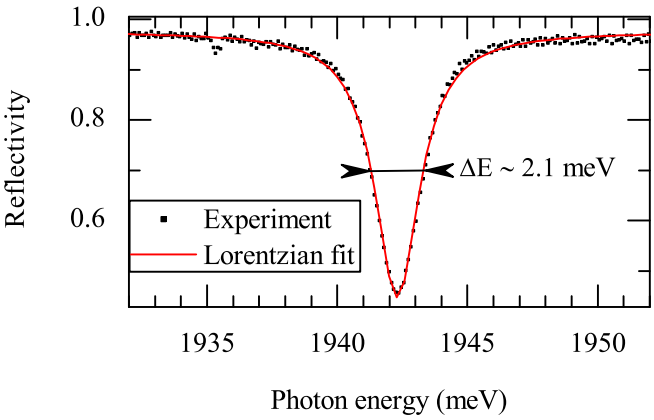

Figure 4.2: Reflectivity spectrum of a microcavity (sample B), collected with high-spectral resolution, revealing a quality factor $\approx$ 930. A Lorentz function fit yields the FWHM of the mode dip.

shape coincides with the shape of the mode deduced from the reflectivity experiment. We observe mainly the luminescence of QDs emitted within the eigenenergy of the resonator. This clearly indicates that the emission of CdTe QDs is influenced by their photonic environment. The observed effect can be explained by damping of the vertical emission of QDs which is off-resonance from the cavity mode. The width of the observed luminescence / reflectivity dip is related both to the quality factor of the resonator (for details see section 4.1.1) and the angular range of the detected photons, as discussed in section 4.4.

4.1.1 Quality factor of planar microcavity

During the development of microcavities after each growth we routinely analyzed their reflectivity spectra to assess their potential to influence the emission of CdTe quantum dots. As described in the previous section the photonic 2D confinement in planar microcavities can be conveniently characterized by reflectivity measurements yielding the resonance energy. To characterize the quality factor the collection angle of the photoluminescence has to be preferentially low. This is because optical microcavities feature angular emission of higher energy than the fundamental mode (such angular emission is characterized in section 4.4). The resulting spectral broadening of the observed mode blurs the investigated quality factor of the cavity given by the ratio $E/\Delta E$ (energy of the mode over its energy full width at half maximum). We performed macro reflectivity measurements in the standard photoluminescence experimental setup (see chapter Spectroscopic setups) where we replaced the microscope lens with a lens featuring long focal length 150 mm. On the path of the parallel beam we additionally placed an aperture. Such approach enabled us to control the photon collection angle.

Reflectivity spectrum of sample B presented in Fig. 4.2 reveals a cavity mode around 1942 meV for normal light incidence. The mode width is equal to about 2.1 meV, which results in a quality factor $Q \approx 930$. In the presented result the Lorentz function fits evenly to the experimental data. Hence, we can estimate that we do not see broadening due to the collection of photons emitted off the z-axis. However, the observed Q value is influenced by the lateral inhomogeneity of the structure. The sample was not rotated during the cavity growth in order to obtain a gradient in the cavity thickness (for more details see chapter Technology and samples). The mode energy shifts by 2 meV per 1 mm displacement on the sample [Jakubczyk, 2009]. Finite size of the light spot (several hundreds of microns) results in a broadening of the cavity mode. The light spot size has approximately a diameter of 0.4 mm which results in thickening of the observed FWHM of the investigated cavity mode by around 20% .

The obtained quality factor, corrected for the broadening due to the cavity non-homogeneous width, equals around 1000. If micropillar cavities were etched out of this sample only very moderate Purcell enhancement could be expected (for details on Purcell factor evaluation see chapter Purcell effect in quantum dot).

There are several factors influencing the quality factor of a planar microcavity. The structural deviations from the designed optimal thicknesses of the layers are

determined by the precision of the epitaxial method used. In the case of MBE this precision is of the order of single atomic layers, which is far less than the wavelenght in the material. Therefore, structural disorder has a negligible effect on the quality factor of our resonator strucutures. If absorption is neglected Q increases with the increase of number of Bragg pairs. However, in real structures the probability for a photon to be absorbed in the Bragg mirror before leaving the structure increases with the thickness of such mirror, and therefore Q-factor reaches its maximum value for a certain number of such pairs. To optimize the quality factor of structures the growers (Wojciech Pacuski and coworkers from Bremen) performed simulations using the transfer matrix method varying the number of upper and lower Bragg pairs. They determined an optimal value of 18 upper and 20 lower Bragg pairs for the investigated ZnTe-based system. The slight asymmetry in the number of pairs, although not optimal for the Q-factor, results from the desired guiding of the emission in the upper direction (*i. e.* toward detector).

4.2 Photonic modes

4.2.1 Identification

In the previous section we observed luminescence of QDs within a cavity mode of a planar microcavity. In that experiment the cavity mode spectral position could be unambiguously identified due to its broad spectral characteristics which could not be mistaken with QD emission. However, if the cavity mode emission has a comparable linewidth (within the experimental accuracy) as single QDs emission lines, as is often the case for high Q-factor cavities, then an additional experimental technique has to be established for routine mode identification required in further experiments. It is of special importance in the case of micropillar cavities. Reflectivity measurements of micropillar cavities, although feasible, are not as straight-forward as those of planar microcavity as they require greater sensitivity of the setup to detect the relatively smaller signal. Additionally, the radial confinement in micropillars results in discretization of the radial and azimuthal component of the field. This yields a set of photonic modes distributed over a certain spectral range, where they are observed together with QDs emission lines.

Since our further investigations are based on photoluminescence, we routinely used this technique to identify energy position of cavity modes. To distinguish the emission which can be directly related to QD emission from that of cavity modes

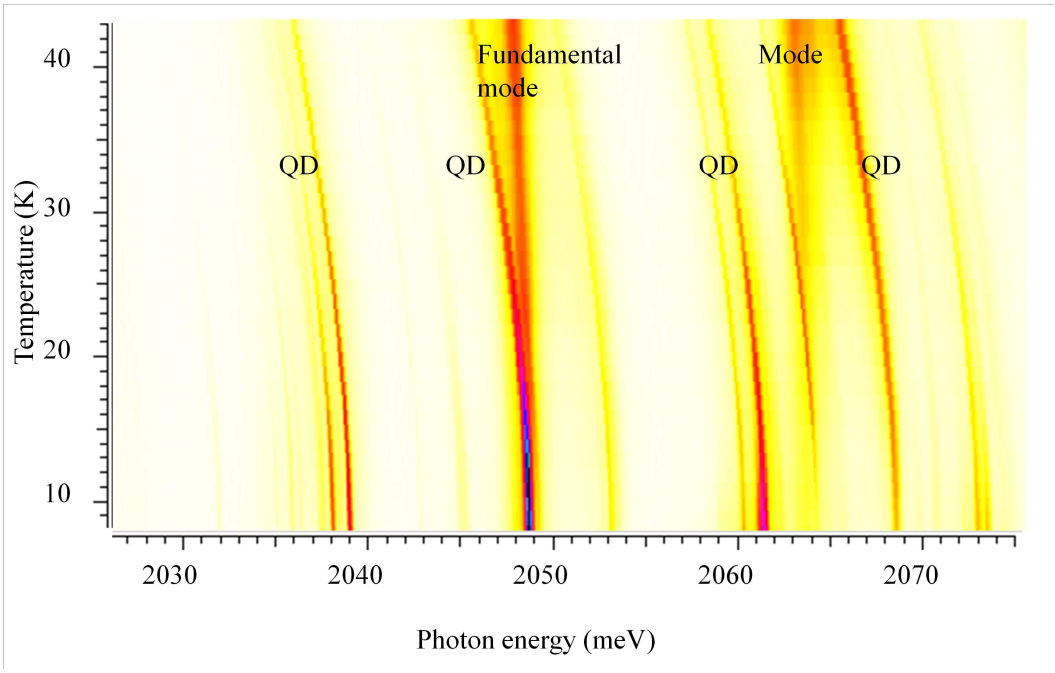

Figure 4.3: Photoluminescence energy vs temperature (in false color scale) of a micropillar with QDs (Sample E, micropillar B). The lines are identified according to their dependance on the temperature - QDs lines depend more strongly on the temperature than cavity mode. Fundamental mode is identified as the mode with the lowest energy.

we use the fact that the excitonic transition energy depends more strongly on the temperature than the energy of the photonic mode with temperature. The temperature dependence of the energy of the cavity mode originates from the change in the refractive index of the cavity material (ZnTe) with temperature, which is usually a small correction. The temperature variation of energy of QDs transitions is related to the bandgaps of CdTe and ZnTe. This property of the QD-cavity system allows us to identify features observed in the luminescence spectra, as shown in Fig. 4.3. It has to be noted here that cavity modes can also be observed in photoluminescence spectra even if no QD transition line coincides with the spectral position of the mode (for the discussion of the origin of cavity mode emission see chapter Purcell effect in quantum dot).

4.2.2 Energy of modes

In the micropillar cavities containing QDs the μPL spectra measured at low temperature and under low excitation power (few μW) show both single QD lines and cavity modes. If the spectral density of QDs is high enough at increased temperature the phonon-broadened spectral emission of each QD merges into a continuum of QDs emission and serves as an internal light source in the investigation of cavity photonic properties [Gérard *et al.*, 1996]. Moreover, at high excitation density higher QDs orbitals start to be occupied which leads to a qusicontinuum of states and transitions feeding mode emission [Laucht *et al.*, 2011]. Thus, at increased excitation power and temperatures of the order of several tens of kelvins a characteristic pattern, dependent on micropillar size, appears revealing photonic modes due to the 0D photonic confinement, as shown in Fig. 4.4. The spectrum measured at 65 K presents well-separated modes of the micropillar. A series of micropillars with various diameter was measured. The modes form a characteristic pattern as shown in Fig. 4.5. With decreasing diameter of the micropillar a blue-shift of the pattern is observed, as well as an increase of the distance in between neighboring mode lines. This is expected for increasing confinement and routinely observed for micropillar cavities in other material systems [Gérard *et al.*, 1996; Lohmeyer *et al.*, 2006b]. Despite the random distribution of QDs and their emission energies the photonic pattern is reproducible for series of micropillars of the same size and it undergoes smooth changes for increasing/decreasing diameter of the micropillars.

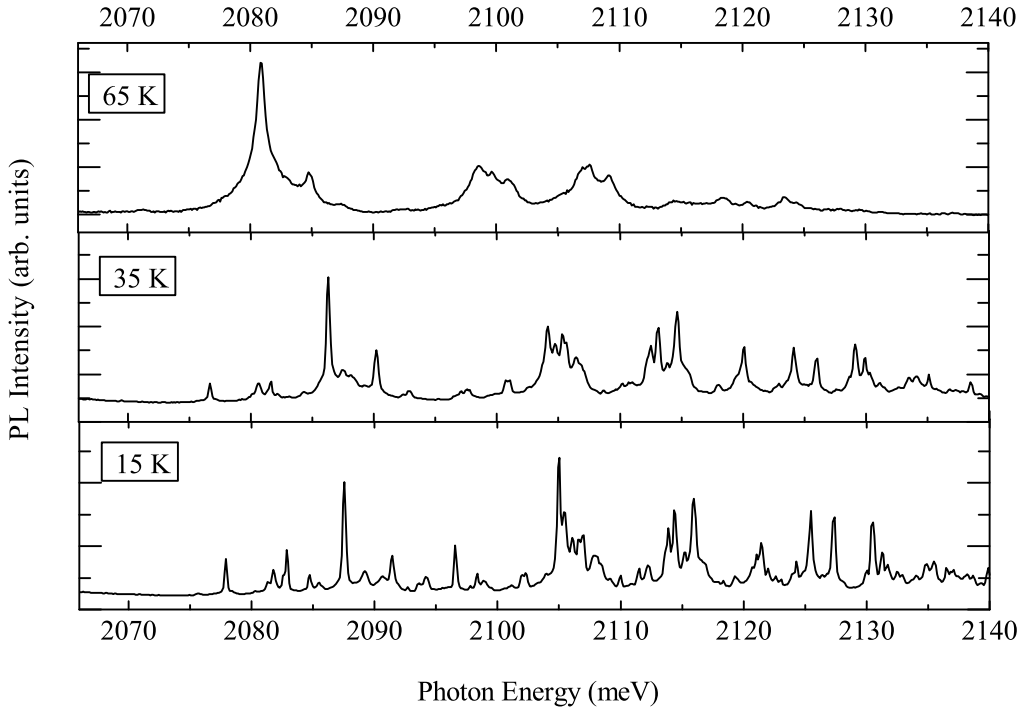

Figure 4.4: Microphotoluminescence of micropillar with diameter of 1 μm from sample C under high excitation power and at different temperatures. Individual QD lines gradually disappear with temperature growth and a characteristic pattern, dependent on micropillar size, gradually reveals the micropillar modes due to 0D photonic confinement.

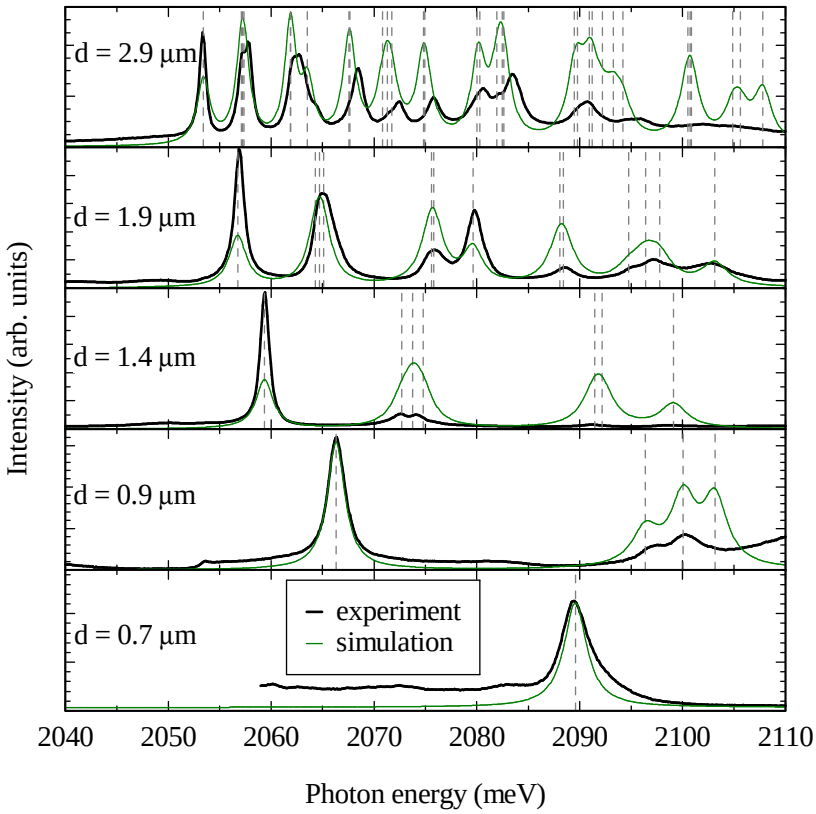

Figure 4.5: The experimental microphotoluminescence spectra of a series of micropillars (sample G) with different diameters (black lines) measured at 80 K and under strong excitation power (200 µW) are compared to spectra computed using a vectorial transfer matrix approach (green lines). Please note that the theoretical spectra do not represent the PL data but the quantity (1 - Reflectivity). The vertical dashed lines indicate the energetic position of the simulated modes.

Simulation

To find the eigenenergies and model the distribution of the electromagnetic field inside micropillar cavities two approaches are commonly used. In one of them, the so-called *finite-difference time-domain* method (FDTD), the investigated structure is discretized and Maxwell equations are calculated in finite time steps. I used this approach to get a basic flavor of the electromagnetic field distribution of micropillars with additional Bragg reflectors (see. Appendix). This method is fully numerical and requires significant computation power, although it can be easily adapted to calculate field distribution versus time in any structure. If the structure has spatial symmetry the computational effort can be significantly decreased.

The second approach remains in the frequency domain and is based on the expansion of modes of a cylindrical waveguide [Burak & Binder, 1997]. The electric and magnetic field in each layer of the micropillar is decomposed in the basis of normal modes of a corresponding infinitely long circular waveguide. The expansion coefficients are found by inducing the condition of matching of the transverse field components at a boundaries between adjacent layers. Within the so-called common-mode approximation only waveguide modes with the same mode number are coupled across the interfaces. The propagation of the field in each of the layers can be conveniently written in matrix form thus a stack of layers can then be represented as a product of the individual layer matrices. This method was used to calculate the distribution of field inside structures studied in this work. The simulations were done by Matthias Florian from the University of Bremen. This approach yields high accuracy provided that the analysis can be restricted to the confined (bounded) modes in the transverse direction, what is well justified for micropillars with sufficiently large diameters, for which the radiation in the transverse direction can be neglected.

The green lines in Fig. 4.5 show the simulated cavity spectra, wherein the refractive indices (both real and imaginary part), DBR layer thicknesses, and micropillar diameters enter as parameters. The intensity of all the calculated modes is assumed to be equal. The refractive index of the superlattice ($n_{SL} = 2.5$) was determined experimentally [Pacuski *et al.*, 2009] and other indices were taken from Ref. [Marple, 1964]. The spectral position of the individual modes is indicated by vertical dashed lines and their broadened superposition determines the shape of the calculated cavity spectra. The obtained resonant wavelengths correspond very well to the experimental spectra, which identifies the peaks in the PL as different transverse modes of the

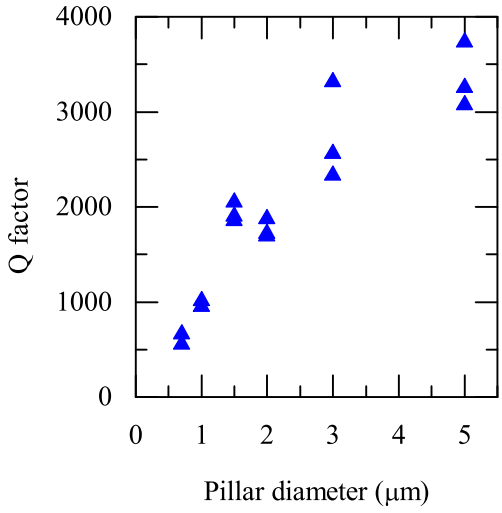

Figure 4.6: Quality factor of fundamental mode shown as a function of the micropillar diameter (sample G).

micropillar.

4.2.3 Quality factor of micropillar cavities

As already mentioned in section 4.2.2 the emission originating from a high density of QDs emitting at the spectral range of cavity modes energies enables the analysis of spectral characteristics of these modes. However, due to the Purcell effect those emitters that are at resonance with the cavity modes have emission intensity enhanced causing a distortion in the observed linewidth of the modes. Gayral *et al.* showed that in order to measure correctly the quality factor the micropillar emission should be fed by a constant number of saturated transitions that all have similar radiative recombination rates, which can be achieved in the limit of strong excitation power [Gayral & Gérard, 2008].

The spectra used to determine quality factors of the micropillars were thus measured at relatively high temperature (80 K) and strong excitation power (400 μW). A series of micropillars on sample G of diameters ranging from 0.7 to 5 μm was investigated. Fundamental modes of the micropillars were fitted with Lorentz functions to determine the quality factors of micropillars and the results are plotted in Fig. 4.6. For the micropillar with diameter of 5 μm a value of Q≈ 3700 is observed and this value decreases with the decreasing diameter of micropillars, as expected (for details see section 1.4.7). The decrease is related to scattering losses induced by the micropillars sidewalls. We do not observe signs of pronounced oscillatory variation of Q, [Lalanne *et al.*, 2004] described in more detail in chapter 1. This can

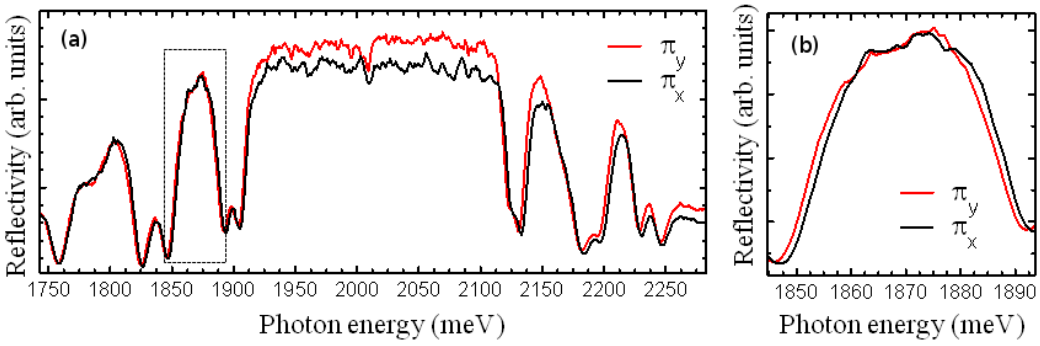

Figure 4.7: (a) Polarization resolved reflectivity of planar microcavity; (b) Enlarged fragment of the data plot

be related to a relatively large step of diameter variation, exceeding the period of oscillatory behavior.

4.3 Anisotropy of cavity refractive index

A small anisotropic splitting is observed in the reflectivity of planar samples detected with polarization resolution, as presented in 4.7. Similar effect is observed in Fig. 4.8 where I present polarization resolved photoluminescence of a micropillar with a diameter of 2 µm. It is clear that the degeneracy of the fundamental mode is lifted.

The observed effects may be explained by the anisotropy of the refractive index of materials constituting the structure. As described in more detail in chapter Technology and samples the superlattice consists of layers of ZnTe, which crystallizes naturally in zinc-blende structure and layers of crystal which typically crystallize in the rock salt crystalline structure - MgSe and MgTe, but in the discussed superlattice their growth is forced in Zinc-blende structure (thin layers). Therefore the anisotropy might be due to a strain-induced variation of the refractive index along certain crystallographic directions, resulting from growth, in one superlattice, of materials having different lattice constant and different crystalline structure.

The fundamental mode, as it is discussed in more detail in section 4.4, has an anisotropic orientation of the electric field. Thus, its energy depends on the relative orientation of this field with respect to the cavity crystalline lattice, as shown in Fig. 4.8. The above is also valid for higher order modes with anisotropy of the electric field in the cavity plane. Analogical effect is observed for elliptical micropillars where the mode degeneracy is lifted and the fundamental mode splits

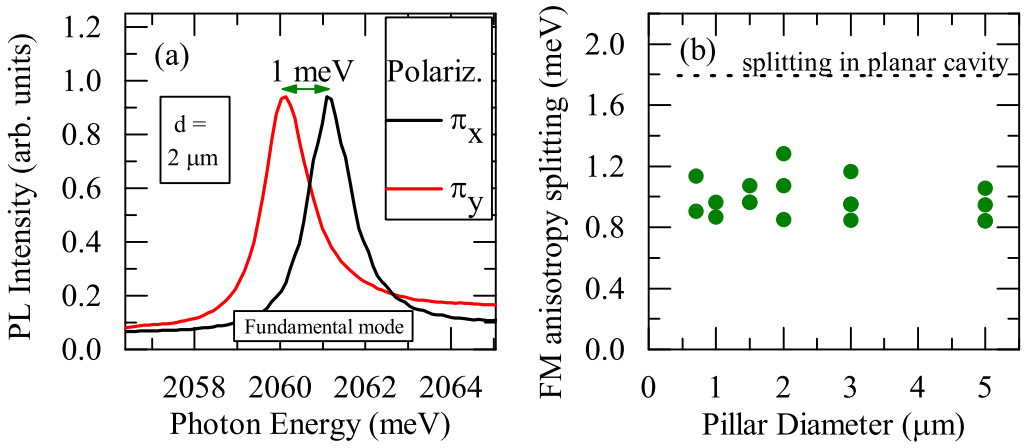

Figure 4.8: (a) Polarization resolved photoluminescence of a micropillar with diameter of 2 μm ; (b) The value of fundamental mode split extracted from photoluminescence spectra is plotted versus micropillar diameter.

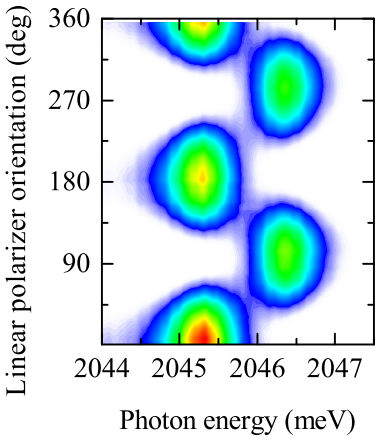

Figure 4.9: Luminescence map (in false color scale) of the fundamental mode of a micropillar collected with linear polarizer.

into two linearly polarized states [Gayral *et al.*, 1998].

As deduced from the plot of luminescence of fundamental mode collected with different orientation of the linear polarizer, presented in Fig. 4.9, orientation of the two polarizations of the fundamental mode are perpendicular. These polarizations are not aligned along crystalline axes derived from the easy cleavage directions of the crystal. In all the investigated pieces of sample G the axes of polarization X (higher energy mode) and Y (lower energy mode) are rotated with respect to the crystalline axes by 10 ± 4 degrees.

As presented in Fig. 4.8b the anisotropic splitting decreases when the sample is structured into micropillars, which would confirm the hypothesis that the anisotropy is related to strain. Indeed, HRXRD analysis of such Bragg reflectors [Pacuski *et al.*, 2009] confirmed, that the superlattice layers were grown strained on ZnTe. However, the value of anisotropic splitting is expected to decrease with the decrease of micropillar diameter as it facilitates relaxation, and this is not observed in the experiment. Further experiments, such as, for example, transmission electron microscopy imagining are required to unambiguously identify the origin of the anisotropy.

4.4 Distribution of electromagnetic field radiated from microcavities

Angular distribution of planar microcavity radiation

In planar microcavities, the photon energies of cavity modes depend on the propagation direction. In order to investigate this dependence, the method of Fourier plane imaging, described in chapter Spectroscopic setups, was used. In this method each parallel beam of light leaving the sample is focused to a single point on the focal plane, which in turn is imaged on the spectrometer slit. Figure 4.10 shows an emission intensity map of planar microcavity S1801 (sample G) obtained in this way.

The emission was simulated using a simple model of a homogeneous microcavity with two highly reflecting mirrors. This assumption is well justified experimentally and leads to the following constructive interference condition:

$$\frac{2nd}{\cos\delta} - 2d\tan\delta\sin\theta = m\lambda, \quad m \in N, \tag{4.1}$$

where: n - refractive index, δ and θ - propagation angle inside and outside of the

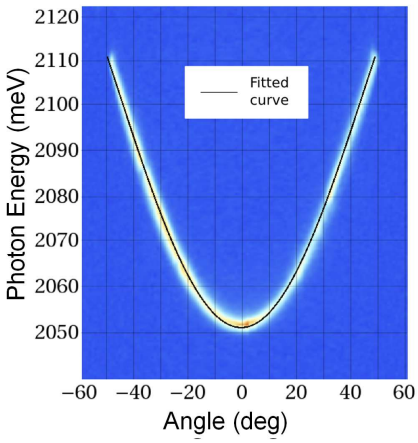

Figure 4.10: Observation angle vs photon energy map of emission intensity, measured at 60 K for the planar microcavity S1801; black line - fit with eq. 4.3.

microcavity, respectively, d - cavity thickness, and λ - vacuum wavelength. Combining this equation with one that relates the two angles according to the Snell's law:

$$nsin(\delta) = sin(\theta), \tag{4.2}$$

it leads to the following relation:

$$E_0 = E\left(1 - \frac{\sin^2\theta}{2n^2}\right). \tag{4.3}$$

The formula (4.3) was fitted to experimental data with two free parameters E_0 and n, producing an excellent agreement (Figure 4.10). The value of refractive index obtained from the fit, $n = 3.12$, is consistent with available literature data for ZnTe ($n = 3.05$)[Marple, 1964].

Spectrally resolved mode mapping

In order to image the emission of the micropillars, the setup for mode mapping described in chapter Spectroscopic setups was used. For micropillars of diameters of 1, 1.5 and 5 µm the images obtained on the CCD of the spectrometer are presented in Fig. 4.11. Unlike in the planar microcavity case, where a continuous angular dependence of emission energy was observed, discrete energy values appear for micropillar cavities. This results from the confinement of photons in all three dimensions: vertically by the Bragg reflectors and in-plane by the micropillar lateral surface. A vertical modulation, visible also in Fig. 4.11, will be discussed further below in terms of light diffraction.

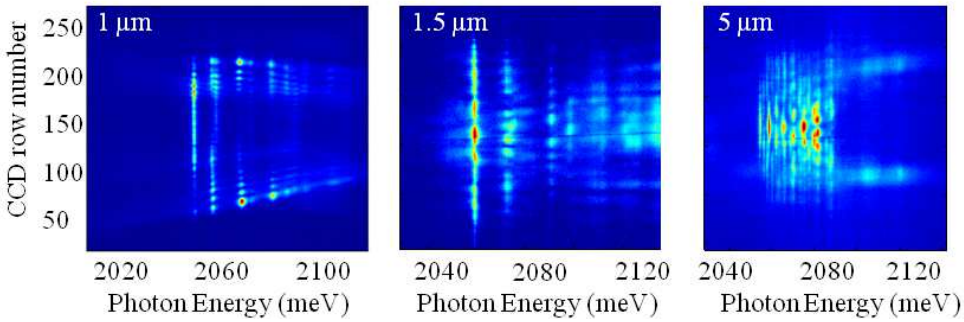

Figure 4.11: Vertical position on CCD vs photon energy photoluminescence intensity maps, measured at 60 K for micropillars with three different diameters - 1, 1.5 and 5 µm (on sample G). Figures present middle cross-sections of the micropillar images.

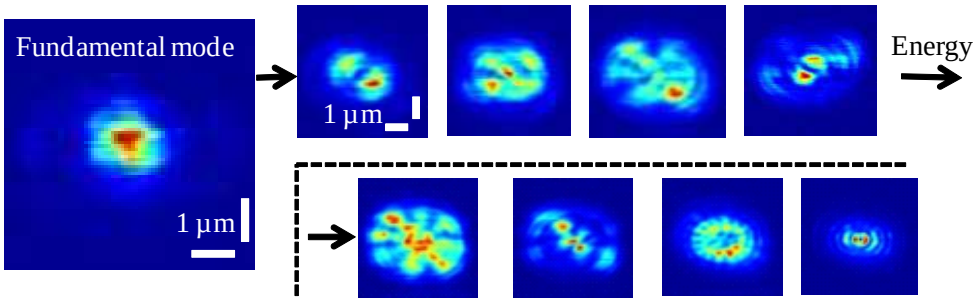

Figure 4.12: Selected results of energy resolved two-dimensional mode mapping for micropillar of diameter of 5 µm. The emission is filtered with linear polarizer.

By deflection of the beam and consecutive collection of one dimensional, energy-resolved cross-sections of the emission, a set of two-dimensional mappings was obtained for various emission energies. Polarizing optics used in the setup assured polarization resolution of the experiments. The observed radiation reflects the electromagnetic field distribution inside the micropillar. In Fig. 4.12 we present the results obtained for the micropillar with a diamter of 5 µm, as for smaller micropillars diameters the Fresnel diffraction blurred the investigated field distribution inside the micropillars (more details can be found in section 4.4.1). The first mode shows one maximum and is well centered, with maximum corresponding to the emission in the direction of the axis of micropillar. while the higher ones have increasingly more nodes and antinodes, especially in the azimuthal direction.

Simulation of intra-cavity field distribution The distribution of the electromagnetic was simulated by Matthias Florian from the University of Bremen using

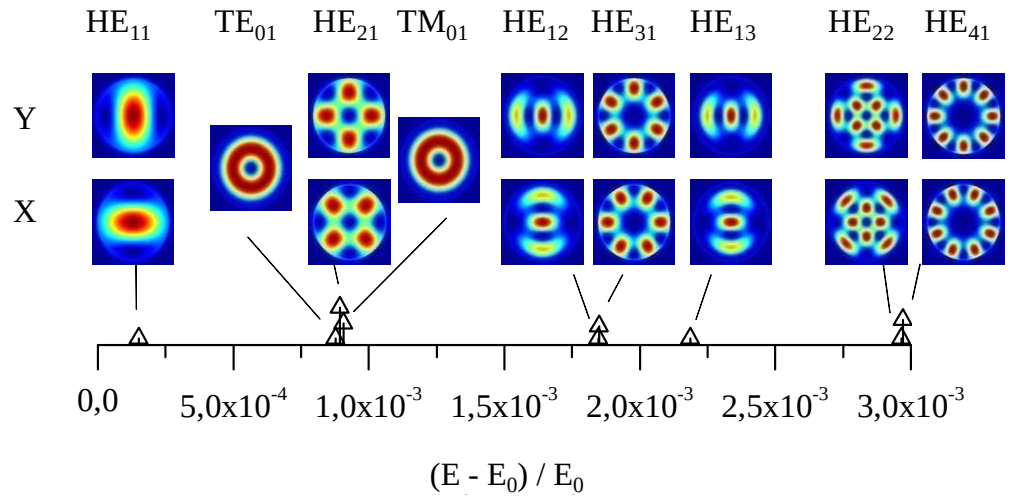

Figure 4.13: Simulated modes and relative energy position for a micropillar with a diameter of 5 µm. E_0 denotes the energy of the planar microcavity mode. For each of the modes the distribution of the amplitude of Poyinting vector along the Z axis is plotted, reflecting the distribution of the electromagnetic field intensity inside the micropillars.

the extended transfer matrix method.

The calculation assumes isotropy of shape and refractive index of the micropillars. This is required by the prerequisites of the used method. The calculated distribution of the field for a micropillar with a diameter of 5 µm are presented in Fig. 4.13. The plot presents the amplitude of the Poynting vector along the vertical axis of the pillar. The modes designation read as follows: TE_{ml} (TM_{ml}) for a transverse electric (magnetic) mode, where there is no electric (magnetic) field in the direction of propagation, HE_{ml} modes feature a non-zero electric and/or magnetic fields in the direction of propagation (see Fig. 4.14). The number of nodes in the azimuthal direction is encoded as m and in the radial direction as l. For all the modes with $m \geq 0$ there are two degenerated solutions of the field with an azimuthal dependence described by $cos(m\phi)$ and $sin(m\phi)$ (ϕ denotes the azimuthal angle), labeled X and Y respectively. The field is a linear combination of these two solutions.

The energy degeneracy of the modes is lifted if micropillars have elliptical cross section [Gayral *et al.*, 1998] or anisotropic refractive index (see 4.3). However, the exact simulation of such field is beyond the scope of this method. Therefore, as the

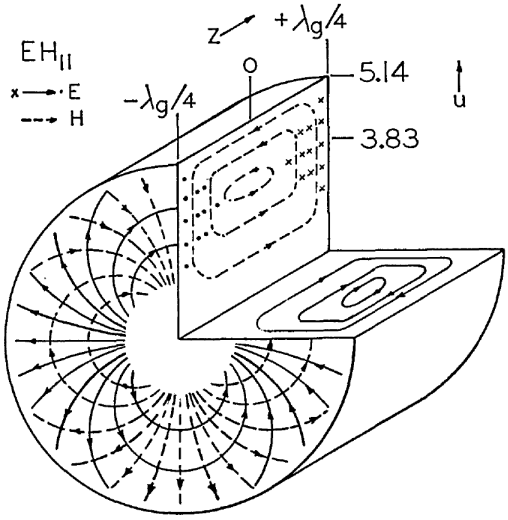

Figure 4.14: Plot of the electric and magnetic field lines of a HE_{11} mode of cylindrical waveguide having non-zero electric and magnetic fields in the direction of propagation. Note difference in notation on the figure (EH instead of HE). From [Snitzer, 1961].

experimentally investigated micropillars feature such splitting due to an anisotropic refractive index we may only qualitatively compare the simulation results to those obtained experimentally. Also, the plotted amplitude of the Poyinting vector parallel to the vertical micropillars axis can not be directly compared to experiment. This is because experimental plots were obtained with the use of a linear polarizer. Therefore they represent only the electromagnetic field with one of the two planar orientations of the electric field.

4.4.1 Small micropillar diameter - Fresnel diffraction

In Fig. 4.15 mode mapping of a micropillar with a diameter of 1.5 µm is presented. Comparing to the previously shown result an additional concentric modulation of the signal is observed in the presented maps. Such feature is observed for small diameters of micropillars and it gradually disappears for larger diameters.

We suppose that the Fresnel diffraction is responsible for the observed concentric modulation. From the point of view of diffraction the experimental setup is equivalent to a parallel beam of light diffracted on a circular aperture of diameter equal to that of the lens. The diameter of the lens is equal 5 mm and the spectrometer slit is placed at a distance of around 1.8 m. This yields around 6 Fresnel zones, characterizing the system. But this holds only under condition that the whole lens aperture is illuminated by the micropillar. However, the far-field emission profile of the micorpillars is characterized by Gaussian shape and finite angular spread of the emission angle. The aspheric lens used has a numerical aperture equal 0.68 and therefore

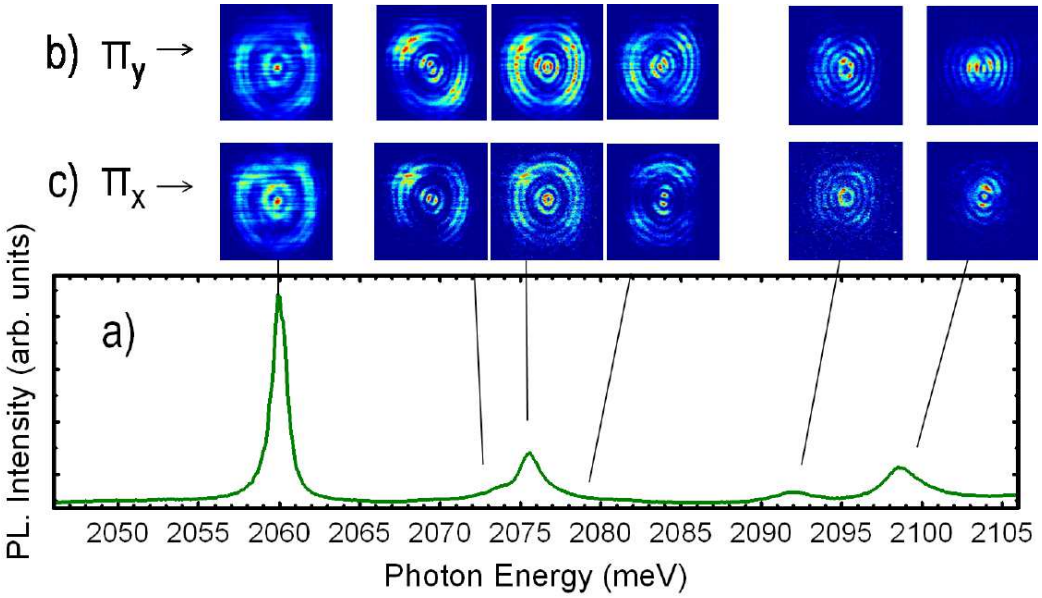

Figure 4.15: a) Microphotoluminescence spectrum, measured at 60 K for a micropillar wiat a diameter of 1.5 µm (sample G) revealing well-defined modes. b),c) Polarization and energy resolved far field emission maps of the investigated micropillar revealing characteristic modes of micropillar emission combined with diffraction pattern.

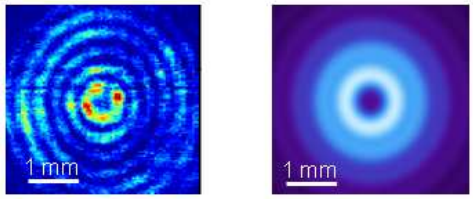

Figure 4.16: Distribution of micropillar emission intensity (sample G), measured at 1.8 m from the aspheric lens (left), compared with a simulation of corresponding Fresnel diffraction (right).

it collects the luminescence of the micropillars emitted at an angle up to around 43 degrees. The solid angle of the emission of micropillar increases with decreasing size of a micropillar [Gutbrod *et al.*, 1999], which is expected according to principles of light diffraction on apertures of size comparable to the photon wavelenght. For micropillars of diameters smaller than 5 µm the emitted radiation illuminates the whole lens more uniformly [Gutbrod *et al.*, 1999], and therefore interference fringes are more pronounced in this case. This is at the origin of the strong modulation of the resulting radiation pattern, oscillating in the radial direction.

The diffraction was modeled with free software [N.Betancort, 2001]. Numerical simulations of such diffraction for a parallel and slightly convergent or divergent beams show, that the diffraction pattern (especially the positions of diffraction maxima) is weakly affected by the convergence of the beam i.e. the position of the sample with respect to the lens focus. The simulation result is compared with the experimental emission pattern in Fig. 4.16. A striking similarity of the simulated and experimentally observed pattern is visible. Therefore we conclude that the diffraction of light on the lens aperture is the dominant source of the observed radial modulation.

Chapter 5

Purcell effect in quantum dot

In this chapter I describe the coupling of quantum dot exciton to micropillar cavity photon mode in the weak coupling regime. I discuss the influence of the cascaded emission occurring under increased excitation power on the observed decay time of the excitonic transition in resonance with a cavity mode. In the last section I describe investigations of dynamics of the emission of a single QD tuned consecutively to resonance with two energetically non-degenerated polarizations of the fundamental mode. We used time-resolved experiment to evaluate the spontaneous emission rate modification, which is a direct measure for the Purcell effect. I compare the obtained value with theoretical estimates. In the last section I present studies of the nonresonant cavity mode feeding and a modification of the intensity of emission of a quantum dot thanks to resonant coupling with the cavity mode.

5.1 Theoretical Purcell factor determination

The volume of a micropillar mode can be calculated for various micropillar diameters by using the vectorial transfer-matrix method [Burak & Binder, 1997; Jakubczyk *et al.*, 2012]. The refractive indices of the used materials [Marple, 1964; Pacuski *et al.*, 2009], DBR-layer thicknesses, and micropillar diameters enter as given parameters. Having the modes volumes calculated by Matthias Florian (Univ. of Bremen) I calculated the Purcell factor for the fundamental modes of the micropillars. It is given by the equation [Gérard *et al.*, 1998] $F = 3Q\lambda_c^3/4\pi^2 n^3 V$, where n is the refractive index at the position of the emitter (in the presented case n is the refractive index of ZnTe and taken from Ref. [Marple, 1964]), and λ_c is the resonant wavelength of the mode. This factor relates the spontaneous emission rate

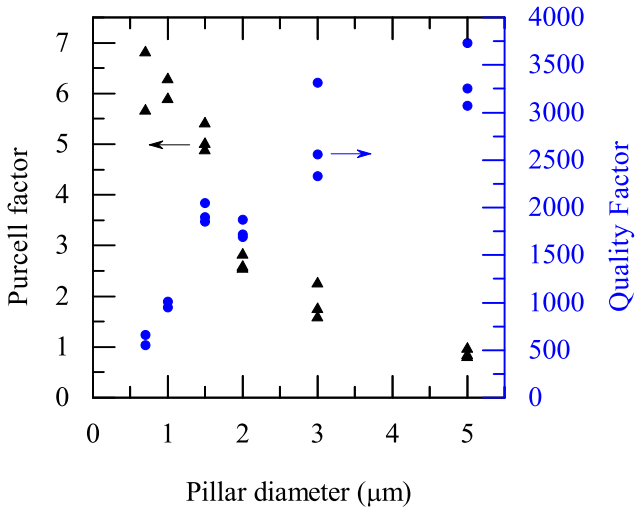

Figure 5.1: Quality factor of fundamental mode shown as a function of the micropillar diameter (circles and right axis) and Purcell factor derived from this experimental data with calculated volume of the mode (triangles and left axis).

of an emitter in resonance with a cavity mode to the total spontaneous emission rate without a cavity. The results for different micropillar diameters are shown in Fig. 5.1. From these calculations we conclude that the largest Purcell enhancement is expected in micropillars with relatively small diameter and that an enhancement of spontaneous emission rate by Purcell factor up to 7 can be expected.

5.2 Experiment

We performed time-resolved optical measurements of the photoluminescence of QDs in micropillars. The optical measurements were done in the μPL setup (for details see chapter Spectroscopic setups) in the configuration with the aspheric lens immersed together with the sample in helium gas. The photoluminescence signal was filtered with a linear polarizer aligned to one of the polarizations of the fundamental mode (for mode polarization see section sec:Anisotropy).

5.2.1 The influence of excitation power on the decay dynamics of Purcell-enhanced emission of quantum dot

Before determining the Purcell factor we had set up an experiment to find the optimal experimental conditions for observing the enhancement effect. One may

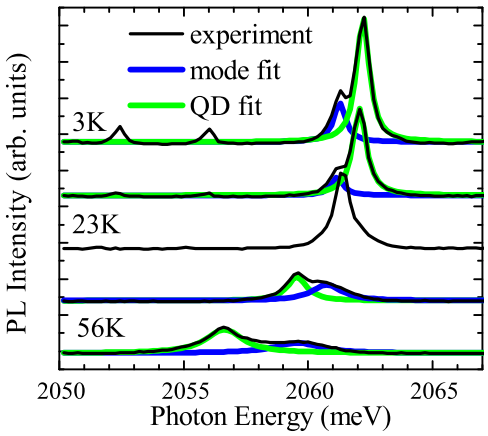

Figure 5.2: Photoluminescence spectra of the QD in the micropillar A are shown as a function of temperature. Lorentzian fits are performed for the exciton emission line and fundamental mode emission. At low temperature two additional emission lines of far detuned dots can be recognized at the low energy site of the spectra.

expect that cascaded emission from higher excited states may significantly blur the investigated fast decay dynamics. With growing excitation power the higher excitonic complexes (i.e. biexciton or the p-shell of the QD) become more populated leading to cascaded emission to the lower states, elongating the observed decay time. On the other hand low excitation power results in low signal-to-noise ratio in the collected photoluminescence which requires prolonged signal acquisition. The latter is neither optimal because of the limited stability of the QD position under the excitation beam nor usually possible in the experimental setups shared with other users. Therefore, an optimal excitation power had to be found balancing the above contradictory requirements.

In the first step we have selected one micropillar (micropillar A) with a diameter of 1.4 µm on sample G stemming from the microcavity S1801 (for details see the chapter Technology and samples). The micropillar was preselected from a group of several tens of micropillars as there was a single QD emission line in the vicinity of its fundamental mode and additionally the system showed very bright emission at resonance with one of the polarizations of the mode. As described in chapter Basic optical properties of planar and micropillar cavities the fundamental mode has two polarizations with non-degenerated eigenenergies and we investigated the one with the higher energy. The bright emission observed indicates pronounced Purcell effect [Munsch *et al.*, 2009] resulting from a good spatial matching of the QD position and the cavity mode antinode (for details see the chapter Basic optical properties of planar and micropillar cavities). The emission line is in resonance with the considered polarization of the fundamental mode at 21K (see Fig. 5.2).

To find the optimal laser excitation power, we have tuned the investigated QD

transition to the fundamental cavity mode by setting the temperature to 21 K. In the next step we have measured the decay time for different excitation power (see Fig. 5.3(b)). The decay time of the investigated transition is clearly getting elongated when increasing the excitation power. We explain the observed effect by the influence of cascaded emission. With the calculated Purcell factor we expect that the lifetime of the investigated transition at resonance with the cavity mode is of the order of several tens of ps, while the time for the transition from the higher excited state (which would not be shortened by the Purcell effect in this case) is longer than 270 ps [Smoleński *et al.*, 2011]. 270 ps is the fastest observed decay transition in CdTe/ZnTe QDs and corresponds to the biexciton. The same explanation would hold also if the observed transition was originating from a higher excitonic complex (the biexciton would have to be substituted, well understood, by a higher complex including carriers on the p shell of the dot). It is worth noting here that the capture of single electrons takes place in 20 to 40 ps after the excitation pulse, while the capture of holes is much faster [Kazimierczuk *et al.*, 2010]. As a result, the time of formation of the complexes is comparatively short and it can not play a role in the observed elongated decay time at increased excitation power.

As we want to investigate the acceleration of the investigated QD transition by analyzing the temporal profile of its luminescence, the cascaded emission from the higher occupied states is not desired. Therefore, in the experimental determination of the Purcell factor, described below, the excitation power was kept at a level well below saturation (P_0).

The observed QD transition is supposedly related to an exciton or charged exciton state. Biexcitons show a quadratic dependence of emission intensity vs power, while lower complexes show linear dependence. The investigated line is observed in the spectra in the regime of relatively small excitation power. Together with the observation that its decay time vs excitation power is characteristic for exciton or charged exciton complex we suppose that we observe one of those. In the experiment described below the unambiguous identification of the investigated transition has no importance as we measure relative change in the decay time.

5.2.2 Determination of the Purcell factor of a micropillar

In order to determine the Purcell factor for our micropillars, the time-resolved excitonic emission was measured as a function of the detuning from the cavity mode. Fig. 5.5 shows an example of a streak image collected at a temperature of 3 K, which

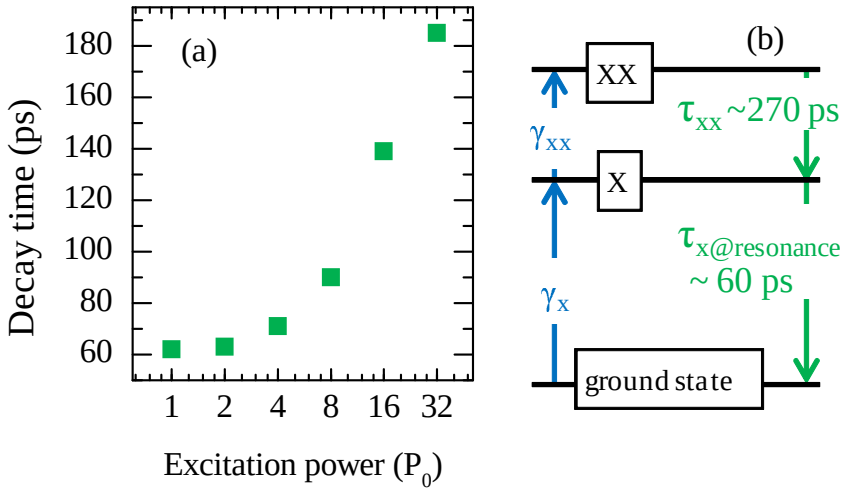

Figure 5.3: **Pillar 2** (a) Scheme of the energy levels and transitions. High excitation power causes an enhanced occupation of the biexciton state (XX) leading to prolonged decay times due to cascaded emission. (b) The excitonic (X) decay time at resonance with the cavity mode is shown versus excitation power.

corresponds to a detuning of 1.2 meV.

The choice of the resonance at low temperature limits thermally activated non-radiative recombination processes, which potentially shorten the recombination time, blurring the investigated Purcell effect.

To explore the exciton decay dynamics we have integrated the PL in a 1 meV broad frequency window around the QD emission. As can be seen in Fig. 5.4(b) the results show an exponential decay behavior, which we have fitted accordingly and extracted the exciton lifetime. To avoid the creation of multi-exciton configurations, which would lead to a prolonged decay due to cascaded emission (as discussed above), we have used low excitation power. In Fig. 5.4(c) the measured decay times are shown and exhibit a clear shortening at zero-detuning. We attribute this result to enhancement of the exciton emission due to the Purcell effect. The apparent asymmetry of the decay time as a function of detuning is related to the phonon-assisted emission of the cavity mode [Hohenester *et al.*, 2009]. At low temperature, where phonon emission is much more probable than phonon absorption, this emission channel is efficient only when the QD is on the higher energy side of the mode.

For certainty that the change in the decay time is by no means related to the temperature variation we performed a similar experiment on a reference exciton line and used QD in an unstructured environment (i.e. without the cavity). A constant

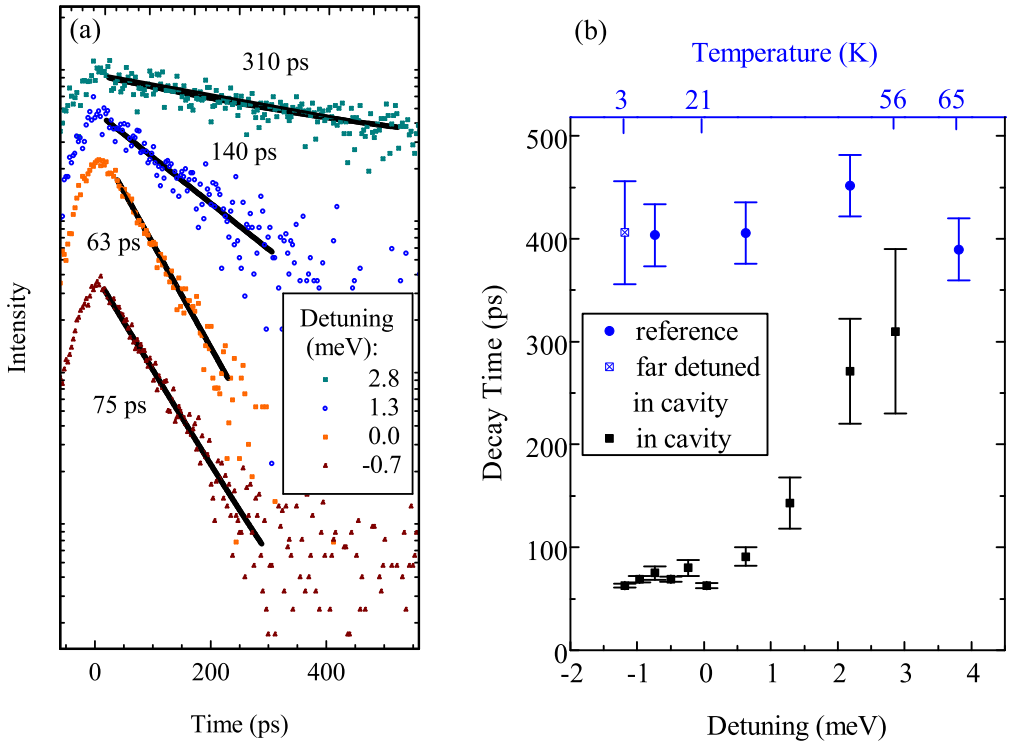

Figure 5.4: **(a)** The selected decay curves of the exciton emission in the cavity collected at various detuning are presented together with exponential fits. **(b)** Decay times for the QD in cavity are shown as a function of detuning. Decay times for the detuned emitters in the same cavity and the reference QDs are presented as a function of temperature.

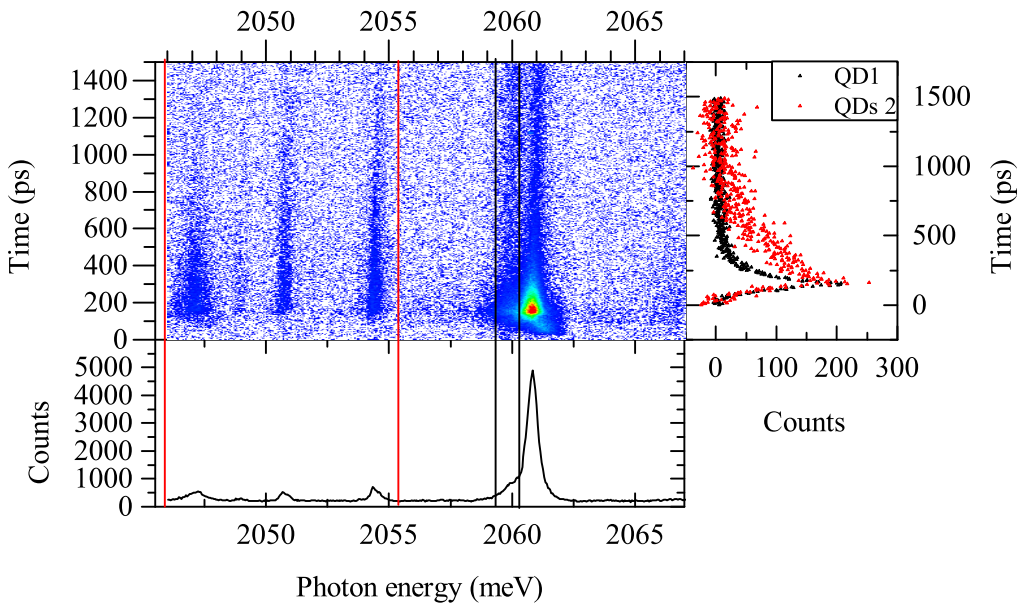

Figure 5.5: (a) Streak image of the system at 3 K; (b) The corresponding spectrum (result of the streak vertical integration); (c) Decays corresponding to the areas limited by the vertical lines on plot (a) corresponding to the QD1,which is close to a resonance with the cavity mode and three other QDs lines (QDs2) which are not at resonance.

value of the decay time of about 400 ps was obtained (see Fig. 5.4). This value is in agreement with results known for CdTe/ZnTe QDs [Kazimierczuk *et al.*, 2010]. Additionally we measured the average decay time of far detuned QD emission lines in the micropillar. This was done at low temperature (such lines are visible on the low energy side at Fig. 5.4(a)) and the resulting decay time is also close to 400 ps. This proves that the rate of the off-resonant emission is weakly influenced by the cavity. A pronounced photonic band gap and photonic modes are present only in the growth direction. The emitter can therefore couple to a quasi-continuum of "leaky" photon modes [Gérard *et al.*, 1998; Ściesiek *et al.*, 2011] and photons can be emitted in directions off the growth axis and collected due to a large numerical aperture of the lens used in the experiment (0.68).

In the case where there is no inhibition of the spontaneous emission rate for detuned emitters, the Purcell factor might be written as [Gérard *et al.*, 1998]

$$F = \frac{\tau(\Delta = \infty)}{\tau(\Delta = 0)} - 1, \tag{5.1}$$

where τ is the lifetime of the QD exciton and Δ is the detuning. In our experiment the average decay time of the reference QD is $\tau(\Delta = \infty) = (420 \pm 80)$ ps and the decay time at zero detuning is $\tau(\Delta = 0) = (63 \pm 3)$ ps. Thus we obtain a Purcell factor of $F = 5.7 \pm 0.5$. We compare this value with the calculated $F = 5$ determined earlier, which is in good agreement with the experimental value.

5.3 Polarization-resolved decay dynamics

One of the terms in the Purcell enhancement factor of spontaneous emission (see equation 1.7 in chapter Introduction) accounts for the orientation of the emitter dipole with regard to the cavity mode field. In previous reports it was shown that the polarization of the emission of quantum dots embedded within the micropillars can be controlled by coupling it with polarized photonic mode, such as fundamental mode of micropillar with elliptical cross section [Daraei *et al.*, 2006]. In such micropillar also a rotation of polarization axis and a change of polarization degree are observed as the coupling is varied [Lee & Lin, 2014].

In section 4.3 I describe a lifting of the energetic degeneracy of the two polarizations of fundamental mode of the micropillars. It presumably results from the anisotropy of their refractive index. Lifting of the degeneracy is expected to result in the Purcell enhancement only along the direction of the mode polarization, in

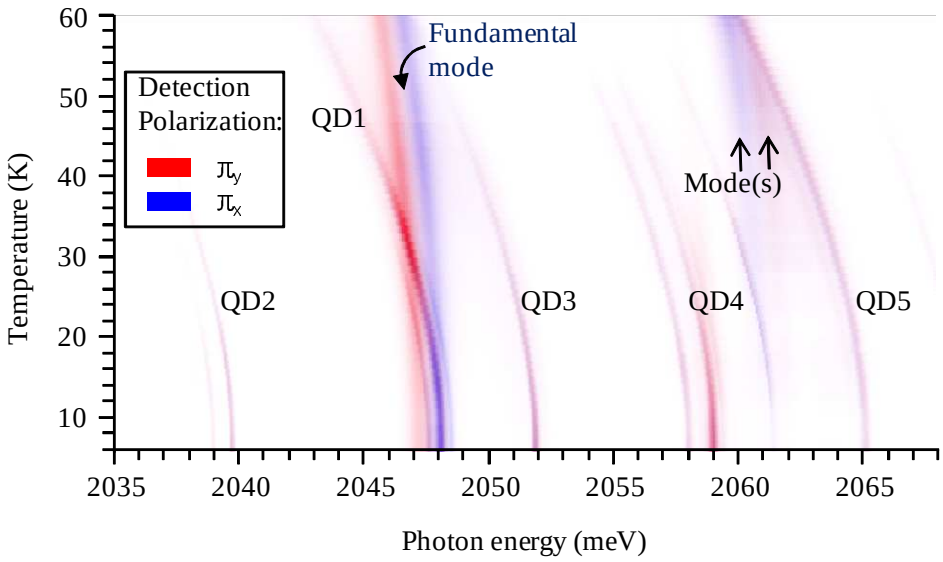

Figure 5.6: Superposition of two polarization resolved maps of photoluminescence spectra vs temperature (in false color scale). Linear polarization is encoded in color - blue (X polarization) and red (Y-polarization) and signal strength is encoded as saturation of the color.

analogy to elliptically shaped micropillars [Daraei *et al.*, 2006; Unitt *et al.*, 2005].

The luminescence attributed to exciton recombination also features two linearly and orthogonally polarized emission lines (with relatively small energy splitting), each corresponding to a spin state with a well-defined dipole direction in the sample plane. This splitting results from an anisotropy of the QD which may be related to its shape, strain or symmetry breaking at the heterostructure interface [Kulakovskii *et al.*, 1999; Stevenson *et al.*, 2002]. The lifetime of a given spin orientation is long as compared to the exciton lifetime and both states have an equal probability of occupation [Stevenson *et al.*, 2002].

We select for this experiment micropllar B, where a single QD emission line, labeled QD 1, is at resonance with one of the two states of the fundamental mode of the cavity at a temperature equal to 31 K and with the second one at 19 K. By a variation of temperature in a wide range of temperatures QD1 is consecutively tuned in resonance with both polarizations of the fundamental cavity mode. A polarization resolved map of photoluminescence spectra vs temperature is presented in Fig. 5.6. When the quantum dot states moves in and out of resonance with each of the polarizations of the observed mode the emission becomes to a large extent polarized.

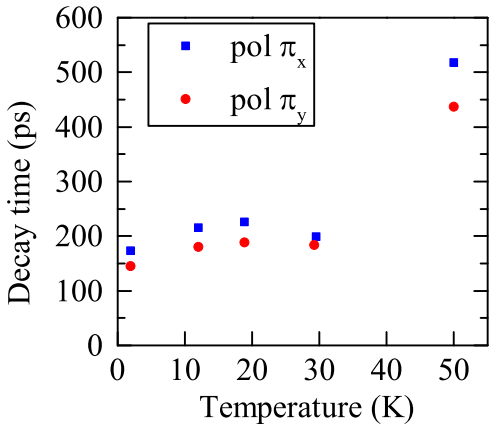

Figure 5.7: Temperature-dependent lifetimes of the QD1 measured in polarization X and Y.

in Fig. 5.7 decay times in both of the modes polarizations are presented. The experiment is similar to the one in which the experimental Purcell factor of a micropillar is determined. Decay times in both polarizations feature a similar pattern when plotted vs temperature. It shows minima for both of the resonances of QD with the two polarizations of the fundamental cavity mode. This can be explained by assuming that the orientation of the dipole moments related to the specific spin states of the QD1 exciton are tilted 45 degrees with respect to the X and Y directions of the modes. Purcell enhancement of the emission in proportional to the square of cosine function of this angle (see equation 1.7). In the proposed configuration the exciton is equally enhanced by both of the polarizations when at resonance with each of the modes.

5.4 Emission spectroscopy on coupled quantum dot-cavity micropillars

The cavity mode emission at off-resonance from emitters is commonly observed in solid state cavities like photonic crystals [Hennessy *et al.*, 2007] or micropillar cavities [Press *et al.*, 2007]. The mechanism of this coupling was intensively investigated during the last few years. It was found that the photoluminescence from an off-resonance cavity mode exhibits strong correlations with the quantum-dot transitions [Kaniber *et al.*, 2008; Suffczyński *et al.*, 2009]. A mechanism of exciton coupling to acoustic phonons and surrounding carriers resulting in fast dephasing of the QD exciton was proposed and confirmed experimentally [Suffczyński *et al.*, 2009]. Also a quasicontinuum of excitonic transitions stemming from the mesoscopic nature of

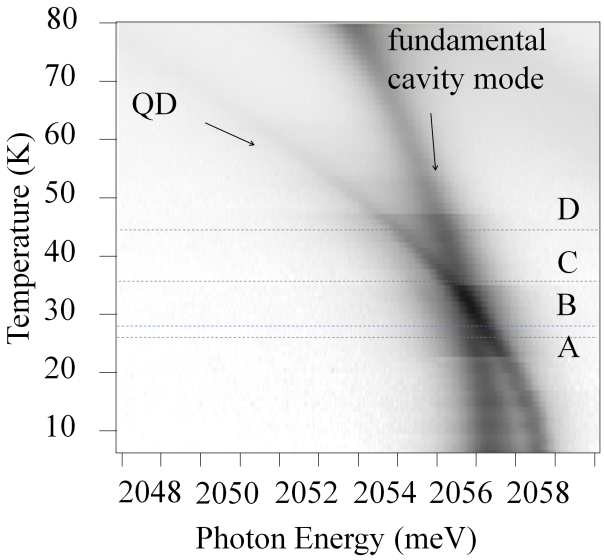

Figure 5.8: Map of photoluminescence of the micropillar C at varied temperature. The intensity is encoded in the gray scale (white- low intensity, black- high intensity).

quantum-dot confinement was proposed as a possible source of emission funneling off-resonant cavity mode emission [Winger *et al.*, 2009]. For large detuning values, such as $|\Delta E| \geq 5\,\text{meV}$ acoustic-phonon mediated coupling becomes ineffective and feeding of photons into the mode occurs from optical transitions between higher excited multi-exciton states and an energetically lower quasicontinuum of multi-exciton states [Laucht *et al.*, 2011].

5.4.1 Experiment

To investigate the mechanisms of cavity mode feeding we have selected a micropillar with diameter of 1.4 µm (micropillar C) on sample G (stemming from the sample S1801), where a single QD transition is in resonance with the fundamental cavity mode for a temperature of 33 K. We tune the QD-exciton energy difference by variation of temperature [Kiraz *et al.*, 2001], as shown in Fig. 5.8. Ramping the temperature from 6 to 80 K we collected luminescence of the micropillar every 1 K.

The emission of the QD and the cavity mode are fitted with two Lorentzian functions (see Fig. 5.9) to extract their intensities (integrated area under the respective Lorentzian functions, without background). We divided the fitting procedure in two parts, one for negative and one for positive detuning. In each case we first fit the spectrum corresponding to the largest absolute detuning value, where the fit is unambiguous as the spectra consist of two well-separated Lorentzian functions. In the next step the obtained fit parameters are used as initial parameters for the

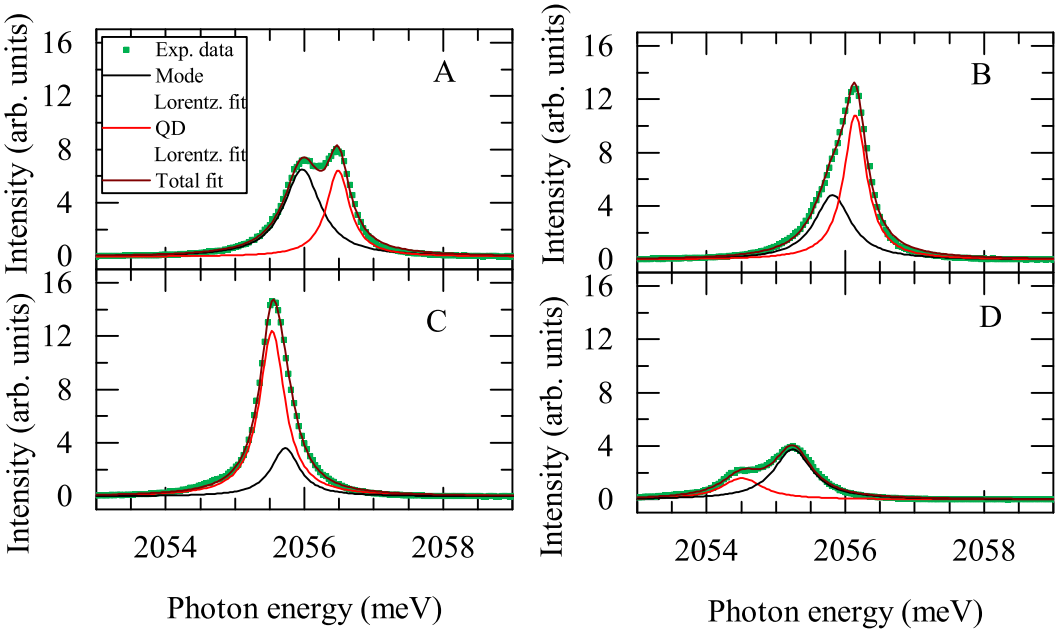

Figure 5.9: Selected two-Lorentzian fits to the emission spectra at various temperatures. A - 26 K, B - 28 K, C- 36 K, D- 44 K (the corresponding detunings are indicated in 5.10)

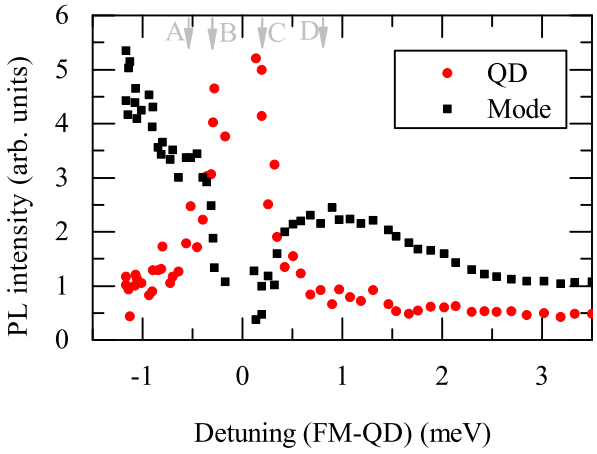

Figure 5.10: Intensity of the QD and cavity mode emission obtained by fitting the photoluminescence spectra with two Lorentzian functions.

following fit. By doing so we can increase the stability of the fitting procedure near the resonance, where the spectral overlap of the two emission lines is pronounced. This enables us to unambiguously distinguish the emission of the QD from this related to the mode. When the temperature changes by 1 K the parameters of a given Lorentzian (amplitude, width and central wavelength) change relatively little compared to the difference between parameters of both functions. Only for the two spectra measured at temperatures closest to zero-detuning (one for positive and one for negative detuning) the spectral overlap of the emission leads to a disambiguation in the fitting procedure, hence the corresponding data points are not shown. The intensities obtained in the described procedure are plotted versus detuning in Fig. 5.10.

5.4.2 Results and discussion

Off-resonance, the emission of the QD has a relatively small intensity as vertical emission, which is collected in the experiment, is blocked. The observed QD emission significantly increases at the resonance. This can be explained by the Purcell effect which results in fast emission of the QD in the cavity mode. This mode is guided in direction toward the detector [Jakubczyk *et al.*, 2011; Rigneault *et al.*, 2001], explaining the observed increase of QD intensity. It has to be noted here that we pump the system well below saturation of the QD transition so the shortening of the decay time, which is due to the Purcell effect, does not result in an significant increase in the number of events of exciton creation and radiative recombination.

The mode emission intensity also features changes when the detuning from the QD is varied. First of all, we observe decrease of this emission at resonance. The mode emission dropping toward zero near resonance evidences that apart from the analyzed QD there are no other major sources of the mode's luminescence in the observed system. The observed drop is in agreement with the reports claiming that the mode emission is related to exciton coupling to acoustic phonons [Suffczyński *et al.*, 2009] and has been predicted theoretically [Hohenester *et al.*, 2009; Naesby *et al.*, 2008], as shown in Fig. 5.11.

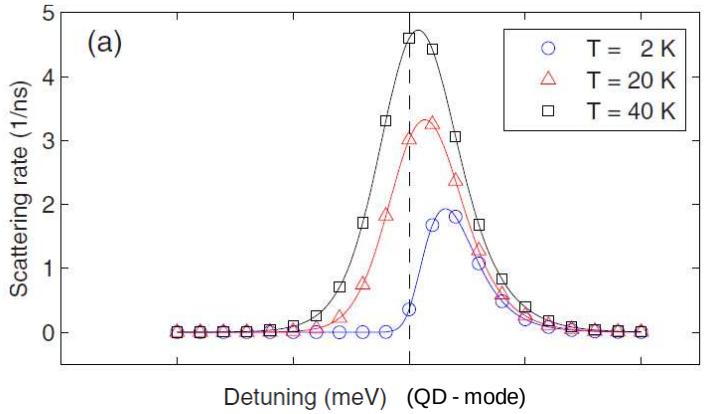

Figure 5.11: Phonon-assisted scattering rate from exciton to cavity as a function of exciton-cavity detuning, and for different temperatures. The authors use material parameters for GaAs and consider deformation potential and piezo electric interactions with acoustic phonons. For the electron and hole wave functions they assume Gaussian shapes with full width of half maxima of 6 and 3.5 nm along the transversal and growth directions, respectively. From [Hohenester *et al.*, 2009]

Chapter 6

Micropillars with radial distributed Bragg reflectors

In this chapter I present micropillar cavity in which nondesired radial emission is inhibited. The photonic confinement in this structure is improved by implementation of an additional concentric radial distributed Bragg reflector. Such a reflector increases the reflectivity in all directions perpendicular to the micropillar axis from a typical value of 15-31% to above 98%. An inhibition of the spontaneous emission of off-resonant excitonic states of quantum dots embedded in the microcavity is revealed by time-resolved experiments. It proves a decreased density of photonic states related to unwanted radial leakage of photons out of the micropillar. For on-resonance conditions, we find that the dot emission rate is increased evidencing the Purcell enhancement of spontaneous emission. The proposed design may increase the efficiency of single photon sources and bring new functionalities to micropillar cavities based on elongated decay times.

6.1 Emission from edge of a planar microcavity

To qualitatively characterize the lateral emission of vertical microcavity we collected spectra of reflectivity and luminescence of the microcavity S1801 (planar sample) containing QDs in two configurations: either perpendicular to the sample surface or perpendicular to the edge. The latter configuration is schematically depicted in Fig. 6.1. The obtained results are presented in Fig. 6.2. In the reflectivity curve, collected from the surface, the stopband of the microcavity is well pronounced. This stopband can also be observed in the surface photoluminescence spectrum. Such

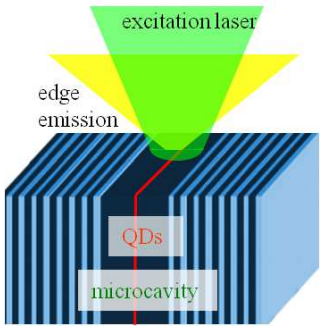

Figure 6.1: Scheme of experiemental configuration for investigation of edge emission.

emission is roughly proportional to a constant with subtracted reflectivity curve. Such result is expected for QDs in planar microcavity and is related to the photonic confinement induced by the microcavity. The edge emission features a 100 meV wide peak of Gaussian shape characteristic for the emission of an ensemble of QDs [Kobak *et al.*, 2011]. This emission seems to be unafected by its photonic environment. This experiment shows that QDs, either tuned to or detuned from the cavity mode, have an emission channel resulting in horizontal emission. We conclude that also the lateral emission of QDs embedded in micropillar cavities is little affected by micropillars photonic confinement. In the case of micropillars I will refer to the lateral direction as the *radial* direction.

In a micropillar cavity light is confined in the vertical direction by upper and lower distributed Bragg Reflectors (DBRs). In the horizontal direction it is confined only by the micropillar walls with a refractive index contrast between semiconductor and the air. The losses through the sides have a detrimental effect on the efficiency of the device. Brightness (defined in chapter Introduction by the number of collected photons in the first lens of the detection setup per excitation pulse) is a good measure of the efficiency of the micropillar. In any type of application, the brightness of a coupled micropillar-quantum dot device should be as high as possible. It is proportional to the emission rate of the dot within the guided mode and inversely proportional to the emission rate into the other, leaky decay channels. For a microcavity without inhibition of leaky modes the fraction of photons emitted into the mode equals to $\beta = F_P/(F_P+1)$, where F_P is the Purcell factor related to the mode.

Whereas for standard micropillar structures the reflectivity of distributed Bragg reflectors used for vertical confinement can easily reach over 99% [Pacuski *et al.*, 2009], the radial reflectivity in ZnTe-based micropillars equals only about 18% (31%for typical GaAs-based micropillars), depending on the semiconductor-air re-

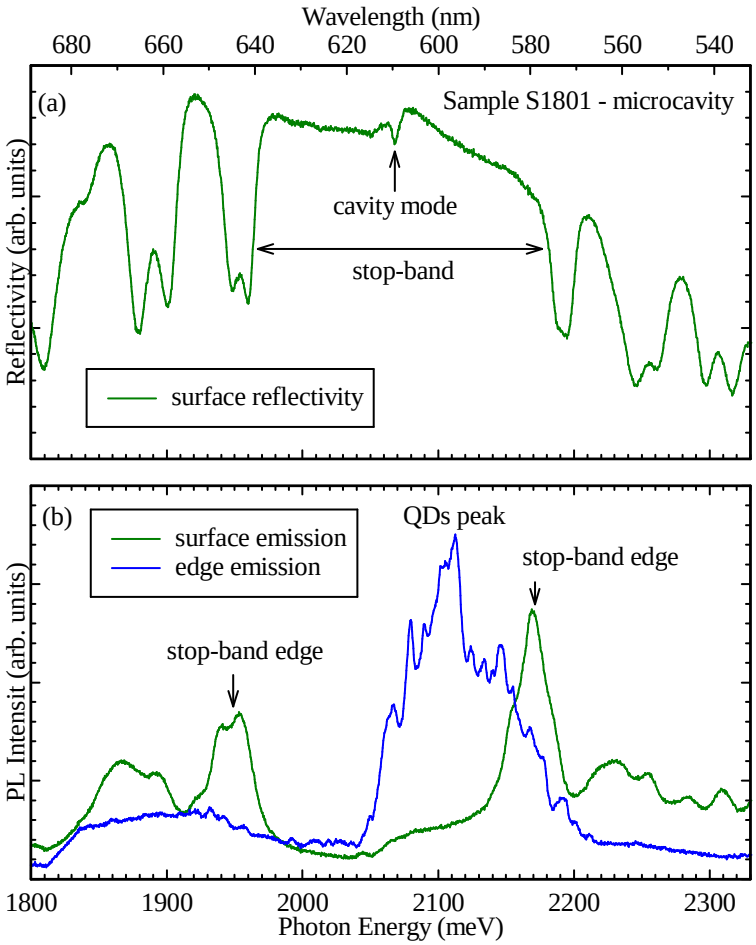

Figure 6.2: Data collected at 80 K. (a) Reflectivity spectrum measured in direction perpendicular to the surface of the sample; (b) photoluminescence spectra measured from the surface and from the edge of the sample, excitation wavelength 405 nm.

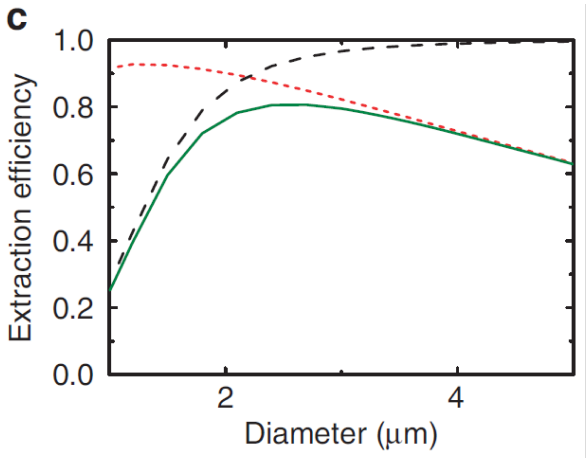

Figure 6.3: Fit of an experimentally measured Q/Q_0 (black dashed line) of micropillars based in the GaAs/InAs material system [Gazzano *et al.*, 2013a], calculated $F_P/(F_P+1)$ (red dotted line) and the maximum extraction efficiency $F_P/(F_P+1)xQ/Q_0$ (solid green line) as a function of micropillar diameters. From [Gazzano *et al.*, 2013a]

fractive index step. This is why the QD emission is lost through the sidewalls. This transverse emission, commonly described as "leaky" emission, has a great effect on the micropillar's performance. This channel is so effective that no elongation of the emission is observed for detuned emitters [Gérard *et al.*, 1998; Jakubczyk *et al.*, 2012; Lohmeyer *et al.*, 2006a]. Leaky modes also deteriorate the efficiency of single photon sources as their presence prevents the emitter from coupling 100% into the desired mode. For these reasons an inhibition of the unwanted emission into leaky modes, which out-couples QD emission in the undesirable planar direction, is one of the major challenges in the micropillar-based cavity technology.

For micropillar cavities it has been shown that the photonic bandgap for the light out-coupling in the transverse directions can be strongly enhanced by means of a silver coating of the micropillars [Poborchii *et al.*, 2003]. Suppression of coupling to leaky modes and a large increase in acceleration of the spontaneous emission of QDs resonant with the cavity modes has also been demonstrated for metal-coated micropillars [Bayer *et al.*, 2001]. However, due to losses induced by the metallic coating this technique is not considered as optimal. Furthermore, it does not allow for electrical contacting of micropillars [Böckler *et al.*, 2008].

Here we have developed an approach based on coating micropillars with oxide-based radial DBRs [Schmidt-Grund *et al.*, 2010] assuring over 98% reflectivity [Sturm *et al.*, 2009] in order to effectively suppress emission into leaky modes of the coupled QD-micropillar device [Ho *et al.*, 2007] (see Fig. 6.4). The presented method is expected to facilitate the construction of future ultra-bright light sources approaching

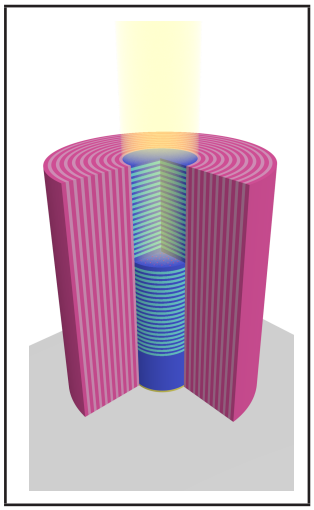

Figure 6.4: Scheme of a micropillar with an radial DBR. Micropillar is a core of the structure and is coated with cylindrical shell layers constituting an radial-trench DBR. I thank Maciej Ściesiek for preparing the figure.

the ultimate 100% limit of photon extraction efficiency.

6.2 Sample preparation

The standard planar microcavity S1801 was used. Micropillars with circular cross-sections of diameters ranging from 0.7 to 5 μm were etched on a piece of microcavity (sample E) by a focused ion beam (FIB). Compared to standard micropillar preparation, the surrounding material was etched over a wider range and at a deeper level to provide room for the radial DBR layers deposited on the micropillars in the next step. We have fabricated several tens of micropillars obtaining several micropillars with exactly one QD emitting in the spectral range close to the fundamental mode, as revealed by spectroscopic characterization. This allows us to investigate effects resulting from the coupling of a single QD line with a single cavity mode.

6.3 Deposition of radial distributed Bragg reflector

The materials for the lateral DBR should fulfill a number of specific requirements: have large difference of the indices of refraction in order to obtain high reflectivity values with already a small number of layer pairs; they have to be transparent in the considered spectral range and they should be deposited in amorphous layers to uniformly cover curved structures.

By using Alumina (Al_2O_3), and YSZ (Yttria-stabilized zirconia) researchers at the University of Leipzig are able to reproducibly grow, using pulsed laser depo-

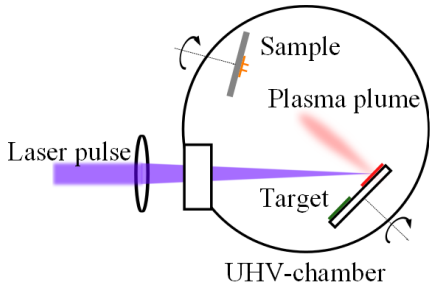

Figure 6.5: Schematic diagram of an oblique-incidence pulsed laser deposition set-up.

sition (PLD), well-tuned DBRs with smooth interfaces and low surface roughness. Especially important is the fact, that this is possible not only on planar substrates, but also on nanorods [Schmidt-Grund *et al.*, 2010]. We established cooperation to grow such DBRs on our micropillars.

Pulsed laser deposition is a technique particularly useful for the thin film deposition of complex oxides. In a PLD system the substrate and a target of the deposited material are located inside a vacuum chamber. A high-power pulsed laser beam is focused to strike the target and as a consequence the material is vaporized forming a plasma plume. The target material can be quickly choosed as it is located on a motorized stage. This determines the flexibility of the method that enables a straightforward deposition of multilayer systems, particularly important in growth of DBRs. The deposition process migth be carried either in ultra high vacuum or in the presence of a background gas. In growth of oxides oxygen is commonly used to fully oxygenate the deposited films. In oblique incidence pulsed laser deposition (OIPLD) the substrate holder is tilted to ensure deposition of layers also on vertical surfaces of the sample (*i. e.* perpendicular to the main surface). Scheme of an OIPLD setup is presented in Fig. 6.5.

YSZ is a ceramic in which the crystal structure of zirconium dioxide is made stable at room temperature by an addition of yttrium(III) oxide. These oxides are commonly called "zirconia" (ZrO_2) and "yttria" (Y_2O_3).

The micropillars were coated with a shell of YSZ/Al_2O_3 radial DBRs (see Fig. 6.8). In order to obtain a homogeneous concentric coating of the micropillars, the plasma plume axis was tilted by about 30° with respect to the normal of the rotated substrate. The DBRs consist of 10 pairs of alternating Al_2O_3 and YSZ layers. Simulation of the reflectivity of the radial DBR is presented in Fig. 6.6. The ceramic targets were ablated using a pulsed KrF excimer laser at 248 nm with a pulse duration of 25 ns and a fluence of 2 J/cm^2 at a repetition rate of 15 Hz. The growth was carried at oxygen partial pressure of 0.002 mbar and a low substrate temperature

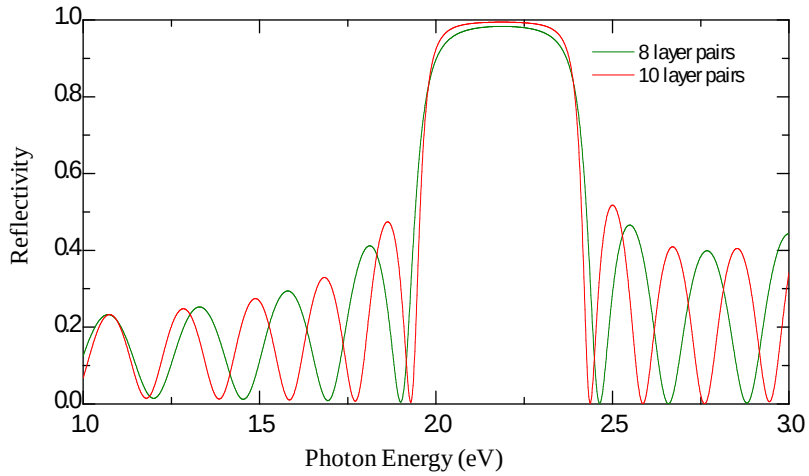

Figure 6.6: Simulated reflectivity spectrum of a DBR used for radial confinement. Simulation performed by Helena Franke from University of Leipzig.

of about 150°C in oblique-incidence pulsed laser deposition. The use of such low temperatures results in amorphous materials and smooth layers. Deposition of crystalline phase would result in a non-homogeneous coating. As a result of the OIPLD we became micropillars uniformly coated by the additional DBRs. Scanning elecron micrographs are presented in Fig. 6.7.

The refractive index contrast of the two materials used is about 0.5 (at the investigated wavelengths: $n_{Al_2O_3} = 1.7$ and $n_{YSZ} = 2.2$) [Schmidt-Grund *et al.*, 2010] leading to a stopband width of the DBR of about 400 meV. With 10 layer pairs the maximum reflectivity amounts to 98.7% at the center of the stopband at 2.2 eV, as deduced from planar samples by means of spectroscopic ellipsometry. Such stopband covers the whole range of emission of the ensemble of QDs. During the process a planar DBR grows between the micropillars. However, it does not influence the investigated properties of the micropillars.

The layers deposited with the PLD on the flat surfaces did mostly peel off (see Fig. 6.8a - peeled of layer behind the micropillar cavity). However, all the coating on the micropillars proved to be stable and durable despite repetitive cooling down and possible temperature gradients induced by laser excitation of the micropillars during spectroscopic experiments. In principle, the deposited material might introduce compressive or tensile strain on the micropillars [Voss *et al.*, 2013] depending on the relative thermal expansion coefficients, but no signature of such influence was observed in our experiments.

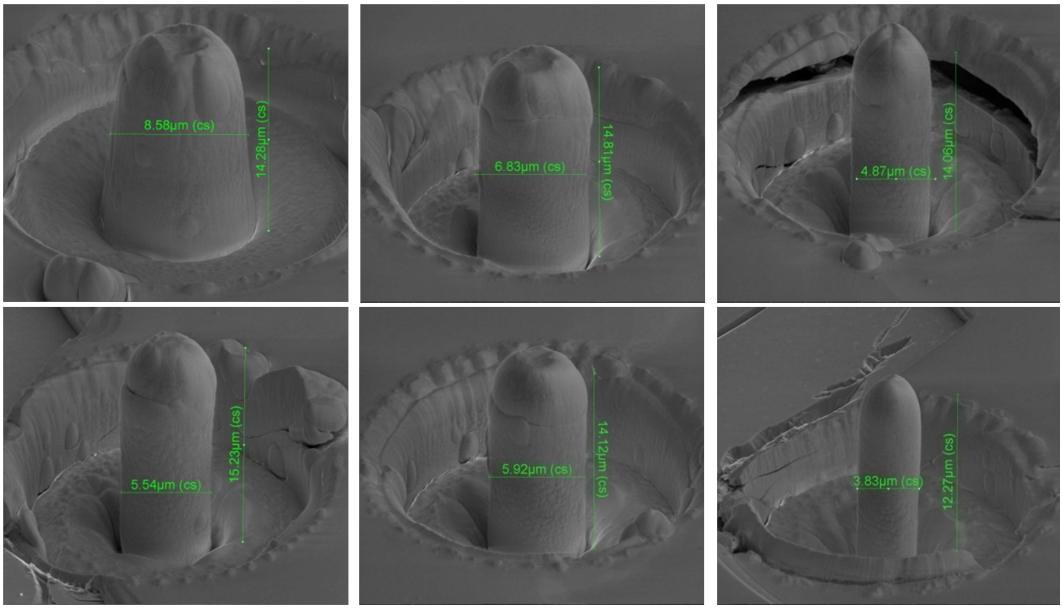

Figure 6.7: Scanning electron microscope images of micropillars after the oblique incidence pulsed laser deposition process. The diameter of the micropillars before coating was in the range from 1 to 5 1.5 µ. The apparent phallic morphology of the structures attracted a considerable attention to the presented results, also among non-specialists.

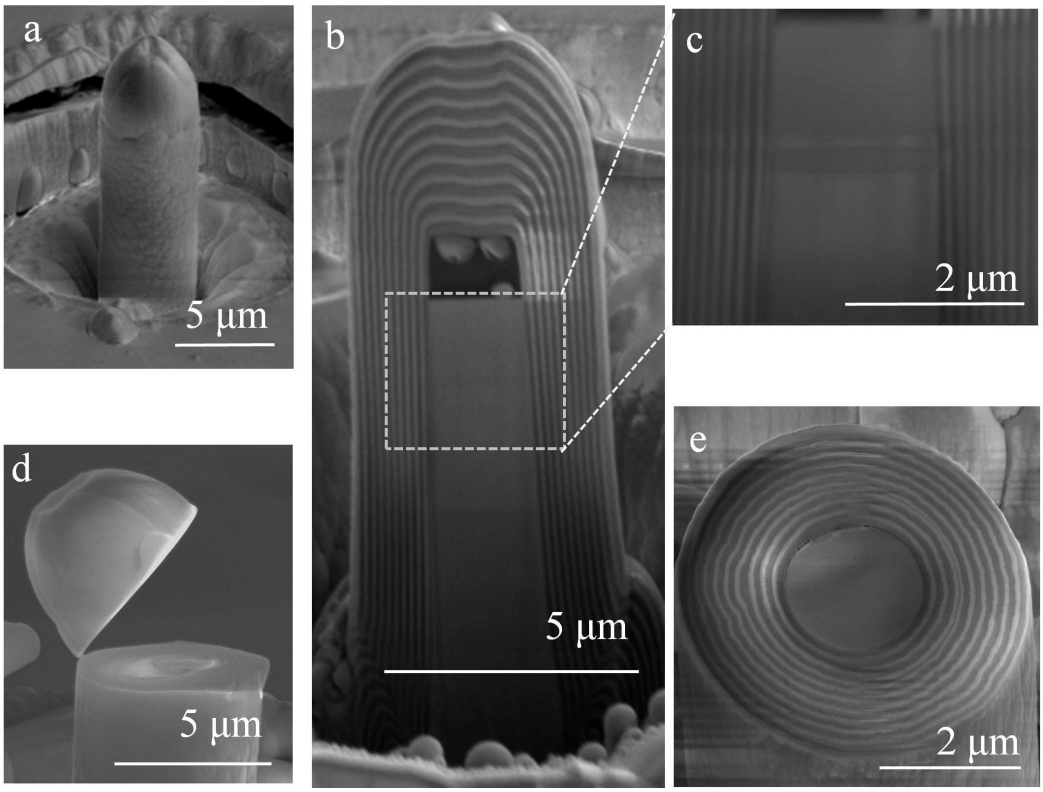

Figure 6.8: Scanning electron microscope images of micropillars. (a) Micropillar after oblique incidence pulsed laser deposition coating; (b, c) Cross-section of a micropillar showing the smooth interface between the micropillar and the radial coating; (d) Top of the micropillar during the removal process; (e) Top surface of the final micropillar structure showing a cross-section of the radial coating layers.

In order to avoid destructive optical interference in the top layers deposited by OIPLD the upper part of the coating, a sort of cap on top of the micropillars, has to be removed. Such capping has undesired optical properties as it deflects luminescence back downwards, which was confirmed by low luminescence intensity in experiments on micropillars after OIPLD (not shown). The caps were removed by FIB in a configuration where the beam is perpendicular to the axis of the micropillars (see Fig. 6.8d). This enables precise removal of the cap down to the top layer of the initially uncoated micropillar (see Fig. 6.8e) [Nesbit, 1967].

Longitudinal and cross-sectional cuts of the coated micropillars reveal the high structural quality of the radial DBR. The SEM pictures of the two surfaces depicted in (Fig. 6.8b, c and e) reveal homogeneous layers with smooth boundaries and the desired thicknesses. A photoresist layer on top of the micropillar, which can be seen in Fig. 6.8b, results from an optional two-step etching procedure of the initial micropillars described in Ref. 137.

In chapter Basic optical properties of planar and micropillar cavitiesI present discussion on optimal conditions to investigate the quality factor of the modes. With regard to conclusions of this discussion the influence of the radial DBR on the quality factor of the modes should be investigated in micropillars with high spectral density of QDs emission in the investigated spectral range. In addition, in regard to the recently reported mode distortion observed when only single QD feeds the emission of mode [Valente *et al.*, 2014](see the Appendix) conclusive information on the spectral characteristics of the emission of micropillar modes can be drawn only if the modes is "illuminated" by a large number of QDs emission lines. For these reasons I do not discuss the spectral characteristics of the micropillars here, but focus on time resolved experiments where a single QD emission line is tuned in and out of resonance with a cavity mode.

6.4 Exciton decay dynamics

To prove that the radial DBR inhibits the emission into the continuum of radial leaky modes we investigated the emission dynamics of the QDs, looking for an increase of the exciton decay time at off-resonance from the cavity modes. Such prolongation, as was mentioned before, is not observed in standard micropillars. The time-resolved optical measurements were performed using a microphotoluminescence (μPL) setup at temperatures ranging from 2 to 70 K.

We selected a micropillar of 1.5 μm diameter (diameter before the radial coating)

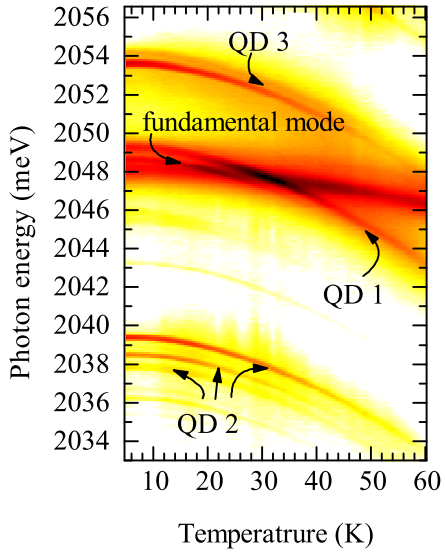

Figure 6.9: Photoluminescence map of the micropillar with QD 1 emission line at resonance with the cavity fundamental mode at 31 K and other emission lines (QD 2 and QD 3) plotted on a linear false color scale. The signal is collected with linear polarizer transmitting only one of the two states of the fundamental mode.

with radial DBR (micropillar B), where a single QD emission line, labeled QD 1, is at resonance with one of the two states of the fundamental mode of the cavity at a temperature equal to 31 K, as shown in Fig. 6.9 (with the second state, which is not shown, it is in resonacne at 19 K). In the spectral vicinity of the mode there were also other QD emission lines detuned from the micropillar mode in the range from 2 to 70 K (two lines labeled QD 2 and one line labeled QD 3) which served as reference in the experiment.

6.5 Identification of the emission line

The attribution of all the emission lines (QD 1, 2 and 3), as related to exciton or charged exciton recombination, was based on experiment with varying excitation power which is presented in Fig. 6.10. The studied lines 1, 2 and 3, when detuned from the cavity mode, show similar dependence of their intensity vs excitation power. Some other emission lines, gain faster in intensity when increasing the excitation power and therefore those other lines can be attributed to higher excitonic complexes (*e. g.* biexciton *etc.*). Whether the investigated lines are related to exciton or charged exciton recombination is not relevant in the presented experiments, as both have similar decay dynamics.

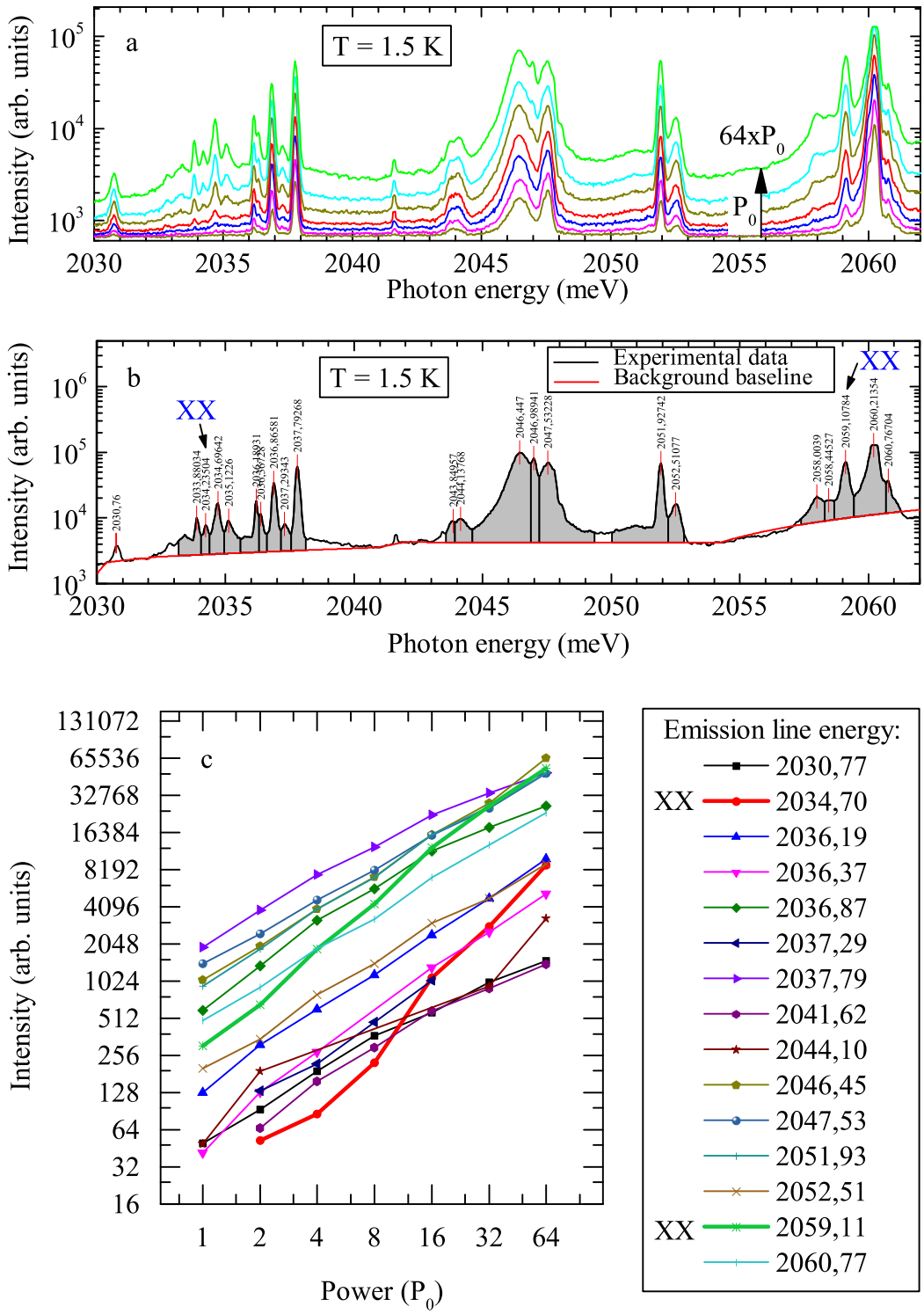

Figure 6.10: (a) Spectra collected at variable excitation density; (b) Spectrum taken at the highest excitation power plotted together with baseline of the emission ; (c) Plot of the extracted intensity of the lines vs excitation power. Baselines resulting from background emission are subtracted. The plot reveals two emission lines with above-linear intensity dependence vs power, characteristic for biexciton emission.

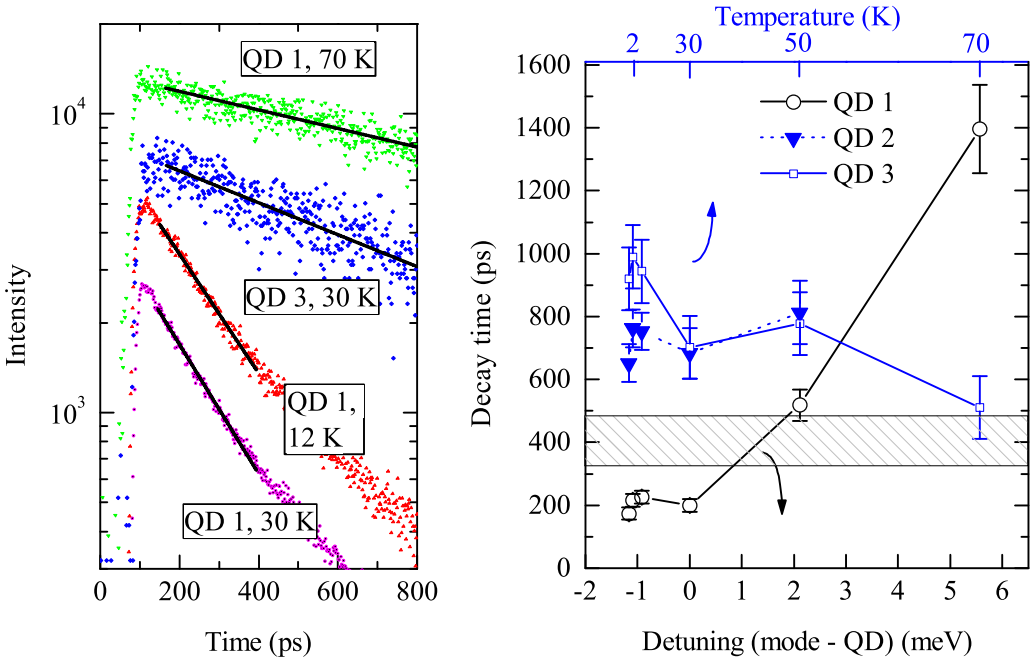

Figure 6.11: (a) Selected decay curves of the QDs emission lines collected at various temperatures (detunings) are presented together with exponential fits. The plots are vertically shifted for clarity; (b) Decay times for the QDs in the microcavity are shown as a function of detuning. The shaded area marks typical CdTe/ZnTe QDs exciton decay time range for QDs without the photonic environment and for QDs in uncoated micropillars out of resonance with cavity modes; The analyzed micropillar has a diameter of 1.5 µm, coating not included.

6.6 Emission dynamics - inhibition

We have investigated the dynamics of the emission lines 1, 2 and 3 by analyzing the temporal profile of their luminescence for various temperatures. The time-resolved photoluminescence integrated in a 1 meV energy window around the QDs emission lines shows a single exponential decay. Accordingly, we fitted monoexponential curves (Fig. 6.11a) and extracted the exciton lifetimes. These times are shown in Fig. 6.11b. The expected lifetime for an exciton (or charged exciton) in CdTe QDs embedded in a standard ZnTe-matrix lies in the range between 340 ps and 450 ps [Jakubczyk *et al.*, 2012; Kazimierczuk *et al.*, 2010]. It is clearly visible that the decay of the QD 1 line in resonance with photonic mode is significantly faster, while the off-resonant emission of all the lines is much longer.

Our previous studies have shown that the investigated micropillars exhibit a

non-degenerate emission of the fundamental mode. Due to the anisotropy of the refractive index the fundamental mode energy depends on the orientation of its electric field with an splitting equal to about 1 meV. In the presented experiment only photoluminescence with polarization attributed to the lower energy fundamental mode is shown (the same experiment is discussed also in section 5.3 with the focus on the influence of the polarization splitting). The QD crosses the higher energy mode at a detuning of around -1 meV (not shown on the map). The emission line named QD 1 has decay dynamics closely related to the detuning from both of the modes. Departure from the expected shape (sum of two Lorentz functions) of the decay time vs detuning [Munsch *et al.*, 2009] relation may result from phonon-mediated emission of the QD-cavity system [Hohenester *et al.*, 2009], also observed in the experiment described in chapter Determination of the Purcell factor of a micropillar. Basing on our previous investigations [Jakubczyk *et al.*, 2012] we assume that the oscillator strength of the QDs is constant over the temperature range considered here. The shortening of the decay time at resonance indicates a Purcell enhancement of the emission [Jakubczyk *et al.*, 2012]. For off-resonance, also in the case of QD 2 and QD 3, a considerable lengthening of the emission time is apparent as compared to QDs in an unstructured environment [Kazimierczuk *et al.*, 2010] and standard micropillars [Jakubczyk *et al.*, 2012]. We attribute this effect to an efficient suppression of the non-resonant recombination channels (i.e. leaky modes) for the QDs.

The factor of inhibition for QD 1 has a value of at least 3 compared to the free space emission. This value is the lower bound. In fact, nonradiative decay channels may be blurring the effect by shortening the observed decay time, so the real impact of the radial distributed Bragg reflector might be even higher. Micropillar cavity with QD 1 was selected for the described experiment as it shows the most pronounced Purcell enhancement and inhibition, therefore it lies probably close to the micropillar axis where the fundamental mode has its largest electric field amplitude. Randomly located QDs emitting lines labeled QD 2 and QD 3 are presumably located further from the micropillar axis than QD emitting line QD 1. As a consequence, they are more influenced by the nonradiative processes induced by the proximity of the FIB-damaged surface of the micropillar. The robustness of the effect of spontaneous emission inhibition was confirmed by the lengthened decay time in other micropillars studied in the experiment.

As the spontaneous emission in the in-plane direction is forbidden the carriers are redistributed to the states with allowed recombination channels, *i. e.* the emission

in the vertical direction. This could potentially be very important for applications in light sources, such as, for example, vertical-cavity surface-emitting lasers (VCSELs). Demonstration of such a hybrid approach also broadens the range of tools for engineering the photonic bandgap, which can be used to tailor the local density of photonic states for all quantum emitters.

The prolongation of the recombination time is promising for increasing the timescale of coherent manipulations of an exciton qubit and lifetime of the *dark* exciton. Its recombination is particularly allowed by light-heavy hole mixing. It was recently shown that the *dark* exciton lifetime is limited only by in-plane (*i. e.* radial) radiative recombination [Smoleński *et al.*, 2012], which was confirmed by a direct observation of its photoluminescence from a cleaved edge of the sample. The prolongation of dark exciton lifetime is desired in possible applications of this complex as a coherently controlled qubit [Poem *et al.*, 2010].

In principle, the radial DBR should allow for electrical contacting of the micropillars. Their wide top surface may facilitate deposition of the top electrode in existing schemes of micropillar contacting [Böckler *et al.*, 2008].

A potential drawback of the presented design is that the radial confinement may introduce additional scattering losses and as a result the Q-factor of the micropillar may be decreased. However, by using Bloch-wave engineering of the micropillars [Lermer *et al.*, 2012] (described briefly in chapter Introduction) this undesired effect can be eliminated. This is because micropillars constructed in this way have the electromagnetic field of the mode well concentrated along axis of micropillar, and therefore the mode is less prone to scattering on the sidewalls.

Chapter 7

Growth of quantum dots and distributed Bragg reflectors on GaSb substrates

In this chapter I describe growth of QDs and DBRs on GaSb-substrates. This material has almost the lattice constant constant as ZnTe (the mismatch equals only 0.13 %) and it is expected to allow almost lattice-matched epitaxy. I investigated the optical properties of the obtained structures by spectroscopic methods. The lattice match of the structures was controlled by high resolution X-ray diffraction (HRXRD) measurements.

As described in previous chapters ZnTe-based microcavities deposited on GaAs substrates proved their ability to efficiently modify the emission of CdTe/ZnTe quantum dots [Jakubczyk *et al.*, 2011; Ściesiek *et al.*, 2011]. However, the lattice mismatch of 7.30% between the GaAs substrate and the ZnTe-based structure results in a large density of misfit dislocations. Therefore thick ZnTe buffer layers are required prior to the growth of the intended epitaxial structure to minimize the formation of crystal lattice defects. About 1 µm-thick ZnTe buffer used in the microcavity S1801 investigated in this thesis was probably not thick enough to obtain best possible crystal quality [Fan *et al.*, 2011]. Thoug, thicker buffers are not only time consuming in epitaxy (typically many hours of growth) but also they lower the optical quality of the microcavity due to additional optical interferences with high spectral density.

Much better crystalline and optical quality could be obtained if ZnTe substrates were used [Nomura *et al.*, 2004, 2006a], but they are two orders of magnitude more

expensive than GaAs. Significantly cheaper and almost lattice matched to ZnTe are GaSb substrates. The idea of growing ZnTe on GaSb has been already utilized since 1971 using the advantage of the large difference in the melting points (ZnTe = 1295 °C and GaSb = 702 °C) fabricate a heterojunction in the so called interface-alloy technique [Kamuro *et al.*, 1971]. Growth of ZnTe/GaSb heterostructures is also developed for more than two decades in MOCVD [Dumont *et al.*, 1993; Leiderer *et al.*, 1991] and MBE [Rajakarunanayake *et al.*, 1989]. However, although heteroepitaxial structures of ZnTe (a = 0.613 nm) and GaSb (a = 0.609 nm) were obtained already in the early 70's high-quality GaSb substrates of sufficient size (diameter over one inch) are commercially available since just a few years ago. Reports following this achievement have proven that GaSb is an excellent substrate for the growth of high quality ZnTe-based structures [Fan *et al.*, 2011; Pimpinella *et al.*, 2010, 2011; Wang *et al.*, 2009], thanks to the low relative lattice mismatch.

Our motivation for this research is to improve the quality of microcavities with QDs, although in a broader context we aim at developing vertical cavity surface emitting lasers with QWs as the active material, where the crystal quality determines efficiency of the device.

7.1 Substrate preparation

We used GaSb (0 0 1) oriented substrates provided by *NewWay Semiconductor Inc.* company. GaSb surfaces are very active chemically and easily oxidized. Thus, a several-nm thick oxide layer can be expected on the as-received GaSb substrate surface [Liu *et al.*, 2003]. Such layer has a detrimental effect on the quality of the layers grown on the wafer. Therefore deoxidation is an important step in the preparation of a substrate before the growth.

Basing on previous reports [Liu *et al.*, 2003] we optimized a procedure in which the surface is treated by HCl . It solves the oxides. Two substrates were rinsed in a solution with 37% HCl concentration for either 1 minute or 2 minutes, followed by a 2-propanol rinse. After this step the substrates were dried with gas nitrogen to remove droplets of 2-propanol, then placed on substrate holders and immediately delay loaded to the MBE ultra-high vacuum system. A third substrate was loaded in a state as-received from the producer.

In the next step the possible residue oxides and chlorine-based species, possibly formed on the surface during HCl rinse [Liu *et al.*, 2003], were thermally desorbed in the UHV chamber at a temperature between 500 and 540 °C. Higher temperatures,

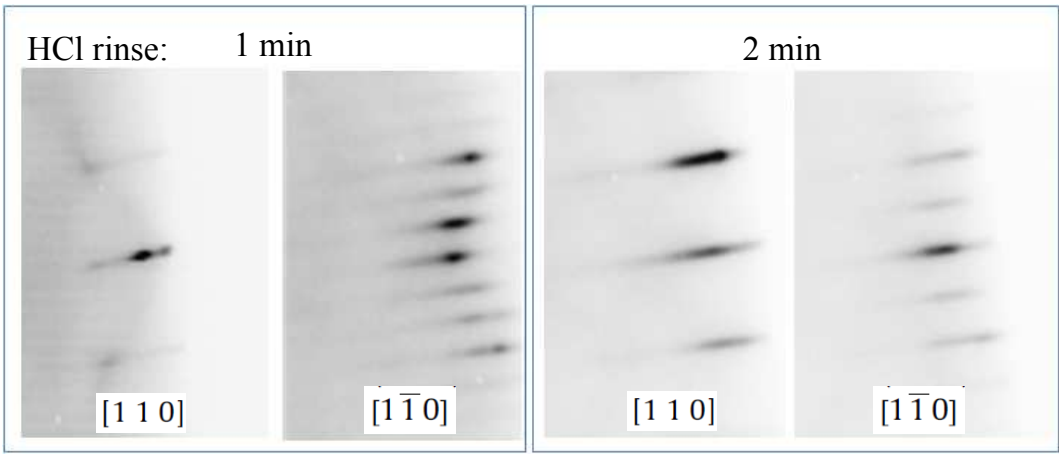

Figure 7.1: RHEED pattern of GaSb substrates rinsed in HCl. (1 x 3) reconstruction is observed for the substrate rinsed 1 minute and (1 x 2) for the one rinsed 2 minutes. For each substrate the left figure refers to [1 1 0] and the right to the [1 $\bar{1}$ 0] axis.

however favorable to fully desorb the unwanted species, lead to significant decomposition of GaSb. This results in formation of three-dimensional metallic Ga-rich clusters [Liu *et al.*, 2003].

After the deoxidation procedure we investigated the surfaces of all three GaSb substrates with reflection high energy electron diffraction (RHEED - for details see chapter Technology and samples). Results are presented in Fig. 7.1. In the case of substrate rinsed for 1 minute we observed the surface (1 x 3) reconstruction typical for GaSb. For the substrate etched 2 minutes the (1 x 2) reconstruction is observed indicating deviation from the optimal surface composition. For the substrate which was not rinsed in HCl at all, there were no interference fringes in the RHEED signal, signifying presence of amorphous material on the surface. As a conclusion of this study, we used the procedure with 1 minute HCl rinse as a standard for preparation of GaSb substrates.

7.1.1 Growth of quantum dots

To adjust growth parameters on GaSb, in particular the substrate temperature, we grew a sample with QDs. QDs were grown by the method using Zn-induced formation process [Kruse *et al.*, 2011] described in chapter Introduction. In the next step we used the same QD-formation recipe on GaAs with ZnTe buffer layer. The scheme of both structures is presented in Fig. 7.2.

To initiate growth of ZnTe on GaSb the migration enhanced epitaxy is used

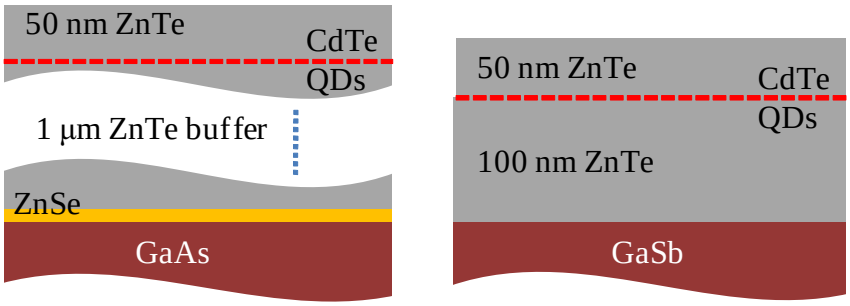

Figure 7.2: Scheme of sample containing QDs grown on GaAs substrate (left) and GaSb substrate (right).

(MEE). The idea of this technique is to supply the participating elements alternately enhancing their surface diffusion [Gaines *et al.*, 1993]. Since in the growth of II-VI and III-V heterostructures the related III-VI compounds are commonly formed at the interface we used Zn-irradiation to prevent formation of Ga_2Te_3 before starting the MEE procedure. In the case of the sample grown on GaAs a standard ZnTe buffer was grown. The rest of the procedure was identical for both samples.

We performed spectroscopic characterization of both samples. We measured their photoluminescence under the same experimental conditions. The emission peak of QDs grown on GaSb is shifted toward higher energies by about 90 meV. We relate this to the fact that GaSb has narrower bandgap than GaAs and therefore it absorbs more radiation from the substrate heater during growth in the MBE system. Higher temperature of the substrate results in a higher material evaporation rate during the growth leading to thinner epitaxial layers. This causes smaller size of the dots and higher emission energy of the QDs on GaSb.

Next, we grew a second QDs sample on GaSb lowering the substrate temperature by 20 °C and performed once again spectroscopic characterization, The results are presented in Fig. 7.3. The emission energy of the QDs ensemble on GaSb substrate matches that of the GaAs sample, suggesting an equal substrate temperature in both cases. This temperature, measured using a thermocouple kept in contact with the substrate holder is in the range $300 - 320\,°C$ and is consistent with previous reports describing optimal epitaxial growth parameters on GaSb substrates [Fan *et al.*, 2011].

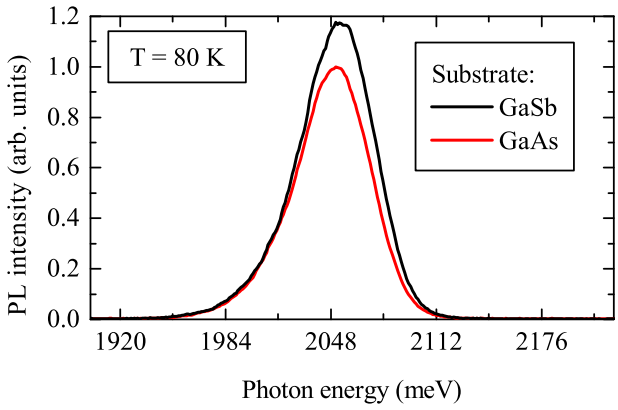

Figure 7.3: Photoluminescence of CdTe/ZnTe QDs grown on two different substrates, GaAs and GaSb, showing higher intensity for QDs grown on GaSb.

The ensemble of quantum dots grown on GaSb show luminescence intensity by about 20% higher comparing to the sample grown on GaAs substrate, as presented in Fig. 7.3. We interpret this result as an indication of improved quality of ZnTe grown on GaSb. This can be attributed to smaller defect density in the epilayer related to its smaller lattice mismatch with the substrate. We expect that moderate increase of QDs luminescence can indicate a substantial enhancement of crystal quality. This is because QDs emission intensity is less susceptible to dislocation density than emission of bulk material or QWs. In reports where the photoluminescence of bulk ZnTe grown on GaSb and GaAs was compared the emission intensity difference was much higher, of the order of factor 5 [Fan *et al.*, 2011]. Therefore, although the QDs increased photoluminescence intensity seems not to be a major progress compared to QDs grown on GaAs substrates, we decided to continue the development of ZnTe-based vertical cavities on GaSb substrates in the context of development of building blocks for future vertical-cavity surface emitting laser. Therefore, in the next step we developed technology for the growth of ZnTe-based DBRs on GaSb substrates.

7.2 Growth of distributed Bragg reflectors

We grew ZnTe-based distributed Bragg reflector analogous to those described in chapter Technology and samples, this time on GaSb substrate and without the ZnTe buffer layer. To maximize reflectivity, the optimal order of layers in such DBR is obtained by growing the superlattice layer directly on the substrate. After Zn irradiation (as in the case of growth of QDs) we begin the growth of superlattice starting with the ZnTe layer, as presented in Fig. 7.5 (for details of the superlattice see chapter Technology and samples) grown by MEE. The rest of the procedure is

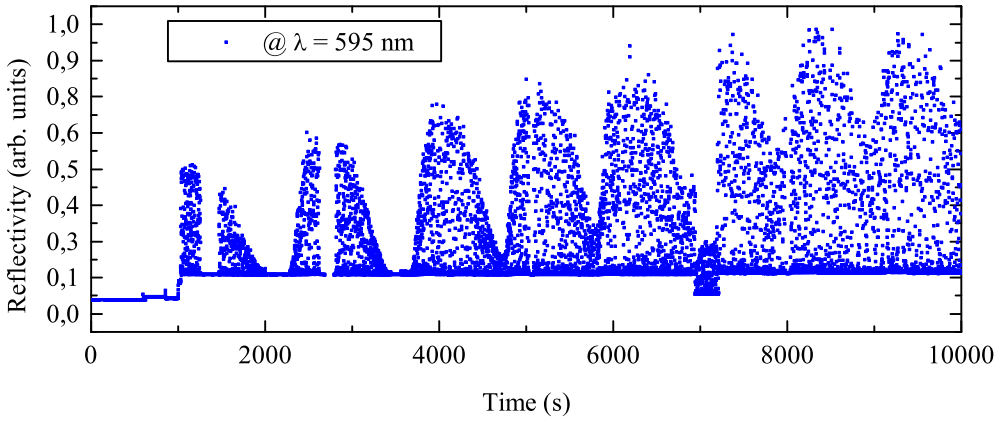

Figure 7.4: Reflectance vs time during epitaxial growth of DBR (sample H1) at 605 nm. The growth of the high refractive index material to the low refractive index one is performed when the reflectivity has its maximum (respectively minimum for the low to high index material change).

the same as for standard DBRs grown on ZnTe. *In situ* reflectivity (see chapter Technology and samples) measured at $\lambda = 595\,\mathrm{nm}$ was used to adjust the $\lambda/4n$-thickness of the two DBR components, where λ is the central wavelength for which the mirror is designed and n is the refractive index of the respective layer. Plot of reflectance vs time is shown in Fig. 7.4. The reflectivity was sampled at a constant rate. Rotation of the sample on a slightly uneven holder and activation of the main shutter of the MBE system during the growth results in a fast variation of the signal. We use the envelope of the data as the actual value of reflectance.

The growing material was changed between this featuring the higher and this with the lower refractive index in the moment, where the DBR reflectivity has, respectively, a local minimum or maximum.

We grew a series of DBR samples. After each growth we used high-resolution X-ray diffractometry to compare the superlattice lattice constant with that of ZnTe and GaSb. The variation of relative thickness of MgSe and MgTe layers allows to adjust the lattice constant of the superlattice layer. In steps we adjusted the parameters of the superlattice layer to match ZnTe. In Fig. 7.6 I present the result of characterization of the final DBR sample (sample H1) plotted together with a simulation. For the simulation the adjusted parameters are the thicknesses of the respective materials and the refractive index of the superlattice. The peak related to ZnTe is close to this related to GaSb, as expected. In the graph there are also

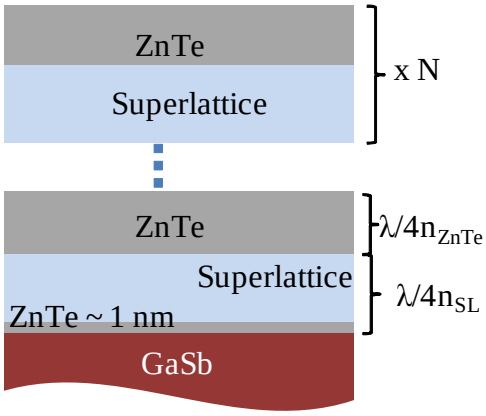

Figure 7.5: Scheme of the DBRs grown on GaSb

7 peaks related to the superlattice. The spacing between fringes corresponds to a superlattice period length equal 3.6 ± 0.1 nm. It is similar to the ones found for the ZnTe-based DBRs [Pacuski *et al.*, 2009]. The zero-order peak postilion indicates a larger lattice parameter of the superlattice than that of ZnTe. The experimental peaks are broader than the simulated one. This might be related to such defects of the crystal lattice as mosaicity, dislocations and curvature. To determine if the grown ZnTe and superlattice layers are relaxed or strained the sample was studied once again with high resolution x-ray diffraction. Figure 7.7 shows a mapping in a range of the reciprocal space close to 335 x-ray reflex. The resolution of the map doesn't allow to unambiguously determine all the features observed around the GaSb, ZnTe and zero-order superlattice. Hovewer, it is clear that the fringes related to the short period SL are vertically aligned to the spot of ZnTe. This shows that the superlattice is grown strained with the lattice parameter of ZnTe. The peak related to GaSb can not be identified unambiguously. However, we see a slight assymetry around the vertical line, which may be related to the GaSb peak. The GaSb peak is indeed expected on the right side of the vertical line as GaSb has smaller lattice constant than ZnTe. Different Q_x parameter of GaSb compared to ZnTe and superlattice indicates relaxation of the epitaxial layers. This is expected, as the critical thickness for pseudomorphic growth of ZnTe on GaSb is in the range from below 180 nm [Tomasini *et al.*, 1996] to 460 nm [Cohen-Solal *et al.*, 1994] and our structure is several μm thick. Moreover the larger lattice constant of the superlattice is expected to trigger strain relaxation in the ZnTe layers. This is favorable for our future vertical cavities. Since it is unlikely to grow the whole structure in the GaSb

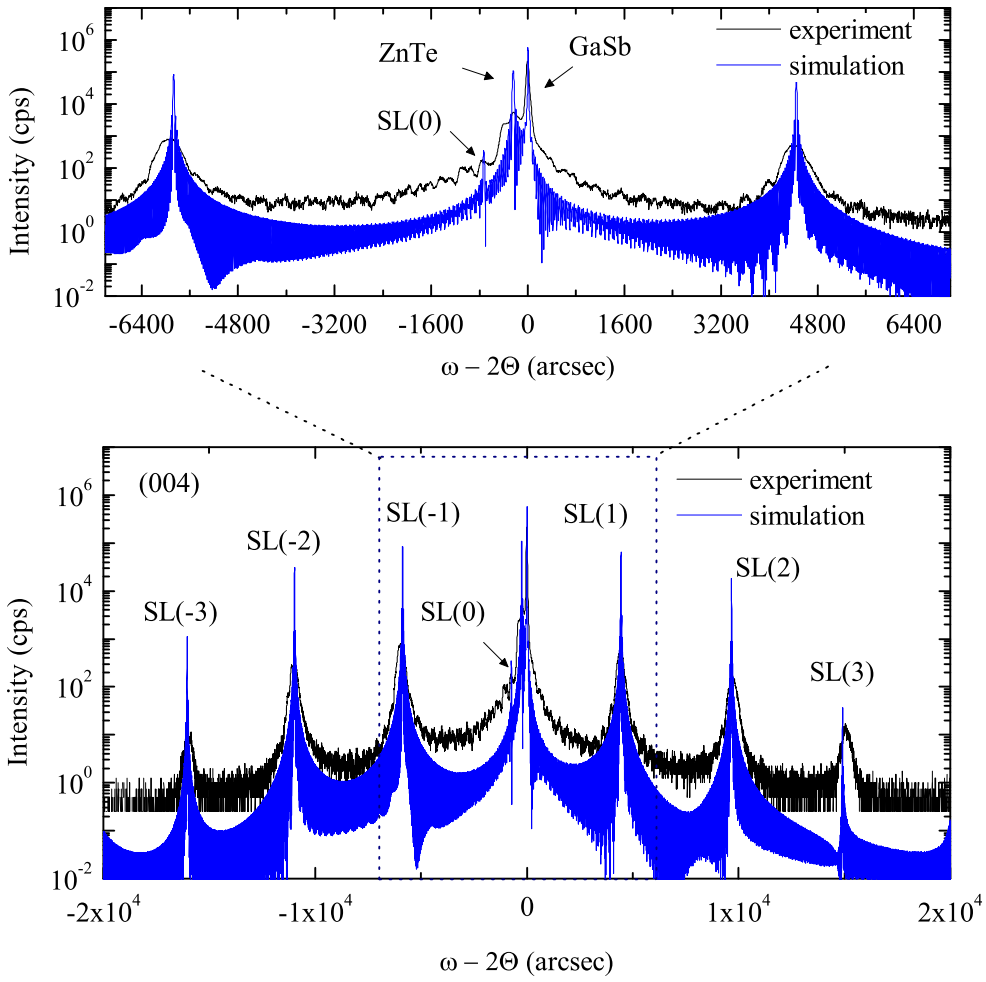

Figure 7.6: HRXRD data of the DBR sample H1. $\omega - 2\Theta$-scan of the (004) reflex and simulation. The magnification is added for clarity.

lattice constant it is favorable to induce the relaxation close to the ZnTe/GaSb, keep thusly formed dislocations far from the optically active layer of the cavity.

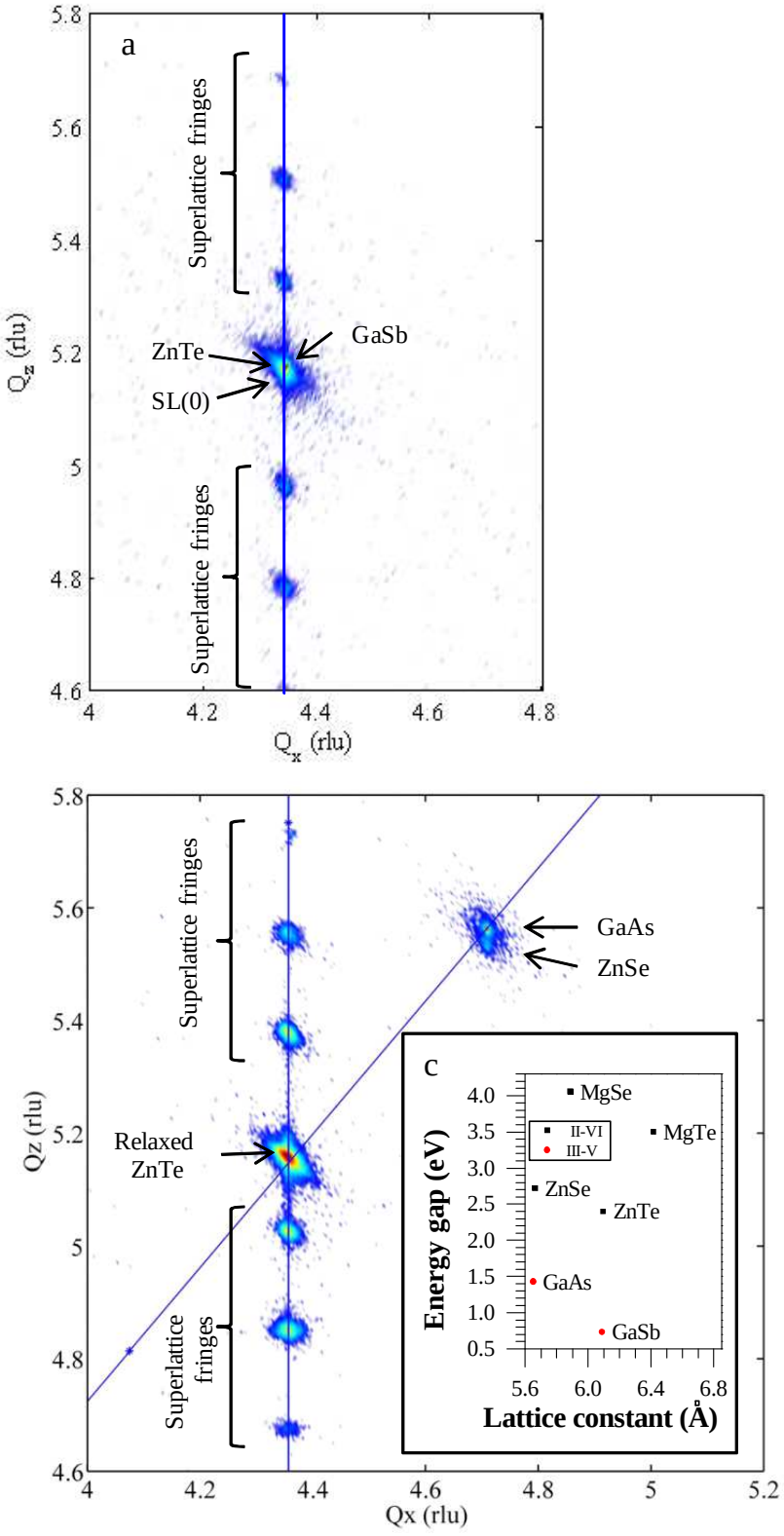

Figure 7.7: HRXRD data of the DBR sample H1 (a) compared to (b) a similar sample grown on GaAs substrate (Graph from [Pacuski *et al.*, 2009]). Both graphs show reciprocal space mapping close to 335 x-ray reflex. Q_x is in layer plane, Q_z is parallel the growth axis, both are in reciprocal lattice unit rlu with a dimension of 1/Å. The line representing relaxed materials crosses the spots of ZnTe and GaAs. In both plots the vertical line connecting the superlattice fringes crosses the spot of ZnTe. This shows that the SL is pseudomorphic to the relaxed ZnTe buffer. (c) Energy gap vs lattice parameter for semiconductors used in this work. Note that refractive index increases, when energy gap of semiconductor decreases.

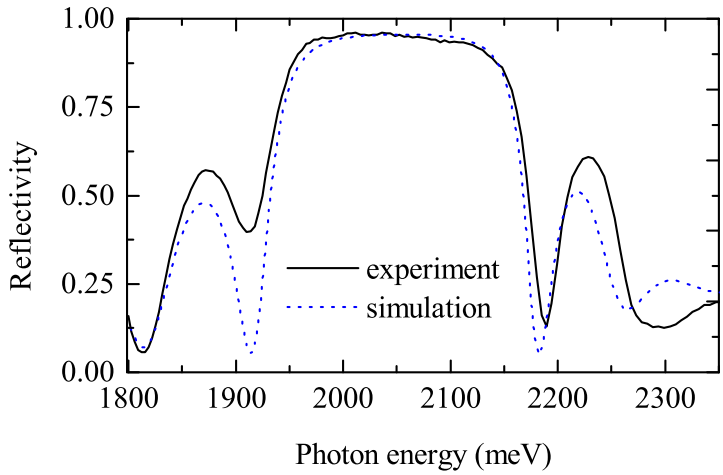

Figure 7.8: Measured and simulated room temperature reflectivity spectrum of the sample H1.

Room temperature reflectivity measurement of the DBR is shown in Fig. 7.8. As designed, it features a stopband in the orange spectral region, centered at around 2050 meV (605 nm). The maximum reflectivity exceeds 95%. The stopband width of over 150 meV is in good agreement with the index difference [Yeh, 1988] of about $\Delta n = 0.5$. The simulation performed with transfer matrix method, with layer thickness and refractive index of the superlattice as adjustment parameters, reproduces well the experimental data.

Concluding, I have presented realization of ZnTe-base DBRs and CdTe/ZnTe QDs on almost lattice-matched substrates. These building blocks of a vertical-cavity surface-emitting laser are expected to facilitate construction of such laser structure for the green-orange spectral region.

Chapter 8

Summary and outlook

In the thesis I have described development and characterization of ZnTe-based microcavities build to control the spontaneous emission of CdTe/ZnTe quantum dots. Such quantum dots are intensively studied in Warsaw and feature many interesting properties. Hovewer, before development of suitable distributed Bragg reflector, effects related to interaction of CdTe/ZnTe quantum dots with cavity electromagnetic field were not investigated. The developmet of the reflector fabrication, followed by design of the first planar and micropillar cavities was the starting point for the presented work.

In the first stage of presented work, basic optical properties of the microcavities were determined. This includes energy and quality factor of the modes, distribution of the electromagnetic field inside micropillars and polarization of the emission. Emission spectroscopy on coupled quantum dot-cavity systems revealed that a single QD emission line, spectrally close to the cavity mode, is responsible for the cavity mode emission. In the same experiment an amplification of the collected QD photoluminescence evidenced the Purcell effect. In a further time-resolved experiment an Purcell-factor above 5 was demonstrated, in agreement with the model simulations.

Having confirmed good optical properties of the ZnTe-based micropillar structures we have developed a new type of micropillar structure in which emission into the undesired continuum of radial decay channels has been successfully suppressed, resulting in decrease of spontaneous emission rate of QDs by factor at least 3. The method, demonstrated for the ZnTe-based system, can be also applied to other material systems.

In the last stage of the work the growth of QDs and DBRs on GaSb substrates was developed. This approach reduces dislocation density, which is an important

step in development of CdTe/ZnTe-based vertical-cavity surface emitting lasers.

8.1 Perspectives

The presented ZnTe-based microcavities constitute a new tool for the research on CdTe/ZnTe quantum dots. It enables amplification of the collected optical response in experiments performed on QDs. Shorter signal aquisition is not only a practical advantage enabling faster experiments, but increasing the signal-to-noise ratio may make doable experiments which would otherwise be impossible.

The developed tool gives new research perspectives for CdTe/ZnTe quantum dots with magnetic ions, which recently featured considerable advance: the use of Cobalt ion as the magnetic impurity was demonstrated. However, QDs with single magnetic ions represent only a small fraction of the ensemble of QDs in a sample. For this reason using currently utilized methods the probability of fabrication of a system featuring QD with a magnetic ion coupled to a micropillar cavity mode is very low. Therefore development of deterministic methods for fabrication of coupled QD-cavity devices is required.

Emission spectroscopy experiments on coupled quantum dot-cavity systems provided valuable information on the properties of micropillars and mechanisms of mode emission. They revealed also a spectral distortion of the observed mode emission - spectral pushing was evidenced when changing the spectral detuning between the emitter and the cavity. Such behavior was also reported for other material systems. The mechanisms behind this distortion are not yet fully understood. Phonons play certainly an important role as they are the major source of cavity mode emission, however, within existing models, the observed large cavity mode ”pushing” still cannot be explained.

The presented method of inhibiting the unwanted ”leaky” emission of QDs in micropillar cavities by radial DBRs is a starting point for further studies. Combined with an enhancement of the spontaneous emission into the guided mode this shows the potential of micropillars with radial DBRs to achieve brightness over 90%. Our study sets thus a new perspective for the construction of a QD-based single photon source reaching ultimate brightness and providing better control of their spontaneous emission. The dark exciton qubit has lifetime much longer than a qubit based on the bright exciton in a QD. Hovewer in-plane radial recombination is its dominant decay channel [Smoleński *et al.*, 2012]. Damping this emission in micropillar with radial DBR opens a way for further increasing the dark excitons lifetime. This give

interesting perspectives for experiments on coherent manipulations of dark exciton qubit.

In the development of vertical-cavity surface emitting laser based on CdTe/ZnTe emitters all the building blocks are ready. However recent efforts of combining these blocks into a functioning device were unsuccessful for reasons that remain unclear, they do not seem to be a major conceptual problem, but rather technical issues. Therefore, it is expected that operation of such laser, optically pumped, will soon be possible.

In a broad overolook on the research on all semiconductor optical microcavities, the wast scope of existing fields gives many possibilities of application of our ZnTe-based system. However, strong coupling between exciton (confined either in QD or quantum well) and cavity mode field is a prerequisite in most of these fields. Therefore improvement of the exciton-photon coupling strenght in the described ZnTe-based QD-cavity system is required, which transtlates mainly to improvement of the quality factor of cavity. Among all those research fields one gains a considerable increase in interest over the recent years. This is the search for non-local coherent coupling between distant emitters, where the radiative coupling by propagating electromagnetic field is intensively explored. Hopefully, experimental work presented here will turn out to be helpful in this new, fascinating field, as well it will bring new perspectives for other, well established fields.

Appendix

8.2 Distortion of observed cavity mode emission

We performed the same experiment as the one described in the previous section on the micropillar A (diameter of 1.4 µm on sample G stemming from the sample S1801) for which we observed the Purcell enhancement described in chapter Purcell effect in quantum dot. To recall: the micropillar was preselected from a group of several tens of micropillars as there was a single QD emission line in the vicinity of its fundamental mode and additionally the system showed very bright emission at resonance with one of the polarizations of the mode. This indicates a good spatial and spectral matching of the QD and cavity mode.

As in the previous section, the properties of the QD - cavity system are extracted by fitting the experimental curves with a sum of two Lorentzian peaks, one for the QD line, the other for the cavity mode (see Fig. 8.1). The line energies are shown as a function of temperature in Fig. 8.2.

With increasing temperature the QD emission line continuously shifts to lower energies, as expected. In contrast, the fitted cavity line when approaching to the resonance with the QD features an anti-crossing-like behavior together with an abrupt jump from low to high energy when crossing the resonance.

We relate the observed mode distortion to effects resulting from the phonon-mediated mode emission [Hohenester *et al.*, 2009; Valente *et al.*, 2014]. As showed by [Hohenester *et al.*, 2009] (see Fig. 5.11) , and confirmed in our experiments, at low temperatures the scattering rate has a dip at zero-detuning. In a simple model the cavity mode emission can be approximated by a product of a Lorentzian (related to its radiative lifetime) and the shape of the scattering rate. Thus, the observed cavity mode - the one we obtain from the fitting procedure described above - appears to be shifted. However, the calculations performed so far [Valente *et al.*, 2014] didn't reproduce the large "pushing" observed in the experiments. We

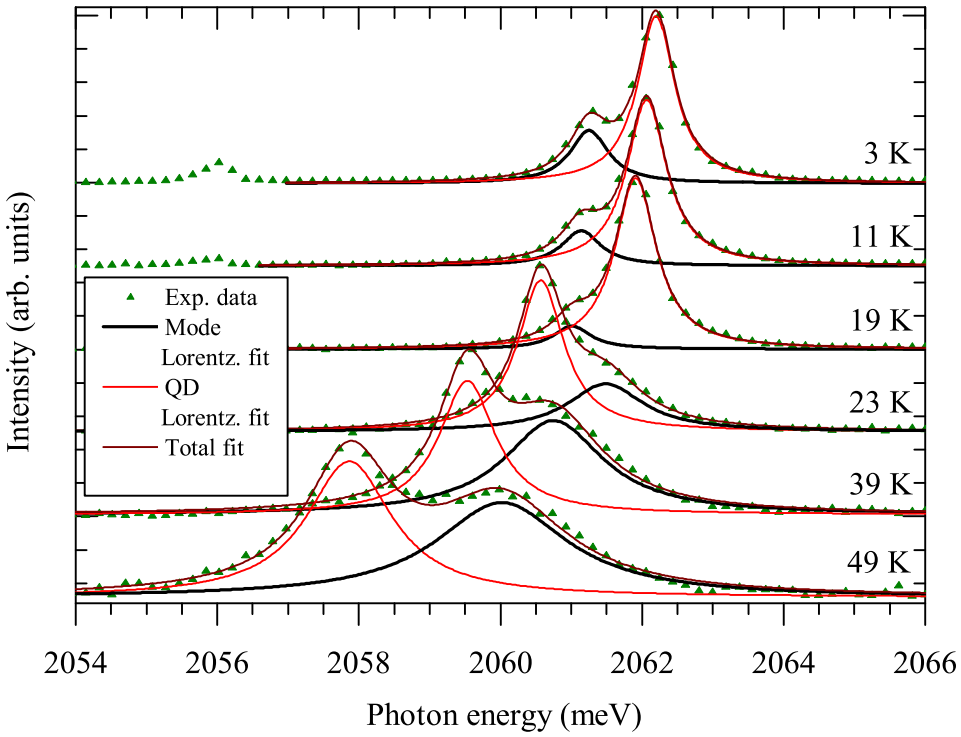

Figure 8.1: Emission spectra for various temperatures.

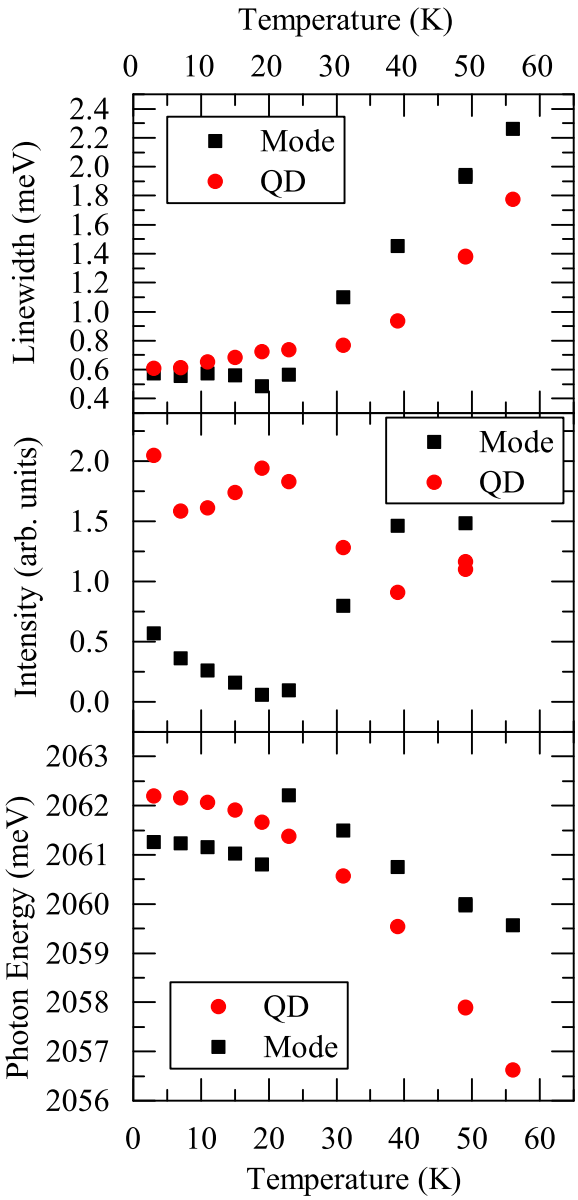

Figure 8.2: Energy of the fitted cavity mode line with respect to the QD line as a function of temperature.

suppose that an additional effect related to phonon energy quantization in QDs may play an important role here.

8.3 Finite-difference time-domain simulation for radially coated micropillar

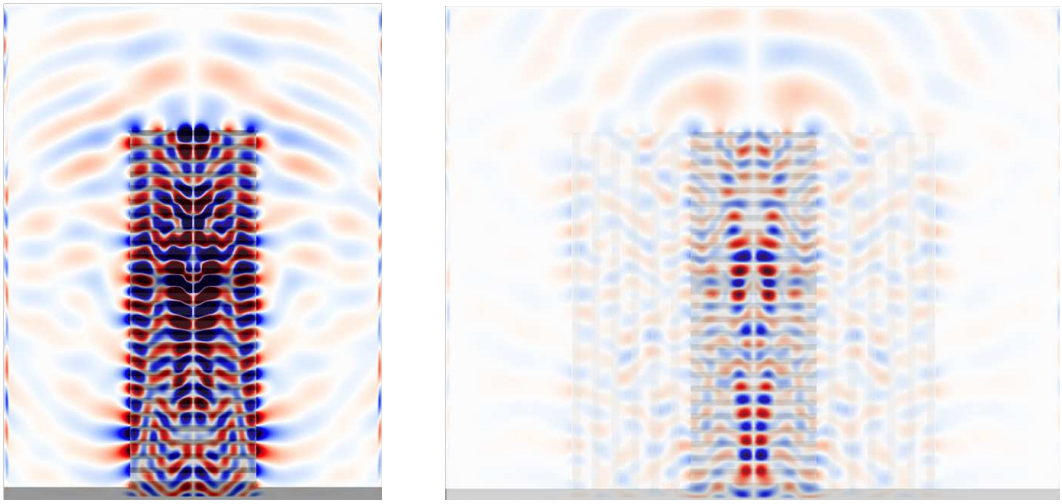

Figure 8.3: Plot of radial component of the electric field in a standard micropillar (left) and coated with a radial DBR (right). Simulation perfrmed using the FDTD method for azimuthal number m = 2.

References

Abram, I., Robert, I. & Kuszelewicz, R. (1998). Spontaneous emission control in semiconductor microcavities with metallic or Bragg mirrors. *Quantum Electronics, IEEE Journal of*, **34**, 71–76. 8

Adachi, M., Yoshizumi, Y., Enya, Y., Kyono, T., Sumitomo, T., Tokuyama, S., Takagi, S., Sumiyoshi, K., Saga, N., Ikegami, T. *et al.* (2010). Low Threshold Current Density InGaN Based 520–530 nm Green Laser Diodes on Semi-Polar 2021 Free-Standing GaN Substrates. *Applied physics express*, **3**, 1001. 21

Adachi, S. (2009). *Properties of semiconductor alloys: group-IV, III-V and II-VI semiconductors*, vol. 28. Wiley. com. 27

Albert, F., Sivalertporn, K., Kasprzak, J., Strauss, M., Schneider, C., Höfling, S., Kamp, M., Forchel, A., Reitzenstein, S., Muljarov, E.A. *et al.* (2013). Microcavity controlled coupling of excitonic qubits. *Nature communications*, **4**, 1747. 10

Alferov, Z.I. (2001). Nobel Lecture: The double heterostructure concept and its applications in physics, electronics, and technology. *Reviews of modern physics*, **73**, 767–782. 12

Amo, A., Lefrère, J., Pigeon, S., Adrados, C., Ciuti, C., Carusotto, I., Houdré, R., Giacobino, E. & Bramati, A. (2009). Superfluidity of polaritons in semiconductor microcavities. *Nature Physics*, **5**, 805–810. 10

André, R., Boeuf, F., Romestain, R., Si Dang, L., Péronne, E., Lampin, J., Hulin, D. & Alexandrou, A. (2000). Mechanisms of polariton stimulation in a microcavity. *Journal of crystal growth*, **214**, 1002–1009. 19

Bayer, M., Reinecke, T.L., Weidner, F., Larionov, A., McDonald, A. & Forchel, A. (2001). Inhibition and Enhancement of the Spontaneous Emission of Quantum Dots in Structured Microresonators. *Phys. Rev. Lett.*, **86**, 3168–3171. 8, 92

Bennett, C. & Brassard, G. (1984). BB84. In *Proc. IEEE International Conference on Computers, Systems, and Signal Processing, IEEE Press, Los Alamitos, Calif*, 175. 11

Bhattacharya, P., Xiao, B., Das, A., Bhowmick, S. & Heo, J. (2013). Solid State Electrically Injected Exciton-Polariton Laser. *Physical Review Letters*, **110**, 206403. 10

Böckler, C., Reitzenstein, S., Kistner, C., Debusmann, R., Löffler, A., Kida, T., Höfling, S., Forchel, A., Grenouillet, L., Claudon, J. & Gérard, J.M. (2008). Electrically driven high-Q quantum dot-micropillar cavities. *Applied Physics Letters*, **92**, 091107. 13, 92, 103

Bogdankevich, O., Zverev, M., Krasilnikov, A. & Pechenov, A. (1967). Laser Emission in Electron-Beam Excited ZnSe. *physica status solidi (b)*, **19**, K5–K6. 22

Bounouar, S., Elouneg-Jamroz, M., Hertog, M.d., Morchutt, C., Bellet-Amalric, E., André, R., Bougerol, C., Genuist, Y., Poizat, J.P., Tatarenko, S. *et al.* (2012). Ultrafast room temperature single-photon source from nanowire-quantum Dots. *Nano letters*, **12**, 2977–2981. 9

Bouwmeester, D., Pan, J.W., Mattle, K., Eibl, M., Weinfurter, H. & Zeilinger, A. (1997). Experimental quantum teleportation. *Nature*, **390**, 575–579. 13

Bouwmeester, D., Ekert, A.K., Zeilinger, A. *et al.* (2000). *The physics of quantum information*, vol. 38. Springer Berlin. 13

Burak, D. & Binder, R. (1997). Cold-cavity vectorial eigenmodes of VCSELs. *IEEE Journal of Quantum Electronics*, **33**, 1205–1215. 63, 75

Carlin, J.F. & Ilegems, M. (2003). High-quality AlInN for high index contrast Bragg mirrors lattice matched to GaN. *Applied physics letters*, **83**, 668–670. 18

Chailertvanitkul, A., Iga, K. & Moriki, K. (1985). GaInAsP/InP surface emitting laser (λ= 1.4 μm, 77 K) with heteromultilayer Bragg reflector. *Electronics Letters*, **21**, 303–304. 6

Christmann, G., Butté, R., Feltin, E., Carlin, J.F. & Grandjean, N. (2006). Impact of inhomogeneous excitonic broadening on the strong exciton-photon coupling in quantum well nitride microcavities. *Physical Review B*, **73**, 153305. 18

Cibert, J., Gobil, Y., Dang, L.S., Tatarenko, S., Feuillet, G., Jouneau, P. & Saminadayar, K. (1990). Critical thickness in epitaxial CdTe/ZnTe. *Applied physics letters*, **56**, 292–294. 42

Claudon, J., Bleuse, J., Malik, N.S., Bazin, M., Jaffrennou, P., Gregersen, N., Sauvan, C., Lalanne, P. & Gerard, J.M. (2010). A highly efficient single-photon source based on a quantum dot in a photonic nanowire. *Nat Photon*, **4**, 174–177. 9

Cohen-Solal, G., Bailly, F. & Barbe, M. (1994). Critical thickness in heteroepitaxial growth of zinc-blende semiconductor compounds. *Journal of crystal growth*, **138**, 68–74. 111

Curran, A., Morrod, J., Prior, K., Kar, A. & Warburton, R. (2007). Exciton–photon coupling in a ZnSe-based microcavity fabricated using epitaxial liftoff. *Semiconductor Science and Technology*, **22**, 1189. 19

Daraei, A., Tahraoui, A., Sanvitto, D., Timpson, J., Fry, P., Hopkinson, M., Guimaraes, P., Vinck, H., Whittaker, D., Skolnick, M. *et al.* (2006). Control of polarized single quantum dot emission in high-quality-factor microcavity pillars. *Applied physics letters*, **88**, 051113–051113. 82, 83

Daum, W. (2002). *POF: polymer optical fibers for data communication*. Springer. 17

Daum, W., Krauser, J., Zamzow, P.E. & Ziemann, O. (2002). Optical Fibers for Data Communication. *Optical Fibers for Data Communication, Springer, Berlin*. 17

Dousse, A., Lanco, L., Suffczyński, J., Semenova, E., Miard, A., Lemaître, A., Sagnes, I., Roblin, C., Bloch, J. & Senellart, P. (2008).

Controlled light-matter coupling for a single quantum dot embedded in a pillar microcavity using far-field optical lithography. *Physical review letters*, **101**, 267404. 13

Dousse, A., Suffczynski, J., Beveratos, A., Krebs, O., Lemaitre, A., Sagnes, I., Bloch, J., Voisin, P. & Senellart, P. (2010). Ultrabright source of entangled photon pairs. *Nature*, **466**, 217–220. 8, 13, 14

Dumont, H., Bourée, J.E., Marbeuf, A. & Gorochov, O. (1993). Photoassisted growth of ZnTe by metalorganic chemical vapour deposition. *Journal of Crystal Growth*, **130**, 600 – 610. 106

Fan, J., Ouyang, L., Liu, X., Ding, D., Furdyna, J., Smith, D. & Zhang, Y.H. (2011). Growth and material properties of ZnTe on GaAs, InP, InAs and GaSb substrates for electronic and optoelectronic device applications. *Journal of Crystal Growth*, **323**, 127 – 131. 105, 106, 108, 109

Faraon, A., Barclay, P.E., Santori, C., Fu, K.M.C. & Beausoleil, R.G. (2011). Resonant enhancement of the zero-phonon emission from a colour centre in a diamond cavity. *Nature Photonics*, **5**, 301–305. 2

Gaines, J., Petruzzello, J. & Greenberg, B. (1993). Structural properties of ZnSe films grown by migration enhanced epitaxy. *Journal of applied physics*, **73**, 2835–2840. 108

Gayral, B. & Gérard, J.M. (2008). Photoluminescence experiment on quantum dots embedded in a large Purcell-factor microcavity. *Phys. Rev. B*, **78**, 235306. 64

Gayral, B., Gerard, J., Legrand, B., Costard, E. & Thierry-Mieg, V. (1998). Optical study of GaAs/AlAs pillar microcavities with elliptical cross section. *Applied physics letters*, **72**, 1421–1423. 67, 70

Gayral, B., Gérard, J., Lemaitre, A., Dupuis, C., Manin, L. & Pelouard, J. (1999). High-Q wet-etched GaAs microdisks containing InAs quantum boxes. *Applied physics letters*, **75**, 1908–1910. 7

Gazzano, ., de Vasconcellos, S.M., Arnold, C., Nowak, A., Galopin, E., Sagnes, I., Lanco, L., Lemaitre, A. & Senellart, P. (2013a). Bright solid-state sources of indistinguishable single photons. *Nat Commun*, **4**, 1425. 5, 14, 92

Gazzano, O., de Vasconcellos, S.M., Gauthron, K., Symonds, C., Bloch, J., Voisin, P., Bellessa, J., Lemaître, A. & Senellart, P. (2011). Evidence for confined Tamm plasmon modes under metallic microdisks and application to the control of spontaneous optical emission. *Physical Review Letters*, **107**, 247402. 8

Gazzano, O., Almeida, M., Nowak, A., Portalupi, S., Lemaître, A., Sagnes, I., White, A. & Senellart, P. (2013b). Entangling Quantum-Logic Gate Operated with an Ultrabright Semiconductor Single-Photon Source. *Physical Review Letters*, **110**, 250501. 13

Gérard, J.M., Barrier, D., Marzin, J.Y., Kuszelewicz, R., Manin, L., Costard, E., Thierry-Mieg, V. & Rivera, T. (1996). Quantum boxes as active probes for photonic microstructures: The pillar microcavity case. *Applied Physics Letters*, **69**, 449–451. 7, 60

Gérard, J.M., Sermage, B., Gayral, B., Legrand, B., Costard, E. & Thierry-Mieg, V. (1998). Enhanced Spontaneous Emission by Quantum Boxes in a Monolithic Optical Microcavity. *Phys. Rev. Lett.*, **81**, 1110–1113. 4, 8, 75, 82, 92

Guo, Y., Aizin, G., Chen, Y., Zeng, L., Cavus, A. & Tamargo, M.C. (1997). Photo-pumped ZnCdSe/ZnCdMgSe blue-green quantum well lasers grown on InP substrates. *Applied physics letters*, **70**, 1351–1353. 22

Gutbrod, T., Bayer, M., Forchel, A., Knipp, P., Reinecke, T., Tartakovskii, A., Kulakovskii, V., Gippius, N. & Tikhodeev, S. (1999). Angle dependence of the spontaneous emission from confined optical modes in photonic dots. *Physical Review B*, **59**, 2223. 73

Haase, M., Qiu, J., DePuydt, J. & Cheng, H. (1991). Blue-green laser diodes. *Applied Physics Letters*, **59**, 1272. 20

Hayashi, H., Saitou, T., Maruyama, N., Inaba, H., Kawamura, K. & Mori, M. (2005). Thermal expansion coefficient of yttria stabilized zirconia for various yttria contents. *Solid State Ionics*, **176**, 613–619. 27

Henini, M. (2012). *Molecular Beam Epitaxy: From Research to Mass Production*. Newnes. 34

Hennessy, K., Badolato, A., Winger, M., Gerace, D., Atature, M., Gulde, S., Falt, S., Hu, E.L. & Imamoglu, A. (2007). Quantum nature of a strongly coupled single quantum dot-cavity system. *Nature*, **445**, 896–899. 10, 84

Herve, D., Accomo, R., Molva, E., Vanzetti, L., Paggel, J., Sorba, L. & Franciosi, A. (1995). Microgun-pumped blue lasers. *Applied physics letters*, **67**, 2144–2146. 22

Ho, Y.L., Cao, T., Ivanov, P.S., Cryan, M.J., Craddock, I.J., Railton, C.J. & Rarity, J.G. (2007). Three-dimensional FDTD simulation of micropillar microcavity geometries suitable for efficient single-photon sources. *Quantum Electronics, IEEE Journal of*, **43**, 462–472. 92

Hohenester, U., Laucht, A., Kaniber, M., Hauke, N., Neumann, A., Mohtashami, A., Seliger, M., Bichler, M. & Finley, J.J. (2009). Phonon-assisted transitions from quantum dot excitons to cavity photons. *Phys. Rev. B*, **80**, 201311. 79, 87, 88, 102, 121

Hovinen, M., Ding, J., Salokatve, A., Nurmikko, A., Hua, G., Grillo, D., He, L., Han, J., Ringle, M. & Gunshor, R. (1995). On degradation of ZnSe-based blue-green diode lasers. *Journal of Applied Physics*, **77**, 4150. 21

Hulet, R.G., Hilfer, E.S. & Kleppner, D. (1985). Inhibited spontaneous emission by a Rydberg atom. *Physical review letters*, **55**, 2137–2140. 8

Itoh, S., Nakano, K. & Ishibashi, A. (2000). Current status and future prospects of ZnSe-based light-emitting devices. *journal of crystal growth*, **214**, 1029–1034. 21

Jakubczyk, T. (2009). Influence of photonic environment on spontaneous light emission from quantum dot. *Master thesis*. 57

Jakubczyk, T., Kazimierczuk, T., Golnik, A., Bienias, P., Pacuski, W., Kruse, C., Hommel, D., Klopotowski, L., Wojtowicz, T. & Gaj, J.A. (2009). Optical Study of ZnTe-based 2D and 0D Photonic Structures containing CdTe/ZnTe Quantum Dots. *Acta Physica Polonica A*, **116**, 888–889. 24

Jakubczyk, T., Pacuski, W., Duch, P., Godlewski, P., Golnik, A., Kruse, C., Hommel, D. & Gaj, J. (2011). Far field emission of micropillar and planar

microcavities lattice-matched to ZnTe. *Central European Journal of Physics*, **9**, 428–431, 10.2478/s11534-010-0131-8. 87, 105

Jakubczyk, T., Pacuski, W., Smoleński, T., Golnik, A., Florian, M., Jahnke, F., Kruse, C., Hommel, D. & Kossacki, P. (2012). Pronounced Purcell enhancement of spontaneous emission in CdTe/ZnTe quantum dots embedded in micropillar cavities. *Applied Physics Letters*, **101**, 132105. 75, 92, 101, 102

Jewell, J., Lee, Y., Walker, S., Scherer, A., Harbison, J., Florez, L. & McCall, S. (1989). Low-threshold electrically pumped vertical-cavity surface-emitting microlasers. *Electronics Letters*, **25**, 1123. 7

Kamuro, S., Hamaguchi, C., Fukushima, M. & Nakai, J. (1971). Electrical and optical properties of ZnTe-GaSb heterojunctions. *Solid-State Electronics*, **14**, 1183 – 1192. 106

Kaniber, M., Laucht, A., Neumann, A., Villas-Bôas, J., Bichler, M., Amann, M.C. & Finley, J. (2008). Investigation of the nonresonant dot-cavity coupling in two-dimensional photonic crystal nanocavities. *Physical Review B*, **77**, 161303. 84

Karczewski, G., Maćkowski, S., Kutrowski, M., Wojtowicz, T. & Kossut, J. (1999). Photoluminescence study of CdTe/ZnTe self-assembled quantum dots. *Appl. Phys. Lett.*, **74**, 3011–3013. 17

Kasprzak, J., Richard, M., Kundermann, S., Baas, A., Jeambrun, P., Keeling, J.M.J., Marchetti, F.M., Szymanska, M.H., Andre, R., Staehli, J.L., Savona, V., Littlewood, P.B., Deveaud, B. & Dang, L.S. (2006). Bose-Einstein condensation of exciton polaritons. *Nature*, **443**, 409–414. 10, 19

Kasprzak, J., Reitzenstein, S., Muljarov, E., Kistner, C., Schneider, C., Strauss, M., Höfling, S., Forchel, A. & Langbein, W. (2010). Up on the Jaynes-Cummings ladder of a quantum-dot/microcavity system. *Nature materials*, **9**, 304–308. 10

Kato, E., Noguchi, H., Nagai, M., Okuyama, H., Kijima, S. & Ishibashi, A. (1998). Significant progress in Il-VI blue-green laser diode lifetime. *Electronics Letters*, **34**, 282–284. 20

Kato, N., Kohno, Y. & Saka, H. (1999). Side-wall damage in a transmission electron microscopy specimen of crystalline Si prepared by focused ion beam etching. *Journal of Vacuum Science & Technology A: Vacuum, Surfaces, and Films*, **17**, 1201–1204. 40, 41

Kazimierczuk, T. (2013). personal communication. 52

Kazimierczuk, T., Goryca, M., Koperski, M., Golnik, A., Gaj, J.A., Nawrocki, M., Wojnar, P. & Kossacki, P. (2010). Picosecond charge variation of quantum dots under pulsed excitation. *Phys. Rev. B*, **81**, 155313. 78, 82, 101, 102

Kelkar, P., Kozlov, V., Jeon, H., Nurmikko, A., Chu, C.C., Grillo, D., Han, J., Hua, C.G. & Gunshor, R. (1995). Excitons in a II-VI semiconductor microcavity in the strong-coupling regime. *Physical Review B*, **52**, R5491. 19

Khitrova, G., Gibbs, H., Kira, M., Koch, S. & Scherer, A. (2006). Vacuum Rabi splitting in semiconductors. *Nature Physics*, **2**, 81–90. 6

Kimerling, L. (1978). Recombination enhanced defect reactions. *Solid-State Electronics*, **21**, 1391–1401. 21

Kiraz, A., Michler, P., Becher, C., Gayral, B., Imamoglu, A., Zhang, L., Hu, E., Schoenfeld, W.V. & Petroff, P.M. (2001). Cavity-quantum electrodynamics using a single InAs quantum dot in a microdisk structure. *Applied Physics Letters*, **78**, 3932–3934. 85

Klein, T., Klembt, S. & Kruse, C. (2014). personal communication. 22

Kleppner, D. *et al.* (1981). Inhibited spontaneous emission. *Physical Review Letters*, **47**, 233–236. 4

Kobak, J., Pacuski, W., Jakubczyk, T., Kazimierczuk, T., Golnik, A., Frank, K., Rosenauer, A., Kruse, C., Hommel, D. & Gaj, J. (2011). Optical Properties of CdTe QDs Formed Using Zn Induced Reorganization. *Acta Physica Polonica A*, **119**, 627–629. 90

Kobak, J., Rousset, J.G., Rudniewski, R., Janik, E., Slupinski, T., Kossacki, P., Golnik, A. & Pacuski, W. (2013). Ultra low density of CdTe quantum dots grown by {MBE}. *Journal of Crystal Growth*, **378**, 274 – 277. 17

Krames, M.R., Shchekin, O.B., Mueller-Mach, R., Mueller, G.O., Zhou, L., Harbers, G. & Craford, M.G. (2007). Status and future of high-power light-emitting diodes for solid-state lighting. *Display Technology, Journal of*, **3**, 160–175. 18

Kruse, C., Alexe, G., Klude, M., Heinke, H. & Hommel, D. (2002). High Reflectivity p-Type Doped Distributed Bragg Reflectors Using ZnSe/MgS Superlatticesgreen monolithic II-VI vertical-cavity surface-emitting laser operating at room temperature. *phys. stat. sol. (b)*, **229**, 111. 19

Kruse, C., Ulrich, S.M., Alexe, G., Roventa, E., Krüger, R., Brendemühl, B., Michler, P., Gutowski, J. & Hommel, D. (2004). Green monolithic II-VI vertical-cavity surface-emitting laser operating at room temperature. *phys. stat. sol. (b)*, **241**, 731. 24

Kruse, C., Gartner, M., Gust, A. & Hommel, D. (2007). In situ observation of Zn-induced etching during CdSe quantum dot formation using time-resolved ellipsometry. *Appl. Phys. Lett.*, **90**, 221102. 43

Kruse, C., Lohmeyer, H., Sebald, K., Gutowski, J., Hommel, D., Wiersig, J. & Jahnke, F. (2008). Green laser emission from monolithic II-VI-based pillar microcavities near room temperature. *Applied Physics Letters*, **92**, 031101–031101–3. 19, 23

Kruse, C., Pacuski, W., Jakubczyk, T., Kobak, J., Gaj, J.A., Frank, K., Schowalter, M., Rosenauer, A., Florian, M., Jahnke, F. & Hommel, D. (2011). Monolithic ZnTe-based pillar microcavities containing CdTe quantum dots. *Nanotechnology*, **22**, 285204. 20, 23, 24, 43, 44, 45, 107

Kulakovskii, V., Bacher, G., Weigand, R., Kümmell, T., Forchel, A., Borovitskaya, E., Leonardi, K. & Hommel, D. (1999). Fine structure of biexciton emission in symmetric and asymmetric CdSe/ZnSe single quantum dots. *Physical Review Letters*, **82**, 1780. 83

Lagoudakis, K.G., Wouters, M., Richard, M., Baas, A., Carusotto, I., André, R., Dang, L.S., Deveaud-Plédran, B. *et al.* (2008). Quantized vortices in an exciton–polariton condensate. *Nature Physics*, **4**, 706–710. 10

Lalanne, P., Hugonin, J.P. & Gérard, J.M. (2004). Electromagnetic study of the quality factor of pillar microcavities in the small diameter limit. *Applied physics letters*, **84**, 4726–4728. 15, 64

Laucht, A., Hauke, N., Neumann, A., Gunthner, T., Hofbauer, F., Mohtashami, A., Muller, K., Bohm, G., Bichler, M., Amann, M.C. *et al.* (2011). Nonresonant feeding of photonic crystal nanocavity modes by quantum dots. *Journal of Applied Physics*, **109**, 102404–102404. 60, 85

Lecamp, G., Hugonin, J., Lalanne, P., Braive, R., Varoutsis, S., Laurent, S., Lemaître, A., Sagnes, I., Patriarche, G., Robert-Philip, I. *et al.* (2007). Submicron-diameter semiconductor pillar microcavities with very high quality factors. *Applied Physics Letters*, **90**, 091120–091120. 15

Lee, E., Ell, C., Brick, P., Spiegelberg, C., Gibbs, H., Khitrova, G., Deppe, D. & Huffaker, D. (2001). Saturation of normal-mode coupling in aluminum-oxide-aperture semiconductor nanocavities. *Journal of Applied Physics*, **89**, 807–809. 10

Lee, Y.S. & Lin, S.D. (2014). Polarized emission of quantum dots in microcavity and anisotropic Purcell factors. *Optics Express*, **22**, 1512–1523. 82

Leiderer, H., Jahn, G., Silberbauer, M., Kuhn, W., Wagner, H.P., Limmer, W. & Gebhardt, W. (1991). Investigation of strain in metalorganic vapor-phase epitaxy grown ZnTe layers by optical methods. *Journal of Applied Physics*, **70**, 398–404. 106

Lermer, M., Gregersen, N., Dunzer, F., Reitzenstein, S., Höfling, S., Mørk, J., Worschech, L., Kamp, M. & Forchel, A. (2012). Bloch-Wave Engineering of Quantum Dot Micropillars for Cavity Quantum Electrodynamics Experiments. *Phys. Rev. Lett.*, **108**, 057402. 16, 103

Liu, Z., Hawkins, B. & Kuech, T. (2003). Chemical and structural characterization of GaSb(100) surfaces treated by HCl-based solutions and annealed in vacuum. *Journal of Vacuum Science Technology B: Microelectronics and Nanometer Structures*, **21**, 71–77. 106, 107

Lodahl, P., Van Driel, A.F., Nikolaev, I.S., Irman, A., Overgaag, K., Vanmaekelbergh, D. & Vos, W.L. (2004). Controlling the dynamics of spon-

taneous emission from quantum dots by photonic crystals. *Nature*, **430**, 654–657. 8

Loffler, A., Reithmaier, J., Sek, G., Hofmann, C., Reitzenstein, S., Kamp, M. & Forchel, A. (2005). Semiconductor quantum dot microcavity pillars with high-quality factors and enlarged dot dimensions. *Applied Physics Letters*, **86**, 111105–111105. 40

Lohmeyer, H., Kruse, C., Sebald, K., Gutowski, J. & Hommel, D. (2006a). Enhanced spontaneous emission of CdSe quantum dots in monolithic II-VI pillar microcavities. *Applied Physics Letters*, **89**, 091107. 8, 24, 92

Lohmeyer, H., Sebald, K., Kruse, C., Kroger, R., Gutowski, J., Hommel, D., Wiersig, J., Baer, N. & Jahnke, F. (2006b). Confined optical modes in monolithic II-VI pillar microcavities. *Applied Physics Letters*, **88**, 051101–051101–3. 19, 60

Lohmeyer, H., Kalden, J., Sebald, K., Kruse, C., Hommel, D. & Gutowski, J. (2008). Fine tuning of quantum-dot pillar microcavities by focused ion beam milling. *Applied Physics Letters*, **92**, 011116–011116–3. 19

Marple, D. (1963). Effective electron mass in CdTe. *Physical Review*, **129**, 2466. 29

Marple, D.T.F. (1964). Refractive Index of ZnSe, ZnTe, and CdTe. *J. Appl. Phys.*, **35**, 539–542. 20, 25, 45, 63, 68, 75

Michler, P., Kiraz, A., Zhang, L., Becher, C., Hu, E. & Imamoglu, A. (2000). Laser emission from quantum dots in microdisk structures. *Applied Physics Letters*, **77**, 184–186. 7

Mueller-Mach, R., Mueller, G.O., Krames, M.R., Shchekin, O.B., Schmidt, P.J., Bechtel, H., Chen, C.H. & Steigelmann, O. (2009a). All-nitride monochromatic amber-emitting phosphor-converted light-emitting diodes. *physica status solidi (RRL)-Rapid Research Letters*, **3**, 215–217. 17

Mueller-Mach, R., Mueller, G.O., Krames, M.R., Shchekin, O.B., Schmidt, P.J., Bechtel, H., Chen, C.H. & Steigelmann, O. (2009b). All-nitride monochromatic amber-emitting phosphor-converted light-emitting diodes. *physica status solidi (RRL)-Rapid Research Letters*, **3**, 215–217. 18

Munsch, M., Mosset, A., Auffèves, A., Seidelin, S., Poizat, J.P., Gérard, J.M., Lemaitre, A., Sagnes, I. & Senellart, P. (2009). Continuous-wave versus time-resolved measurements of Purcell factors for quantum dots in semiconductor microcavities. *Phys. Rev. B*, **80**, 115312. 77, 102

Munsch, M., Malik, N.S., Dupuy, E., Delga, A., Bleuse, J., Gérard, J.M., Claudon, J., Gregersen, N. & Mørk, J. (2013). Dielectric GaAs Antenna Ensuring an Efficient Broadband Coupling between an InAs Quantum Dot and a Gaussian Optical Beam. *Physical review letters*, **110**, 177402. 9

Naesby, A., Suhr, T., Kristensen, P.T. & Mørk, J. (2008). Influence of pure dephasing on emission spectra from single photon sources. *Phys. Rev. A*, **78**, 045802. 87

Nakamura, S., Senoh, M., Nagahama, S.i., Iwasa, N., Yamada, T., Matsushita, T., Kiyoku, H., Sugimoto, Y., Kozaki, T., Umemoto, H. *et al.* (1998). InGaN/GaN/AlGaN-based laser diodes with modulation-doped strained-layer superlattices grown on an epitaxially laterally overgrown GaN substrate. *Applied Physics Letters*, **72**, 211–213. 20

N.Betancort (2001). Fresnel Diffraction Applet, Ver. 2.7. *Numerical simulation programme*. 73

Nesbit, R. (1967). Operation for correction of distal penile ventral curvature with or without hypospadias. *The Journal of urology*, **97**, 720. 98

Nomura, I., Ochiai, Y., Toyomura, N., Manoshiro, A., Kikuchi, A. & Kishino, K. (2004). Characterization of ZnCdSeTe/MgZnSeTe materials for ZnTe-based visible optical devices. *phys. stat. sol. (b)*, **241**, 483. 19, 45, 105

Nomura, I., Manoshiro, A., Kikuchi, A. & Kishino, K. (2006a). Yellow-green lasing operations of ZnCdTe/MgZnSeTe laser diodes on ZnTe substrates. *phys. stat. sol. (b)*, **243**, 955. 105

Nomura, I., Kishino, K., Ebisawa, T., Sawafuji, Y., Ujihara, R., Tasai, K., Nakamura, H., Asatsuma, T. & Nakajima, H. (2009). Photopumped green lasing on BeZnSeTe double heterostructures grown on InP substrates. *Applied Physics Letters*, **94**, 021104–021104. 22

Nomura, I., Sawafuji, Y. & Kishino, K. (2011). Photopumped Lasing Characteristics in Green-to-Yellow Range for BeZnSeTe II–VI Compound Quaternary

Double Heterostructures Grown on InP Substrates. *Japanese Journal of Applied Physics*, **50**, 1201. 23

Nomura, M., Iwamoto, S., Watanabe, K., Kumagai, N., Nakata, Y., Ishida, S. & Arakawa, Y. (2006b). Room temperature continuous-wave lasing in photonic crystal nanocavity. *Opt. Express*, **14**, 6308–6315. 17

Pacuski, W., Kruse, C., Figge, S. & Hommel, D. (2009). High-reflectivity broadband distributed Bragg reflector lattice matched to ZnTe. *Applied Physics Letters*, **94**, 191108. 20, 23, 24, 45, 63, 67, 75, 90, 111, 114

Passow, T., Leonardi, K., Heinke, H., Hommel, D., Litvinov, D., Rosenauer, A., Gerthsen, D., Seufert, J., Bacher, G. & Forchel, A. (2002). Quantum dot formation by segregation enhanced CdSe reorganization. *Journal of applied physics*, **92**, 6546–6552. 43

Pawlis, A., Khartchenko, A., Husberg, O., As, D.J., Lischka, K. & Schikora, D. (2003). Large room temperature Rabi-splitting in II–VI semiconductor microcavity quantum structures. *Microelectronics journal*, **34**, 439–442. 19

Pelton, M., Santori, C., Vuc̆ković, J., Zhang, B., Solomon, G.S., Plant, J. & Yamamoto, Y. (2002). Efficient Source of Single Photons: A Single Quantum Dot in a Micropost Microcavity. *Phys. Rev. Lett.*, **89**, 233602. 8, 11

Pimpinella, R., Liu, X., Furdyna, J., Dobrowolska, M., Mintairov, A. & Merz, J. (2010). Self-Assembled CdTe Quantum Dots Grown on ZnTe/GaSb. *Journal of Electronic Materials*, **39**, 992–995. 106

Pimpinella, R.E., Mintairov, A.M., Liu, X., Kosel, T.H., Merz, J.L., Furdyna, J.K. & Dobrowolska, M. (2011). Optical measurements of single CdTe self-assembled quantum dots grown on ZnTe/GaSb. vol. 29, 03C119, AVS. 17, 106

Poborchii, V., Tada, T., Kanayama, T. & Moroz, A. (2003). Silver-coated silicon pillar photonic crystals: Enhancement of a photonic band gap. *Applied Physics Letters*, **82**, 508–510. 8, 92

Poem, E., Kodriano, Y., Tradonsky, C., Lindner, N., Gerardot, B., Petroff, P. & Gershoni, D. (2010). Accessing the dark exciton with light. *Nature physics*, **6**, 993–997. 103

Press, D., Götzinger, S., Reitzenstein, S., Hofmann, C., Löffler, A., Kamp, M., Forchel, A. & Yamamoto, Y. (2007). Photon antibunching from a single quantum-dot-microcavity system in the strong coupling regime. *Physical review letters*, **98**, 117402. 84

Purcell, E.M. (1946). Spontaneous emission probabilities at radio frequencies. *Physical Review*, **69**, 681–681. 1, 3, 6

Rabe, M., Lowisch, M. & Henneberger, F. (1998). Self-assembled CdSe quantum dots Formation by thermally activated surface reorganization. *Journal of crystal growth*, **184**, 248–253. 43

Rajakarunanayake, Y., Cole, B.H., McCaldin, J.O., Chow, D., Soderstrom, J., McGill, T. & Jones, C.M. (1989). Growth and characterization of ZnTe films grown on GaAs, InAs, GaSb, and ZnTe. *Applied Physics Letters*, **55**, 1217–1219. 106

Reithmaier, J.P., Sek, G., Löffler, A., Hofmann, C., Kuhn, S., Reitzenstein, S., Keldysh, L.V., Kulakovskii, V.D., Reinecke, T.L. & Forchel, A. (2004). Strong coupling in a single quantum dot-semiconductor microcavity system. *Nature*, **432**, 197 – 200. 10

Reitzenstein, S. & Forchel, A. (2010). Quantum dot micropillars. *Journal of Physics D: Applied Physics*, **43**, 033001. 13, 15

Reitzenstein, S., Bazhenov, A., Gorbunov, A., Hofmann, C., Münch, S., Löffler, A., Kamp, M., Reithmaier, J.P., Kulakovskii, V.D. & Forchel, A. (2006). Lasing in high-Q quantum-dot micropillar cavities. *Applied Physics Letters*, **89**, 051107. 13

Reitzenstein, S., Hofmann, C., Gorbunov, A., Strauss, M., Kwon, S., Schneider, C., Löffler, A., Höfling, S., Kamp, M. & Forchel, A. (2007). AlAs/ GaAs micropillar cavities with quality factors exceeding 150.000. *Applied physics letters*, **90**, 251109. 13, 15, 40

Rigneault, H., Broudic, J., Gayral, B. & Gérard, J.M. (2001). Far-field radiation from quantum boxes located in pillar microcavities. *Opt. Lett.*, **26**, 1595–1597. 87

Rivera, T., Debray, J.P., Gérard, J., Legrand, B., Manin-Ferlazzo, L. & Oudar, J. (1999). Optical losses in plasma-etched AlGaAs microresonators using reflection spectroscopy. *Applied physics letters*, **74**, 911–913. 14

Robin, I.C., André, R., Balocchi, A., Carayon, S., Moehl, S., Gérard, J.M. & Ferlazzo, L. (2005). Purcell effect for CdSe/ZnSe quantum dots placed into hybrid micropillars. *Applied Physics Letters*, **87**, 233114. 24

Rubanov, S. & Munroe, P. (2005). Damage in III–V Compounds during Focused Ion Beam Milling. *Microscopy and Microanalysis*, **11**, 446–455. 41

Santori, C., Fattal, D., Vuckovic, J., Solomon, G.S. & Yamamoto, Y. (2002). Indistinguishable photons from a single-photon device. *Nature*, **419**, 594. 13

Schmidt-Grund, R., Hilmer, H., Hinkel, A., Sturm, C., Rheinländer, B., Gottschalch, V., Lange, M., Zuniga-Pérez, J. & Grundmann, M. (2010). Two-dimensional confined photonic wire resonators – strong light–matter coupling. *physica status solidi (b)*, **247**, 1351–1364. 92, 94, 95

Schneider, C., Rahimi-Iman, A., Kim, N.Y., Fischer, J., Savenko, I.G., Amthor, M., Lermer, M., Wolf, A., Worschech, L., Kulakovskii, V.D. *et al.* (2013). An electrically pumped polariton laser. *Nature*, **497**, 348–352. 10

Schubert, E. (2006). *Light-Emitting Diodes*. Cambridge University Press. 14

Schuster, M. & Herres, T. (1993). An Introduction to High-Resolution X-Ray Diffractometry. *In: Proceedings "Herbstschule Röntgenoptik" (ed. H.-R. Höche)*, 69–119. 37, 38

Ściesiek, M., Gietka, K., Golnik, A., Kossacki, P., Jakubczyk, T., Pacuski, W., Kruse, C. & Hommel, D. (2011). Toward Better Light-Confinement in Micropillar Cavities. *Acta Phys. Pol. A*, **120**, 877–879. 82, 98, 105

Sebald, K., Michler, P., Passow, T., Hommel, D., Bacher, G. & Forchel, A. (2002). Single-photon emission of CdSe quantum dots at temperatures up to 200 K. *Applied Physics Letters*, **81**, 2920–2922. 16

Sebald, K., Kruse, C. & Wiersig, J. (2009). Properties and prospects of blue-green emitting II-VI-based monolithic microcavities. *physica status solidi (b)*, **246**, 255–271. 19

Sebald, K., Seyfried, M., Kalden, J., Gutowski, J., Dartsch, H., Tessarek, C., Aschenbrenner, T., Figge, S., Kruse, C., Hommel, D. *et al.* (2010). Optical properties of InGaN quantum dots in monolithic pillar microcavities. *Applied Physics Letters*, **96**, 251906–251906. 18

Smoleński, T., Kazimierczuk, T., Goryca, M., Kossacki, P., Gaj, J.A., Wojnar, P., Fronc, K., Korkusinski, M. & Hawrylak, P. (2011). Influence of Configuration Mixing on Energies and Recombination Dynamics of Excitonic States in CdTe/ZnTe Quantum Dots. *Acta Phys. Pol. A*, **119**. 78

Smoleński, T., Kazimierczuk, T., Goryca, M., Jakubczyk, T., Wojnar, P., Golnik, A., Kossacki, P. *et al.* (2012). In-plane radiative recombination channel of a dark exciton in self-assembled quantum dots. *Physical Review B*, **86**, 241305. 103, 118

Snitzer, E. (1961). Cylindrical dielectric waveguide modes. *JOSA*, **51**, 491–498. 71

Soda, H., Iga, K.i., Kitahara, C. & Suematsu, Y. (1979). GaInAsP/InP surface emitting injection lasers. *Japanese Journal of Applied Physics*, **18**, 2329. 6

Srinivasan, K., Barclay, P.E., Painter, O., Chen, J., Cho, A.Y. & Gmachl, C. (2003). Experimental demonstration of a high quality factor photonic crystal microcavity. *Applied Physics Letters*, **83**, 1915–1917. 7

Stevenson, R., Thompson, R., Shields, A., Farrer, I., Kardynal, B., Ritchie, D. & Pepper, M. (2002). Quantum dots as a photon source for passive quantum key encoding. *Physical Review B*, **66**, 081302. 83

Strauf, S. & Jahnke, F. (2011). Single quantum dot nanolaser. *Laser & Photonics Reviews*, **5**, 607–633. 12

Strauf, S., Hennessy, K., Rakher, M.T., Choi, Y.S., Badolato, A., Andreani, L.C., Hu, E.L., Petroff, P.M. & Bouwmeester, D. (2006). Self-Tuned Quantum Dot Gain in Photonic Crystal Lasers. *Phys. Rev. Lett.*, **96**, 127404. 12

Sturm, C., Hilmer, H., Schmidt-Grund, R., Czekalla, C., Sellmann, J., Lenzner, J., Lorenz, M. & Grundmann, M. (2009). Strong exciton-photon coupling in ZnO based resonators. vol. 27, 1726–1730, AVS. 92

Suffczyński, J., Dousse, A., Gauthron, K., Lemaître, A., Sagnes, I., Lanco, L., Bloch, J., Voisin, P. & Senellart, P. (2009). Origin of the Optical Emission within the Cavity Mode of Coupled Quantum Dot-Cavity Systems. *Phys. Rev. Lett.*, **103**, 027401. 84, 87

Tanaka, K., Nakamura, T., Takamatsu, W., Yamanishi, M., Lee, Y. & Ishihara, T. (1995). Cavity-induced changes of spontaneous emission lifetime in one-dimensional semiconductor microcavities. *Physical review letters*, **74**, 3380. 8

Thomas, O., Yuan, Z., Dynes, J., Sharpe, A. & Shields, A. (2010). Efficient photon number detection with silicon avalanche photodiodes. *Applied Physics Letters*, **97**, 031102. 23

Tinjod, F., Gilles, B., Moehl, S., Kheng, K. & Mariette, H. (2003). II–VI quantum dot formation induced by surface energy change of a strained layer. *Appl. Phys. Lett.*, **82**, 4340–4342. 29, 43

Tinjod, F., Moehl, S., Kheng, K., Gilles, B. & Mariette, H. (2004). CdTe/Zn[sub 1 - x]Mg[sub x]Te self-assembled quantum dots: Towards room temperature emission. *Journal of Applied Physics*, **95**, 102–108. 17

Tomasini, P., Haidoux, A., Domagala, J., Tedenac, J., Maurin, M. & Ducourant, B. (1996). Growth by atmospheric pressure OMVPE and X-ray analysis of ZnTe epilayers on III–V substrates. *Journal of crystal growth*, **165**, 203–209. 111

Ueta, A. & Hommel, D. (2002). New Concept for ZnTe-Based Homoepitaxial Light-Emitting Diodes Grown by Molecular Beam Epitaxy. *phys. stat. sol. (a)*, **192**, 177. 19, 45

Ulrich, S.M., Gies, C., Ates, S., Wiersig, J., Reitzenstein, S., Hofmann, C., Löffler, A., Forchel, A., Jahnke, F. & Michler, P. (2007). Photon Statistics of Semiconductor Microcavity Lasers. *Phys. Rev. Lett.*, **98**, 043906. 12

Unitt, D., Bennett, A., Atkinson, P., Ritchie, D. & Shields, A. (2005). Polarization control of quantum dot single-photon sources via a dipole-dependent Purcell effect. *Physical Review B*, **72**, 033318. 83

Valente, D., Suffczyński, J., Jakubczyk, T., Dousse, A., Lemaître, A., Sagnes, I., Lanco, L., Voisin, P., Auffeves, A. & Senellart, P. (2014).

Frequency cavity pulling induced by a single semiconductor quantum dot. *Physical Review B*, **89**, 041302. 98, 121

Voss, L.F., Reinhardt, C.E., Graff, R.T., Conway, A.M., Shao, Q., Nikolic, R.J., Dar, M.A. & Cheung, C.L. (2013). Analysis of strain in dielectric coated three dimensional Si micropillar arrays. *Journal of Vacuum Science and Technology B*, **31**, –. 95

Vučković, J., Pelton, M., Scherer, A. & Yamamoto, Y. (2002). Optimization of three-dimensional micropost microcavities for cavity quantum electrodynamics. *Physical Review A*, **66**, 023808. 15

Wang, S., Ding, D., Liu, X., Zhang, X.B., Smith, D., Furdyna, J. & Zhang, Y.H. (2009). MBE growth of II–VI materials on GaSb substrates for photovoltaic applications. *Journal of Crystal Growth*, **311**, 2116 – 2119. 106

Weisbuch, C., Nishioka, M., Ishikawa, A. & Arakawa, Y. (1992). Observation of the coupled exciton-photon mode splitting in a semiconductor quantum microcavity. *Phys. Rev. Lett.*, **69**, 3314–3317. 10

Winger, M., Volz, T., Tarel, G., Portolan, S., Badolato, A., Hennessy, K.J., Hu, E.L., Beveratos, A., Finley, J., Savona, V. *et al.* (2009). Explanation of photon correlations in the far-off-resonance optical emission from a quantum-dot–cavity system. *Physical review letters*, **103**, 207403. 85

Wojnar, P., Suffczyński, J., Kowalik, K., Golnik, A., Aleszkiewicz, M., Karczewski, G. & Kossut, J. (2008). Size-dependent magneto-optical effects in CdMnTe diluted magnetic quantum dots. *Nanotechnology*, **19**, 235403. 43

Wojnar, P., Bougerol, C., Bellet-Amalric, E., Besombes, L., Mariette, H. & Boukari, H. (2011). Towards vertical coupling of CdTe/ZnTe quantum dots formed by a high temperature tellurium induced process. *Journal of Crystal Growth*, **335**, 28 – 30. 17

Yablonovitch, E. (1987). Inhibited spontaneous emission in solid-state physics and electronics. *Physical review letters*, **58**, 2059. 2

Yeh, P. (1988). Optical waves in layered media. **95**. 115

Zverev, M., Sorokin, S., Sedova, I., Peregoudov, D., Ivanov, S. & Kopev, P. (2002). ZnSe-Based Room Temperature Low-Threshold Electron-Beam Pumped Semiconductor Laser. *physica status solidi (b)*, **229**, 1025–1028. 22